

رسالة الماجستير

MYOCARDIAL SEGMENTATION OF CARDIAC MRI IMAGES

A Thesis Presented to the Faculty
of
Nile University

In Partial Fulfillment
of the Requirements for the Degree
of Master of Science

By
Mustafa A. AlAttar
July 2010

CERTIFICATION OF APPROVAL

MYOCARDIAL SEGMENTATION OF CARDIAC MRI IMAGES

By
Mustafa A. AlAttar

Dr. Nael F. Osman (Chair)
Associate Professor in Radiology Department

Date

Dr. Ahmed S. Fahmy
Assistant Professor in Biomedical Eng. Department

Date

Dr. Ayman M. Khalifa
Assistant Professor in Biomedical Eng. Department

Date

© 2010

Mustafa A. AlAttar
ALL RIGHTS RESERVED

Dedicated To My Parents

ACKNOWLEDGEMENTS

First and foremost I am indebted to my research advisors, Dr. Nael F. Osman and Dr. Ahmed S. Fahmy, for their friendship, guidance, patience and understanding during my graduate life. I wouldn't have been standing here if it wasn't for their constant support.

I am definitely fortunate to have attended the Nile University and to have worked with these two doctors. I would also like to thank Dr. Ayman M. Khalifa for his time and energy in reviewing my dissertation and serving on my graduate board. My gratitude goes out to the entire faculty, and the staff of the Electrical and Computer Engineering, and the Nile University community at large. I would like to acknowledge that this research was supported by ITIDA.

Many others have made contributions to the research presented in this dissertation. In particular, I thank my colleagues in the Medical Imaging and Image Processing Laboratory and in the Center for Informatics Science. My friends at Medical Imaging and Image Processing Laboratory have the greatest source of encouragement and support both in academic and life matters. Thank you Abdallah, Kilany, Osman, Mina, Abraam and Essam.

I would like also to thank my parents Mr. Ahmed Ibrahim Al Attar and my Mum, my sister Asmaa, and my brother Ibrahim for their support and for all that they have done for me.

I am also very thankful to Dr. Mohamed Elhelw, Dr. Mohamed Abo Elhoda and Dr. Marian Azer for their gracious discussions and support during my graduate and research life.

I have met some incredibly nice and intelligent people during my master's studies at NU, naming them all would be a whole project by itself. Nonetheless, I'd like to name a few people of them. Ahmed Salah El Din, Ahmed Aley and Mohamed El Mahdy thank you all for your support.

Coming to the end of my journey at Cairo University and Nile University, I am obliged to Dr. Ahmed S. Fahmy, whose mentorship and support has had great influence on my life both inside and outside of the university.

LIST OF FIGURES

- Figure 2.1 Heart Structure
- Figure 2.2 (a) Proton magnetic moment direction is indicated by arrow. (b) In a typical material, magnetic moments are oriented randomly. (c) If a magnetic field is applied, magnetic moments align themselves along the direction of the field. Note that some are parallel, while others are anti parallel.
- Figure 2.3 Motions of a spinning top. Rotation or spin of the top about its own axis is first-order motion. Precession of the top about the vertical axis (axis of gravity) is second-order motion. Image courtesy of Hendee [22]
- Figure 2.4 Behavior of magnetic moments of protons (each denoted by a vector in the cone) in a rotating reference frame (a) Before RF pulse. Net magnetization (M) is along the longitudinal axis. (b)-(d) 90° RF pulse is sent in the x-direction inducing a magnetic field, B_1 . Rotation of the net magnetization vector during lifetime of the pulse is illustrated. e) Relaxation after termination of the pulse. Net magnetization turns back to the longitudinal direction. Longitudinal and transversal components of M (M_z and M_y) are shown. By courtesy of Skoog et al. [23].
- Figure 2.5 Two curves representing the effect of the longitudinal relaxation time on two different tissues A and B.
- Figure 2.6 Two curves representing the effect of the Transversal relaxation time on two different tissues A and B.
- Figure 2.7 Longitudinal relaxation. Longitudinal magnetisation, M_z (bold vector) reaches previous strength in time determined by T_1 . By courtesy of Skoog et al. [23]
- Figure 2.8 Transversal relaxation, M_y (bold vector) dies out due to dephasing of magnetic moments in time determined by T_2 . By courtesy of Skoog et al. [23].
- Figure 2.9 Slice selective excitation consists of applying a magnetic field gradient during the RF pulse application.

- Figure 2.10 Example of k-space trajectory. For every phase encoding step a number of echo samples are acquired while the frequency gradient is applied.
- Figure 2.11 a raw k-space acquired image. (Lower) Fourier transformed image as seen in direct space. A short-axis view of the heart is shown.
- Figure 2.12 (a) Short-axis spin-echo image is shown, (b) Short-axis gradient-recalled-echo image (images reproduced from [20])
- Figure 2.13 Six short-axis slices of heart from apex to the base using bright blood technique (image reproduced from [24])
- Figure 3.1 (a) Short-axis cardiac MRI image. (b) A binary image resulted from the thresholding process using single threshold value assigned by the dash line from the histogram on (e). (c) A resulted image of the thresholding by two thresholds at two gray levels assigned in the histogram at (f). (d-f) Histograms of the same gray-level image (a).
- Figure 3.2 (a)-(f) stages of application of the region growing on a short-axis cardiac CINE MRI at different times.
- Figure 3.3 (a) A short-axis cardiac MRI image with clear in-homogeneities. (b) A binary image resulted from application of region growing at threshold = 0.11. (c) A binary image resulted from application of region growing at threshold = 0.23.
- Figure 3.4 (a) Histogram showing three apparent classes. (b) The resulted image from the multi-thresholding technique using the threshold values specified by the classification applied on a short-axis cardiac MRI image.
- Figure 3.5 (a) A short-axis SENC MRI image with signal to noise ratio (b) A binary image representing the classified classes: background and tissue as black and white.
- Figure 3.6 (a) A short-axis SENC MRI image with signal to noise ratio (b) A binary image representing the classified classes: background and tissue as black and white.
- Figure 3.7 (a) A short-axis CINE MRI image. (b) A resulted image after clustering into two three classes. Courtesy of [48].

- Figure 3.8 (a) A short-axis Black-Blood MRI image. (b) Initial active contour and the final converged result. Courtesy of [56].
- Figure 4.1 Short-axis image of the heart with a good quality (Left) another image with in-homogeneity artifacts (Right)
- Figure 4.2 Short axis image with epi, interior and endocontour are drawn (Left) 4-constraining overlapped masks with their seed points (Right)
- Figure 4.3 Short axis image with epi, interior and endocontour are drawn (Left) 4-constraining overlapped masks with their seed points (Right)
- Figure 4.4 (Right images) Short axis image with sectors in white (Left images) result of region growing for each sector on the right image.
- Figure 4.5 Example of the dilation (a) Original image (b) the result image.
- Figure 4.6 Example of the erosion (a) Original image (b) The result image
- Figure 4.7 Results of the opening (a) and closing (b) operations on the original image from figure (4.5) (a).
- Figure 4.8 (a) Original Image (b) Segmentation result with black holes and speckles (c) result of closing operation
- Figure 4.9 (a) A myocardium image shown in the polar representation showing different types of interfaces (b) Three regions are highlighted with the same color of their types in the next chart (c) Chart represents the three types of features.
- Figure 4.10 a short-axis CINE MRI image with the segmentation contours and the refined control points in the three colors
- Figure 4.11 an image introduces the effect of the low resolution on the segmentation process
- Figure 4.12 (Left) Flowchart of the whole proposed algorithm (Right) Detailed flowchart of the main algorithm block.
- Figure 4.13 the curve in yellow represents the original profile and the profile of the mean contour after smoothing is in green with the classification results using k-means. Each classified sector is limited between each two successive blue points. And the black point is the centroid of each sector.

- Figure 4.14 Flowchart of the whole proposed algorithm (Left) Detailed flowchart of the main algorithm block (Right)
- Figure 4.15 The average perpendicular distance between two contours
- Figure 4.16 The parameters used by the Dice metric
- Figure 5.1 the region from the background that was taken to calculate the standard deviation
- Figure 5.2 Simple block diagram illustrates the steps of our experiment beginning with the signal simulation finishing with the decision making.
- Figure 5.3 The Joint PDF of signal intensities S1 and S2 for: (a) the background and (b) tissue samples
- Figure 5.4 Block Diagram of the Bayesian classifier system using real images
- Figure 5.5 Simple block diagram illustrates what are the steps of the simulation of the Bayesian technique & the other two techniques.
- Figure 5.6 Simple block diagram illustrates what are the steps of the simulation of the Bayesian technique & the other two techniques.
- Figure 6.1 Short-axis image (Left) Result of applying the simple RG (Right)
- Figure 6.2 (a) Original image (b) Result of applying region growing with threshold = 27 (c) Another result using threshold = 52
- Figure 6.3 (a) Original image (b) Result of MSRG with threshold = 21, no. of sectors = 10 and Overlapping Ratio = 0.1 (c) result using threshold = 29
- Figure 6.4 Performance curves of the RG and MSRG
- Figure 6.5 Three surfaces are representing the ground truth, TP and FP from upper to lower.
- Figure 6.6 (a) Original CINE image (b) Resulted two contours are drawn in red and green representing the endocardium and epicardium (c) Refined and smoothed contours using ACM and CPR
- Figure 6.7 Segmentation results on 24 time frames are shown between the red and white contours which representing the endocardium and epi cardium.

- Figure 6.8 Segmentation results of low quality dataset with high in-homogeneity in these images.
- Figure 6.9 Segmentation results on 24 time frames are shown.
- Figure 6.9 Segmentation results on 16 time frames are shown.
- Figure 6.11 Final results of the whole algorithm are shown where the white and red contours are representing epicardium and endocardium contour.
- Figure 6.12 (a) short axis CINE MRI image with endocardium, mid-wall and epicardium contours drawn in red, blue and white respectively (b) graph showing the profile of the mid wall contour in blue, the smoothed version of the original profile in red and the black squares are the resulted limits of the clusters using k-means which will be transformed into the polar space to form the limiting sector.
- Figure 6.13 Final results of the Adaptive MSRG (Red Contours represents the endocardium and White Contours represents the epicardium).
- Figure 6.14 Final results of the Adaptive MSRG (Red Contours represents the endocardium and White Contours represents the epicardium).
- Figure 6.15 Final results of the Adaptive MSRG (Red Contours represents the endocardium and White Contours represents the epicardium).
- Figure 6.16 Some of the failed segmented frames.
- Figure 7.1 The Joint PDF of signal intensities S_1 and S_2 for: (a) the background and (b) tissue samples. (c) and (d) are the Joint PDF of signal intensities S_1 and S_2 after removing the samples that are identified as background using Bayes Classifier for background and tissue signals. (e) and (f) are like (c, d) but identified using Quadratic Classifier, (g) and (h) are like (c, d) but identified using Rectangular Classifier. Also (i) and (j) are like (c, d) and for Linear classifier. All signals are generated with $\sigma = 70$.
- Figure 7.2 The Sensitivity (Ability of detecting Background) signals using the four methods for generated signals with different σ .
- Figure 7.3 The Specificity (Ability of detecting Tissue) signals using the four methods for generated signals with different σ .

- Figure 7.4 Precision using the four methods for generated signals with different σ .
- Figure 7.5 Two combined Images that were chosen to apply the different techniques on them.
- Figure 7.6 (a) shows the result of applying Bayesian technique, (b) shows the result of applying l_1 technique (c) shows the result of applying l_2 technique (d) shows the result of applying l_∞ technique (e) shows the result of applying Global Threshold technique.
- Figure 7.7 The different ROIs, background region (Dotted) static tissue (Dashed), and myocardium region (Solid).
- Figure 7.8 Shows the number of pixels considered as noise in the background region.
- Figure 7.9 Shows the number of pixels considered as noise in the background region.
- Figure 7.10 Shows the number of pixels considered as noise in the background region.
- Figure 7.11 Shows the sensitivity behavior for each technique within the time frames.
- Figure 7.12 Shows the sensitivity behavior for each technique within the time frames.
- Figure 7.13 (a) Original Black Blood MRI Image. (b) Final Result after application of the further processing and enhancement methods.

LIST OF TABLES

- Table. 6.1 Sensitivity and precision of each method (simple region Growing, Multi-Seeded Region Growing and Adaptive Multi-Seeded Region Growing)
- Table 7.1 Relative Computation Time for each technique.
- Table 7.2 Relative Computation

TABLE OF CONTENT

ACKNOWLEDGEMENTS	v
LIST OF FIGURES.....	vii
LIST OF TABLES	xiii
ABSTRACT	xvii
INTRODUCTION.....	1
1.1. Motivation	1
1.2. Problem Statement.....	4
1.3. Thesis Objective	5
1.4. Thesis Overview	6
BACKGROUND.....	8
2.1. Physiology Review.....	8
2.1.1. Heart Anatomy	8
2.1.2. Physiological Measurements.....	10
2.2. MRI concepts and data material	11
2.2.1. History of MRI	11
2.2.3. Cardiac MRI.....	25
2.2.4. Cardiac MRI Imaging Methods:	27
RELATED WORK	32
3.1. Thresholding.....	32
3.2. Region Growing	34
3.3. Classifiers	36
3.4. Clustering	40
3.5. Graph-based segmentation	42
3.6. Active contour models ACMs	42
3.7. Active shape models ASMs.....	44

3.8.	Active appearance models AAMs	44
3.9.	Level-set segmentation	45
	CINE IMAGES SEGMENTATION METHODS	46
4.1.	Multi Seeded Region Growing with fixed Sectors sizes (Experiment 1)....	46
4.1.1.	Standard region growing algorithm (RG)	46
4.1.2.	Limitations of region growing.....	47
4.1.3.	Multi-Seeded Region Growing (MSRG)	48
4.1.4.	Morphological Operations.....	53
4.1.5.	Epicardial Control Points	58
4.1.6.	Refinement of the Contours using ACMs	60
4.1.7.	Proposed Algorithm	64
4.2.	Adaptive Multi Seeded Region Growing using K-Means (Experiment 2) ..	65
4.2.1.	Multi-Seeded Region Growing	65
4.2.2.	Seed Points and Constraining Areas Selection	65
4.2.3.	K-Means	65
4.2.4.	Proposed Algorithm	67
4.3.	Automatic Evaluation Methods	68
4.3.1.	Average perpendicular distance	68
4.3.2.	Dice metric	70
4.3.3.	Accuracy Measurements	71
4.3.4.	Visual (Manual) Evaluation Method.....	71
4.3.5.	Another Parameters that's taken into account.....	72
	BLACK BLOOD IMAGES CLASSIFICATION.....	73
5.1.	Modified STEAM for Black Blood Imaging.....	74
5.2.	Stochastic Model	75
5.3.	Classification Techniques.....	76
5.3.1.	Bayesian Classifier.....	76
5.3.2.	Linear Classifier L ₁ -Norm.....	77
5.3.3.	Quadratic Classifier L ₂ -Norm	79
5.3.4.	Rectangular Classifier L _{inf} -Norm	79
5.4.	Numerical Simulation	79

5.4.1. Case1: Background Signal	80
5.4.2. Case2: Tissue Signal	81
5.5. Real Images Test	82
5.6. Further Processing	84
5.7. Performance Evaluation Methods	87
CINE SEGMENTATION RESULTS & DISCUSSION	88
6.1. Multi Seeded Region Growing with fixed Sectors sizes (Experiment 1) Results	89
6.1.1. Simple Region Growing.....	89
6.1.2. Multi Seeded Region Growing constrained by Overlapped Sectors.....	90
6.1.3. Evaluation of the MSRG Coefficients	91
6.1.4. Resulted Contour Refinement using ACM and CPR.....	93
6.1.5. Final Results.....	94
6.2. Adaptive Multi Seeded Region Growing using K-Means (Experiment 2) Results	99
6.2.1. Selecting the sectors sizes and positions using k-means.....	99
6.2.2. Quantitative Analysis	100
6.2.3. Final Results:.....	101
BB CLASSIFICATION RESULTS & DISCUSSION	107
7.1. Simulated Data Results.....	107
7.2. Real Images Results	110
CONCLUSION	118
8.1. Future Work.....	120
REFERENCES.....	121

ABSTRACT

Imaging the heart using cine MRI and Black-blood MRI sequences is very important to evaluate the cardiac global and regional function. In the first type of imaging which is cine MRI, Manual segmentation of the contours in all images through different slices is a cumbersome task. Therefore, methods were proposed to automatically or semi-automatically analyze and segment the contours from short-axis images and derive useful clinical information from them is highly desirable. In this thesis, we have proposed two algorithms to segment LV and they are Multi-Seeded Region Growing MSRG and adaptive MSRG. Their performance has been evaluated also in this thesis. The second type of images which is BB images suffers from the low signal-to-noise ratio SNR in general. In this thesis, a probabilistic model of blood and tissue signals is developed and used to build a Bayesian decision function to identify and filter the noise from the background signal. Numerical simulation and real MRI images were used to test and validate the proposed method. Also, the proposed method is compared to other conventional techniques.

INTRODUCTION

1.1. Motivation

According to estimates from the American Heart Association [1], each year 17 million people die of cardiovascular disease (CVD) around the globe; this is over 29% of all deaths globally. 80% of chronic disease deaths occur in low and middle income countries and half are women. Cardiovascular disease alone will kill five times as many people as HIV/AIDS in these countries. At least 20 million people survive heart attacks and strokes every year; many require continuing costly clinical care.

Locally, around 8.08% of the population in Egypt has heart diseases. 4.85% of the population in Egypt also has coronary heart diseases. Patients with high blood pressure are forming 25% of the total population or about 20 million [1, 2].

CVD is the most costly disease, accounting for 11.6% of the total cost of illness in the world. Therefore any effort to improve screening, diagnosis and treatment of CVD is highly beneficial to society.

Generally, cardiac examination involves assessing a combination of the four following physiological measures: cardiac structure, function, perfusion and myocardial viability. Different imaging modalities, including Ultrasound (US), single-photon emission computer tomography (SPECT), computed tomography (CT), and magnetic resonance imaging (MRI) are used in performing cardiac examinations.

Among existing methods, cardiac MRI (CMR) has attracted significant interest in the

research community, as a single imaging technique capable of retrieving all cardiac measures [3, 4], appropriately given the name "one-stop shop". Despite MRI's effectiveness and wide acceptance in cardiovascular research, it is used infrequently in clinical applications due to some limitations.

The patient's ability to remain still plays a major role in quality of MR imaging, as patient movements and respiratory motion create artifacts in MR images, causing degradation of image quality. However, advancements in MRI hardware and acquisition systems have improved image quality by minimizing such effects.

Imaging the heart using CINE MRI and Black-blood MRI sequences "SENC as an example" are very important tools to evaluate the cardiac global and regional function. These include estimating the ejection fraction, left ventricle (LV) mass and volume, wall-thickness, wall-thickening and contractility inside the myocardium.

In the first type which is CINE MRI, the parameters are usually estimated from datasets that typically include 6-10 short-axis slices of the heart acquired over the entire cardiac cycle with frame rate equal to 20-35 image/cycle [5]. Including some long-axis scans, there are about 350 images to be processed per cardiac acquisition session.

Manual segmentation of the contours in all images through different slices is a cumbersome task. Therefore, methods were proposed to automatically or semi-automatically analyze and segment the contours from short-axis images and derive useful clinical information from them is highly desirable.

Analysis of the left ventricle (LV) in particular has attracted a lot of attention in the medical imaging community, as numerous CVD symptoms are manifested through variations in the left ventricle's volume, mass or motion pattern. Ejection fraction of the left ventricle is another important clinical measure, which is derived based on the LV volume at two critical cardiac phases. While segmentation of the left ventricle in each short-axis slice at any time instance provides volumetric data of the given phase, tracking or detection of the ventricle boundaries through the cardiac cycle represents the ventricle motion.

Segmentation and/or tracking of the LV have been an active research topic for the past decade. Numerous vision-based algorithms have been utilized to address this problem, the most prevalent of which include thresholding, region-based, contour-based, and shape-based methods. Recently different formulations of probabilistic models have also been deployed to solve this problem. Most of these algorithms require either manual initialization of the contours in the first image (of a stacked data set), or they rely on a prior model obtained from training sets.

And in the second one which is Black-blood MRI, we have two short axis image sequences and they are called low tune and high tune sequence with frame rate 10-14 image/cycle [6]. In this imaging technique the blood signal is nulled to increase the contrast-to-noise ratio (CNR) of myocardium-background, to avoid the flow artifacts because of the blood and compute the contractility in the required place not in the blood regions. Aletras et al [7] proposed an acquisition technique for acquiring cardiac images with black-blood contrast. Nevertheless, the technique could null the

blood signal only at one specific time instance during the cardiac cycle and thus cannot produce cine sequence. This limitation prohibits using the technique in the assessment of the heart motion. Another technique that can be used to produce cine sequence with black-blood contrast was proposed by Frahm et al and known as STEAM [8]; unfortunately, the use of STEAM was hindered by severe deformation-dependent artifact that has been reported by many researchers [8,9]—such as fading of the signal. To overcome these limitations, Fahmy et al proposed a modified STEAM-based technique that successfully 1) corrects the STEAM artifacts, and 2) produces cardiac cine sequences with black-blood contrast [10]. However, as good as modified STEAM is, it suffers from low CNR, and there is a great need to enhance this poor CNR by reducing the level of background noise signal.

1.2. Problem Statement

We have two main problems; the first one is that, an automatic technique is required to segment the myocardium (the left ventricle muscle) in the CINE short-axis images and this technique must be fast, simple and reliable.

The other problem here is that we are in need to find a technique which can classify the background blood and tissue from the low and high tune sequences to null the background blood pixels and reset their values into zero and consequently increase the CNR values.

1.3. Thesis Objective

Our first objective is to segment the LV tissue in short-axis cardiac MRI images with minimal user interaction and extract the inner and outer boundaries in a fast way with guaranteeing the reliability. The inner and outer walls of the left ventricle are called endocardium and epicardium respectively.

The motion of left ventricle will be traced using segmentation of each frame and the resulted two contours of the preceding frame to estimate the initial conditions of the new frame. We do not require manual segmentation except for the first frame and it is just estimate for the first frame inner and outer contours and it can be put roughly not exact estimate. We make use of the fact that image data are causal, and combine image measurements of each frame with boundary estimation of the previous frame to perform exact detection of the left ventricle boundary and make the movement of the segmented endocardium and epicardium more stable. The full algorithm is stated in a clear way in the methods chapter. The proposed algorithm and technique is fast and efficient that is comparable with other methods.

The second objective is to classify the black-blood MRI images into two main classes: the background blood and the foreground tissue using two features which are low tune images and high tune images.

Methods for classification exist, but they are not optimal for the case of modified STEAM suggested by Fahmy et al. In this thesis we propose a technique to segment

the background noise in the modified STEAM images to null it. And consequently increase the CNR ratio. Also we explore the use of other methods of classification and their results. Numerical simulation and quantitative studies were done to compare the performance of the used methods. Finally, validation on real MRI modified STEAM images was performed.

1.4. Thesis Overview

The thesis is structured as follows:

- Chapter 2 covers the basic information about the heart anatomy, physiology and important measurements. It includes also some basic concepts of MRI, its physics and different pulse sequences.
- Chapter 3 gives a literature review of reported segmentation techniques for the CINE MR images and the classification techniques in literature for the black blood images.
- Chapter 4 describes the methods and algorithms proposed to segment the myocardium in the CINE MR images automatically. It describes also the technique evaluation methodologies to judge the performance of the proposed techniques fairly.
- Chapter 5 describes the classification methods proposed to classify the black-blood MRI images.
- Chapter 6 covers the results of the segmentation techniques and discussion of these results.

- Chapter 7 describes the results of the classification techniques and the discussion of their results.
- Chapter 8 provides a summary, discussion and final conclusions and gives proposals for future work.

BACKGROUND

This chapter provides a basic overview of the background theory necessary for understanding the problem at hand, and the formulation of the proposed solution.

Section 2.1 gives a summarized description of heart physiology and different physiological measures derived from CMR image analysis. The basis of the MR imaging modality, and its usage in diagnosis of cardiovascular disease, are discussed in Section 2.2.

2.1. Physiology Review

2.1.1. Heart Anatomy

The cardiovascular system consists of the heart and two vascular systems the systemic and pulmonary circulations [11]. The human heart, shown in figure 2.1, is a muscular four chambered organ, responsible for pumping blood throughout the body using rhythmic actions, or what is commonly known as the heart beat. The top two chambers, or atria, work as a reservoir to collect the blood that is coming into the heart. The bottom two chambers, or ventricles, have strong muscles, enabling them to provide the pumping action required to push the blood out of the heart and through the vascular systems. The right side of the heart is part of the pulmonary circulation, which receives de-oxygenated blood from body organs and delivers it to the lungs. The left side, on the other hand, is an essential part of the systemic circulation and collects the oxygenated blood in the left atrium and pumps it to various body organs using the left ventricle. Since a larger force is required from the left side to participate

in systemic circulation, the left ventricle has a much thicker and more muscular wall. The myocardium, depicted in figure 2.1, is the muscular wall of the heart. The smooth outer surface of the myocardium is called the epicardium, while the inner lining is known as the endocardium. The apex and base of the heart, as one might expect are the bottom and the top of the heart as displayed in figure 2.1.

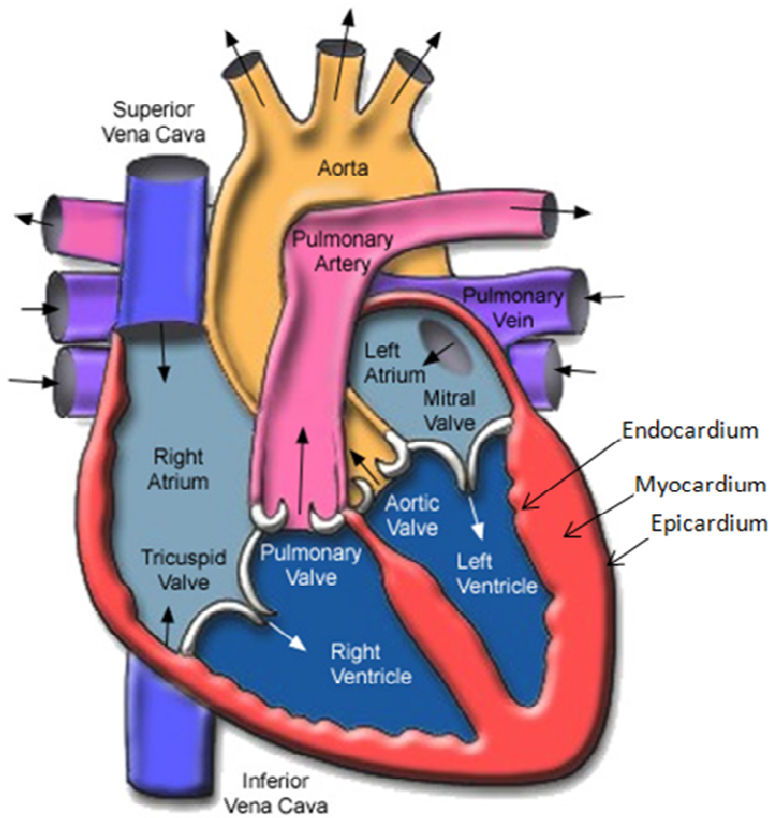


Figure 2.1 Heart Structure

Each cardiac cycle is divided into two main stages [12]:

Diastole: during the period of diastole (or relaxation), the atria contract in order to push the blood to ventricles, which are relaxed and filling with blood.

Systole: during this period the ventricles contract to pump the blood out of the heart to lungs and other body tissues, while the atria are relaxed and filling.

Considering the fact that normal heart rate of a healthy adult is around 72 bpm (beats per minute), each cardiac cycle takes approximately 0.8 seconds to complete.

2.1.2. Physiological Measurements

General health and proper function of the heart depends on numerous factors.

Evaluation of cardiac function is performed based on global and local physiological measurements.

Some of these measurements are listed below:

- End-Diastolic Volume (EDV): the volume of blood in a ventricle at the end of diastole, or filling stage.
- End-Systolic Volume (ESV): the volume of blood in a ventricle right after systole, or ejection period, which is a measurement of adequacy of cardiac ejection.
- Stroke Volume (SV): the volume of blood ejected from a ventricle at each heart beat, which is calculated based on EDV and ESV as follows:

$$SV = EDV - ESV$$

- Ejection Fraction (EF): defined as

$$E_f = \frac{SV}{EDV} = \frac{EDV - ESV}{EDV}$$

is the fraction of the end-diastolic volume (EDV) that is ejected with each heart beat.

Ejection fraction (EF) is normally computed for the left ventricle unless otherwise stated. In addition to the above-mentioned measures, myocardial wall motion and thickness are also derivable from cardiac imaging. These physiological values assist in diagnosis of various heart conditions such as ischemia, or acquired heart disease [13].

2.2. MRI concepts and data material

Many imaging modalities are used in the screening and diagnosis of cardiovascular disease. Some of the more established techniques, reviewed in [14], include: Ultrasound (US), single-photon emission computer tomography (SPECT), computed tomography (CT), and magnetic resonance imaging (MRI). Among these methods MRI deserves special attention as the ideal "one-stop shop", which can potentially address most cardiac examination needs [14, 15]. It provides detailed images of the human body and has shown extreme flexibility with respect to different body parts, diseases, orientation, motion and so forth. Apart from these advantages, it is completely harmless for the patient unlike many existing methods. For the last few years, it has become increasingly widespread and in 2003 approximately 22.000 MRI scanners were used in 60 million examinations around the world [16]. The basic theory behind MRI and its applications in cardiac imaging are presented in the following sections.

2.2.1. History of MRI

Magnetic resonance imaging is a relatively new technology. The first MR image was published in 1973[17, 18] and the first cross-sectional image of a living mouse was published in January 1974.[19] The first studies performed on humans were published in 1977. [20, 21] By comparison, the first human X-ray image was taken in 1895.

Magnetic resonance imaging was developed from knowledge gained in the study of nuclear magnetic resonance. In its early years the technique was referred to as nuclear magnetic resonance imaging (NMRI).

NMR was first discovered in 1946 by Bloch and Purcell. Between years 1950 and 1970 magnetic resonance was used in physical and chemical molecular analysis.

However, because the word nuclear was associated in the public mind with ionizing radiation exposure it is generally now referred to simply as MRI. Scientists still use the term NMRI when discussing non-medical devices operating on the same principles. The term magnetic resonance tomography (MRT) is also sometimes used.

Back projection reconstruction methods were used for NMR imaging. In 1975 Ernst introduced magnetic resonance imaging with phase and frequency encoding and Fourier transform, which is the technique currently used today. With continuous developments in hardware equipment and information technology, fast dynamic MR acquisition has been enabled which gave new diagnostic and interventional aspects to MRI. The 2003 medicine Nobel Prize attributed to Sir Peter Mansfield and Peter Lauterbur shows the importance of MRI contribution to medicine.

2.2.2. Basic concepts of MRI

The MRI technique is based on placing the patient inside a strong magnetic field (most current scanners operate at 1 - 3 Tesla). Atoms with odd number of protons or neutrons, for example hydrogen, sodium and phosphorus, possess a spin angular momentum. Due to its high abundance, the hydrogen atom (proton) is the most widely used in MRI applications. When the protons are placed in a strong external magnetic field as in the MR scanner, they act like compass needles due to their spin properties. This means that some of them align themselves with the magnetic field, the lower energy level, and some of them align opposite to the magnetic field, the higher energy level. In figure (2.2) the different states of protons if put under a strong magnetic field and without magnetic are shown.

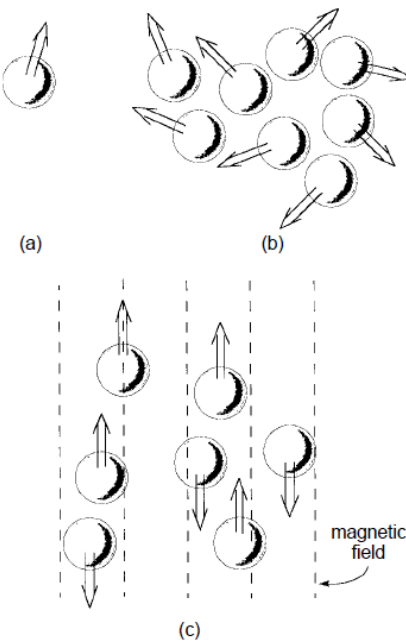


Figure 2.2 (a) Proton magnetic moment direction is indicated by arrow. (b) In a typical material, magnetic moments are oriented randomly. (c) If a magnetic field is

applied, magnetic moments align themselves along the direction of the field. Note that some are parallel, while others are anti parallel.

Two spins in opposite direction cancel each other out but the remaining spins at the lower energy level produce magnetic field along the direction of the external field called longitudinal magnetization. The protons way to spin around the longitudinal axis is called *precession* as shown in figure (2.3).

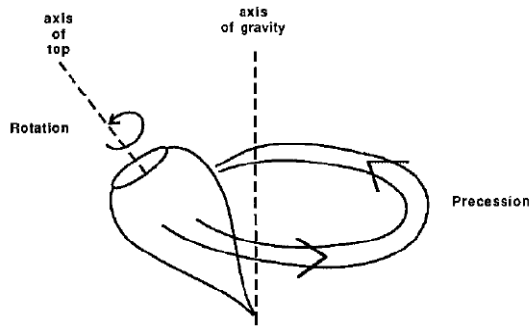


Figure 2.3 Motions of a spinning top. Rotation or spin of the top about its own axis is first-order motion. Precession of the top about the vertical axis (axis of gravity) is second-order motion. Image courtesy of Hendee [22]

Further, they have a precession frequency ω_0 , which can be calculated by the Larmor equation given in this equation

$$\omega_0 = \gamma B_0$$

Here B_0 is the strength of the external magnetic field and γ is the gyro magnetic ratio of the element being observed (here hydrogen). The longitudinal magnetization does not provide the signal needed to give information about a certain body part. By sending a *radio frequency (RF) pulse* through a coil of wire into the system, a second

magnetic field is induced. This is referred to as *resonance* and allows some of the protons to move from a lower to a higher energy level, resulting in decrease in the longitudinal magnetization. Other protons precess away from the longitudinal alignment into the transverse (x,y) plane, resulting in *transversal magnetization*, B_1 . This causes the net magnetization, M to turn by an angle α . After the RF pulse terminates, the protons relax, diphase in the transversal plane and reach equilibrium again. Figure (2.4) illustrates this in a rotating reference frame often useful when visualizing the magnetization.

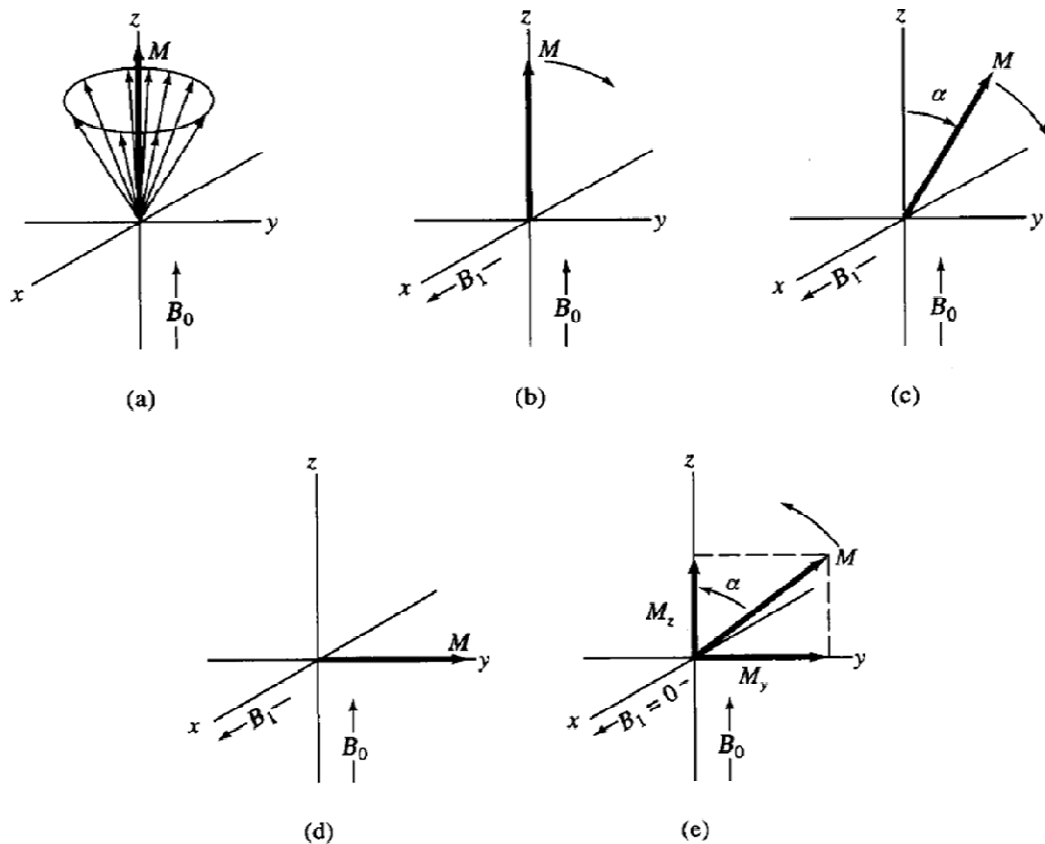


Figure 2.4 Behavior of magnetic moments of protons (each denoted by a vector in the cone) in a rotating reference frame (a) Before RF pulse. Net magnetization (M) is

along the longitudinal axis. (b)-(d) 90° RF pulse is sent in the x -direction inducing a magnetic field, B_1 . Rotation of the net magnetization vector during lifetime of the pulse is illustrated. e) Relaxation after termination of the pulse. Net magnetization turns back to the longitudinal direction. Longitudinal and transversal components of M (M_z and M_y) are shown. By courtesy of Skoog et al. [23]

The rate of relaxation is assessed by two constants:

1. T_1 : *Longitudinal relaxation time*, determines the time it takes to attain the previous longitudinal magnetization and describes how M_z returns to its equilibrium value. The equation governing this behavior as a function of the time t after its displacement is,

$$M_z = M_0 (1 - e^{-t/T_1})$$

In figure (2.5) you can see the effect of *Longitudinal relaxation time* on the magnetization of two different tissues or materials.

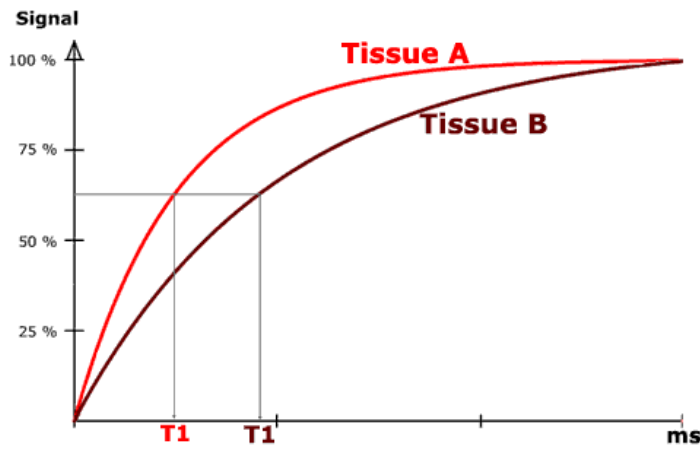


Figure 2.5 Two curves representing the effect of the longitudinal relaxation time on two different tissues A and B.

2. *T₂*: *Transversal relaxation time*, determines the time it takes the transversal magnetization to die out and describes the return to equilibrium of the transverse magnetization, M_{XY} and the equation governing this behavior as a function of the time t after its displacement is,

$$M_{XY} = M_{XY_0} e^{-t/T_2}$$

In figure (2.6) you can also figure out the effect of *Longitudinal relaxation time* on the magnetization of two different tissues or materials.

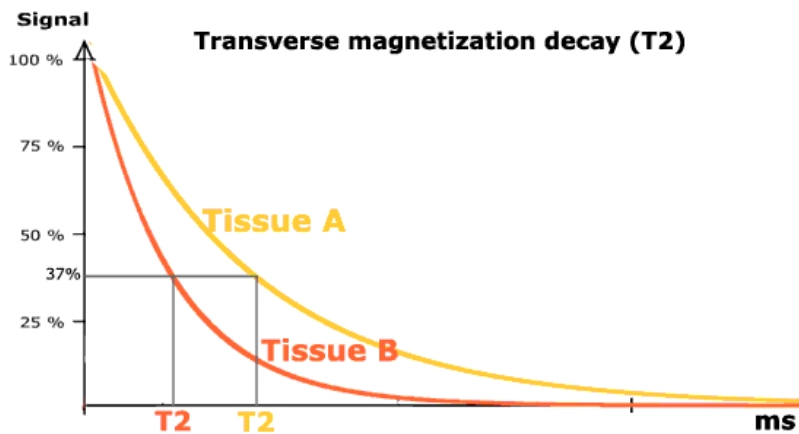


Figure 2.6 Two curves representing the effect of the Transversal relaxation time on two different tissues A and B.

T_2 is always less than or equal to T_1 . The net magnetization in the XY plane goes to zero and then the longitudinal magnetization grows in until we have M_0 along Z. Figures (2.7) and (2.8) illustrate the longitudinal and transversal relaxation respectively. Immediately after turning the RF pulse off, the protons emit a radio signal, the MR signal, of the same frequency as was sent into the system. Gradually the signal dies out as the system reaches equilibrium.

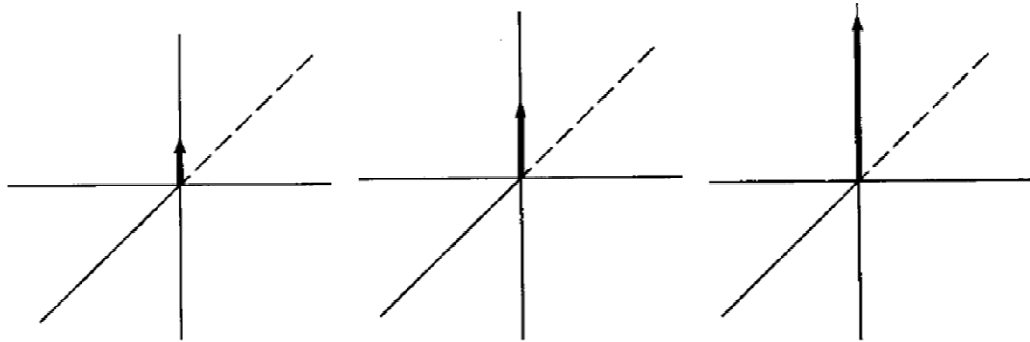


Figure 2.7 Longitudinal relaxation. Longitudinal magnetisation, M_z (bold vector) reaches previous strength in time determined by T_1 . By courtesy of Skoog et al. [23]

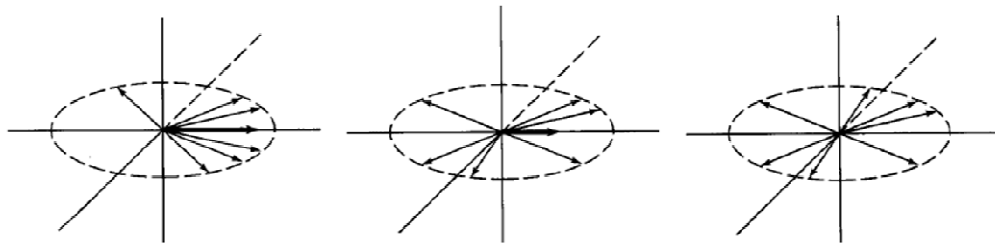


Figure 2.8 Transversal relaxation, M_y (bold vector) dies out due to dephasing of magnetic moments in time determined by T_2 . By courtesy of Skoog et al. [23].

Since the precession frequency of the protons is affected by the magnetic field strength by Equation 2.1, spatial variation of precession frequencies can be created by *gradient* fields which produce different strengths across the magnet and therefore different signals. Since the short duration of the radio signals, a sequence of RF pulses must be generated to obtain the sufficient information to generate an image from the observed signals.

The received MR signals depend on several factors. A few of them are listed below.

- Proton density and frequency
- T1 and T2 relaxation times
- Metabolic properties
- Motion
- Flow and viscosity
- Contrast agents

In order to generate an image with good contrasts, the above mentioned factors are utilized by designing the pulse sequence so as to weight those factors differently. For example, water has shorter relaxation times than fat. This can be utilized by sending two radio pulses with appropriate time gap which optimizes the relaxation difference between the tissues and thereby the image contrast. The resulting image is referred to as a T1-weighted or T2-weighted image depending on which of the relaxation differences, longitudinal or transversal, are being optimized. Paramagnetic contrast agents, for example Gadolinium (Gd-DTPA) shorten the relaxation times for the tissue it is exposed to, which has given the appropriate pulse sequence can generate good contrasts in the image.

Commonly used pulse sequences are for example Saturation recovery sequence, which only uses 90° pulses ($\alpha = 90^\circ$), inversion recovery sequence, which uses 180° pulse followed by a 90° pulse to generate T1-weighted images and a spin echo sequence, which uses a 90° pulse followed by 180° pulses.

Attempts have been made to make the imaging faster, for example FLASH (Fast low angle shot), which decreases the flip (pulse) angle below 90° to reduce the time between pulses.

Spatial localization Elements of imaged volume are called voxels. To localize a slice, slice selection is applied during the RF excitation pulse figure (2.9). This is realized using magnetic field gradients.

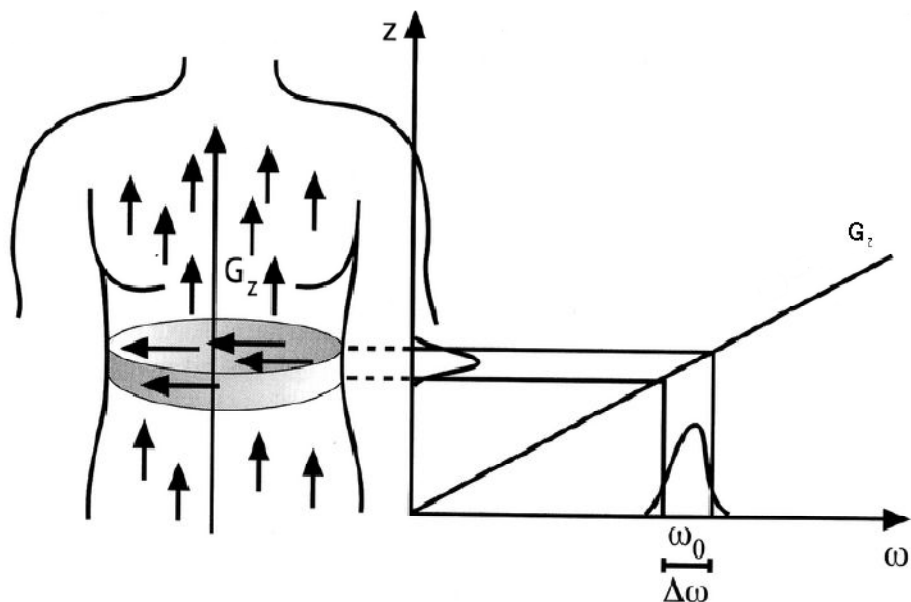


Figure 2.9 Slice selective excitation consists of applying a magnetic field gradient during the RF pulse application.

For a slice perpendicular to the z direction (conventionally parallel to B_0), a magnetic gradient along the z direction, G_z will be applied. Consequently the resonance frequency of the protons depends on z:

$$\omega(z) = \gamma(B_0 + zG_z)$$

Thus the position of the slice will depend on the frequency, and the slice thickness on the transmitter RF bandwidth.

$$\Delta\omega = \gamma G_z \Delta z$$

Once a slice has been selected, the voxel within this slice must be spatially encoded. A phase gradient G_y of duration T , dephases spins in the “phase direction” conventionally noted y , by a phase

$$\varphi = \gamma(B_0 + yG_y)T$$

Similarly, voxel localization in the read or x direction is obtained with a frequency or readout gradient G_x . Based on the Bloch equation solution, the signal from a volume element dV can be expressed as:

$$ds(G, t) = \alpha \rho(r) dV e^{-t/T_2} e^{-i(\omega_0 + \gamma \cdot G \cdot r)t}$$

where $\rho(r)$ is the spin density in the voxel. Assuming $t \ll T_2$, the total signal from the excited slice is:

$$S(t) = \iiint \rho(r) e^{-i(\gamma \cdot G \cdot r)t} dr$$

By introducing the notion of k-space, with the spatial frequency vector:

$$k = \gamma G t,$$

the expression of MR signal in k-space is:

$$S(k) = \iiint \rho(r) e^{-i.k.r.t} dr$$

and the spatial distribution of spin density is obtained by Fourier transform:

$$\rho(r) = \iiint S(k) e^{i.k.r} dk.$$

K-space acquisition MR signal is measured in the k-space. K-space is filled by digitizing MR signal at different times. Each line in k-space corresponds to echo data for a single phase encoding step, and each column in a line corresponds to MR signal amplitudes at various times during the echo. By convention lines near the center of k-space correspond to low-order phase encoding steps, and extremity k-space lines correspond to high order phase encodings. After k-space filling is completed, the real space image is obtained by a 2-dimensional Fourier transform (2DFT) of the k-space grid. It is important to emphasize that individual cells in k-space do not correspond one-to-one with individual pixels in the MR image. Every pixel in the image contains information from all the k-space cells. The center of the k-space corresponds to low spatial frequencies, and is responsible for the gross object shape and contrast in the reconstructed image. The periphery of the k-space corresponds to high spatial frequencies, and is responsible for edge sharpness and detail in the reconstructed image in figure (2.10). In 3D imaging, z direction encoding analog to x and y

encoding is used instead of slice selection, and 3D Fourier transform is used to reconstruct images.

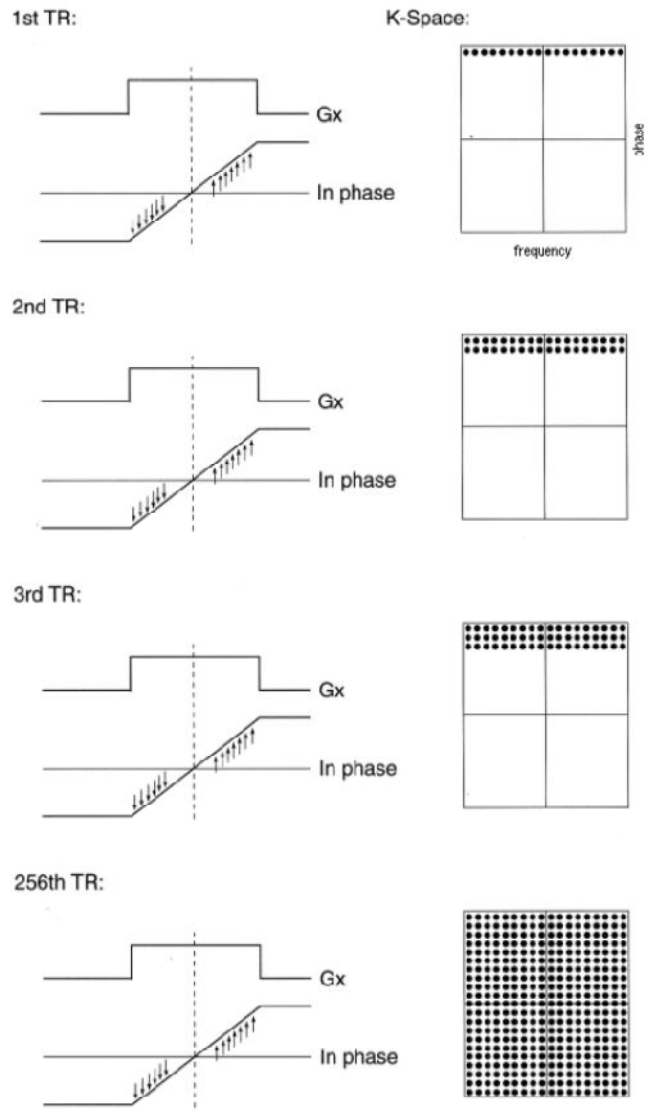
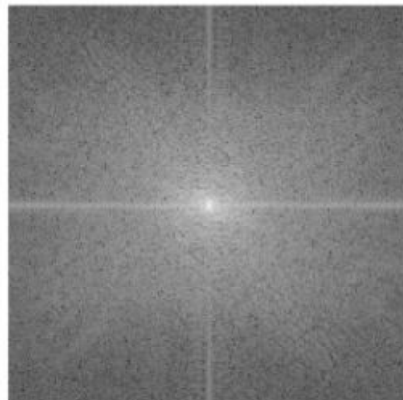


Figure 2.10 Example of k-space trajectory. For every phase encoding step a number of echo samples are acquired while the frequency gradient is applied.



↓ FT

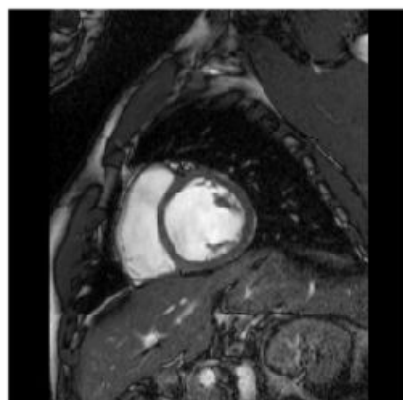
A diagram showing a downward-pointing arrow followed by the text "FT", indicating the Fourier Transform process.

Figure 2.11 a raw k-space acquired image. (Lower) Fourier transformed image as seen in direct space. A short-axis view of the heart is shown.

2.2.3. Cardiac MRI

Cardiovascular magnetic resonance imaging (CMR), sometimes known as cardiac MRI is a medical imaging technology for the non-invasive assessment of the function and structure of the cardiovascular system. It is derived from and based on the same basic principles as Magnetic Resonance Imaging MRI stated in the last sections but

with optimization for use in the cardiovascular system. These optimizations are principally in the use of ECG gating and rapid imaging techniques or sequences. By combining a variety of such techniques into protocols, key functional and morphological features of the cardiovascular system can be assessed.

Initial attempts to image the heart were confounded by respiratory and cardiac motion, solved by using cardiac ECG gating, faster scan techniques and breath hold imaging. Increasingly sophisticated techniques were developed including cine imaging and techniques to characterize heart muscle as normal or abnormal (fat infiltration, oedematous, iron loaded, acutely infarcted or fibrosed).

Cardiac MRI imaging is performed to help:

1. Evaluate the structures and function of the heart, valves, major vessels, and surrounding structures (such as the pericardium).
2. Diagnose and manage a variety of cardiovascular problems.
3. Detect and evaluate the effects of coronary artery disease.
4. Plan a patient's treatment for cardiovascular problems and monitor patient's progress.
5. Assess a patient's recovery following treatment.
6. Cardiac MRI is used to avoid the need for invasive procedures or tests that use radiation (such as x-rays) or dyes containing iodine (these dyes may be harmful to people who have kidney problems).

2.2.4. Cardiac MRI Imaging Methods:

CMR uses several different techniques within a single scan the combination of these results in a comprehensive assessment of the heart and cardiovascular system. Examples are below:

- Heart function using cine imaging (CINE)

Images of the heart may be acquired in real-time with CMR, but the image quality is limited. Instead most sequences use ECG gating to acquire images at each stage of the cardiac cycle over several heart beats. This technique forms the basis of functional assessment by CMR. Blood typically appears bright in these sequences due to the contrast properties of blood and its rapid flow. The technique can discriminate very well between blood and myocardium. The current technique typically used for this is called balanced steady state free precession (SSFP) [24].

- Heart regional function using Strain Encoded MRI (SENC)

Strain-encoded (SENC) imaging [26] is a technique that can directly image and quantify regional myocardial function. Strain encoding is the third type of encoding that can be done with MRI. In this case, the strain can be immediately encoded into the acquired images without measuring the displacement or velocity first. The technique does not measure the strain in arbitrary direction, but in a specific direction relative to the imaging plane. Similar to the previous two encoding, we can encode the regional strain in an image so that regional function can be assessed. There is one

technique that can be used to do the strain encoding, which is called SENC. The encoding with SENC differs from the previous displacement and velocity encodings in that strain is not encoded in the complex phase of an image.

- Visualizing heart muscle scar or fat without using a contrast agent

Typically a sequence called spin-echo is used. This causes the blood to appear black. These are high resolution still image which in certain circumstances identify abnormal myocardium through differences in intrinsic contrast.

- Infarct imaging using contrast

Scar is best seen after giving a contrast agent, typically one containing gadolinium bound to DTPA. With a special sequence, Inversion Recovery (IR) normal heart muscle appears dark, whilst areas of infarction appear bright white.

- Perfusion

In angina, the heart muscle is starved of oxygen by a coronary artery narrowing, especially during stress. This appears as a transient perfusion defect when a dose of contrast is given into a vein. Knowing whether a perfusion defect is present and where it is helps guide intervention and treatment for coronary artery stenosis.

The focus of our work is on the first two measures, cardiac morphology and function. Depending on the specific application, different MRI acquisition methods are utilized.

The two basic techniques in CMR, which are used in accurate depiction of morphology, are "black-blood" and "bright-blood" methods. Spin-echo (SE) was the first method generating black-blood sequences which make the blood appear darker than the myocardium and surrounding fatty tissues and the STEAM imaging also generates the same images with the same properties. SE has proven to be useful in visualizing morphology in congenital heart disease and pericardial abnormalities [14]. On the other hand, blood generates bright signal intensity, appearing lighter than myocardium, in bright-blood imaging [24]. The dominant sequences of this method include balanced steady state free precession (SSFP), gradient recalled echo (GRE) and fast GRE (fGRE). These methods yield both morphological and functional data as well as myocardial perfusion. A short-axis MRI scan using each of these methods is depicted in figure (2.12).

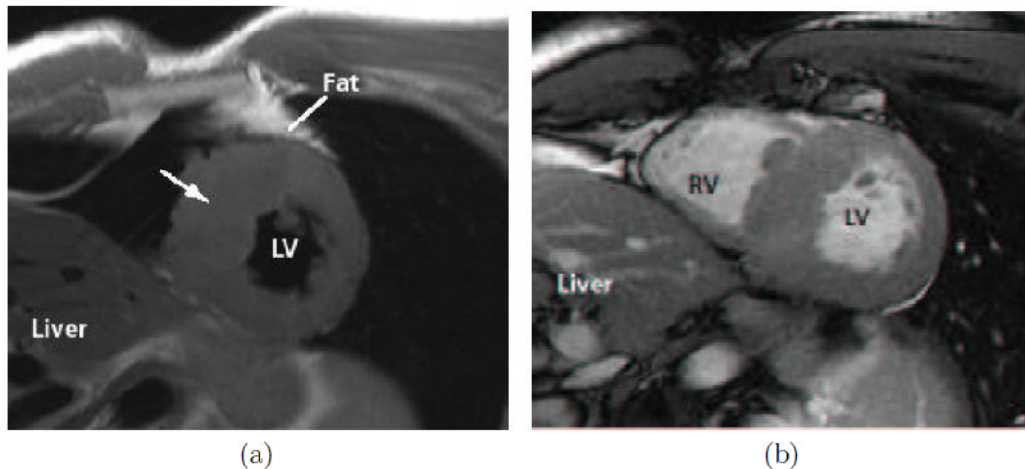


Figure 2.12 (a) Short-axis spin-echo image is shown, (b) Short-axis gradient-recalled-echo image (images reproduced from [20])

Evaluation of cardiac function is performed in a global scale through analysis of EF and in regional scale by measuring contractile malfunction. The latter is derived based on analysis of wall thickening in tagged MRI images, while the former is calculated based on cine MRI techniques. Cine MRI generates images of a single or multiple slices every 30-50 ms during cardiac cycle, providing temporal as well as spatial information. Since blood flow and respiratory motion create artifacts and noise in the resulting images, the imaging time of each scan should be minimized to avoid motion blurring. These artifacts pose some challenges in the analysis of cardiac images using traditional computer vision algorithms. Additionally, during each MRI acquisition, typically six to eight cross sectional slices are acquired from the apex to the base, all with around 20 time phases over the entire cardiac cycle (one scan every 50ms) resulting in approximately 160 short-axis 2D scans of the heart [25].

Figure (2.13) depicts six slices from the apex to the base. As one can imagine, manual analysis of this 3D+T, or better said 4D dataset, is prohibitive and exhaustive, not to mention error-prone and subjective. This expensive and lengthy process certainly poses problems for widespread use of CMR, despite its great capabilities and potential. The need for semi- or fully-automatic methods to extract useful clinical measurements from this data has led to an extensive amount of research in the field of cardiac imaging. Segmentation of the left ventricle can be thought of as the first step in the derivation of ventricular volume or EF. The next section presents a summary of some computer vision methods and how they have been adapted to address this particular problem.

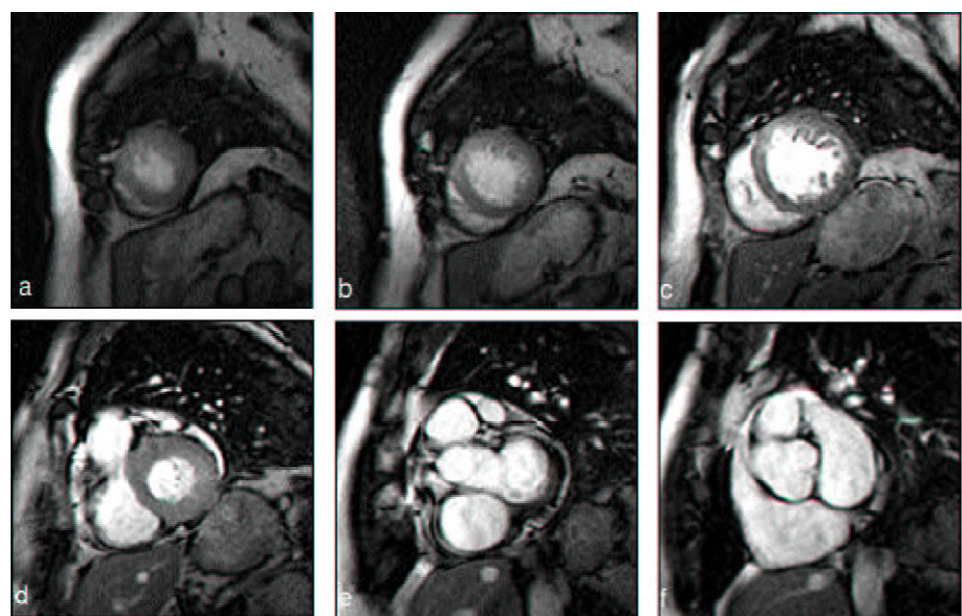


Figure 2.13 Six short-axis slices of heart from apex to the base using bright blood technique (image reproduced from [24])

RELATED WORK

Many cardiac LV segmentation methods have been proposed by the others to calculate blood volume, myocardial volume, and ejection fraction using MRI. These methods can be categorized as follows: traditional segmentation, graph-based segmentation, active shape model (ASM), and level-set algorithms.

Traditional segmentation algorithms use thresholding, region-growing, edge-detection, classifiers and clustering [27]–[34]. Since these algorithms alone require significant user-interaction to segment LV, they have been combined with other segmentation techniques in hybrid schemes to minimize user-intervention. These algorithms work for mid-ventricular slices of LV, but have problems in basal and apical slices. Also, they are unable to segment the detailed structure of papillary and trabecular muscles PTMs.

In the next sections we will give a brief about these traditional techniques.

3.1. Thresholding

Thresholding approaches segment scalar images by creating a binary partitioning of the image intensities. Figure (3.1.d) shows the histogram of a scalar image which is shown in figure (3.1.a) that possesses three apparent classes, corresponding to the three modes.

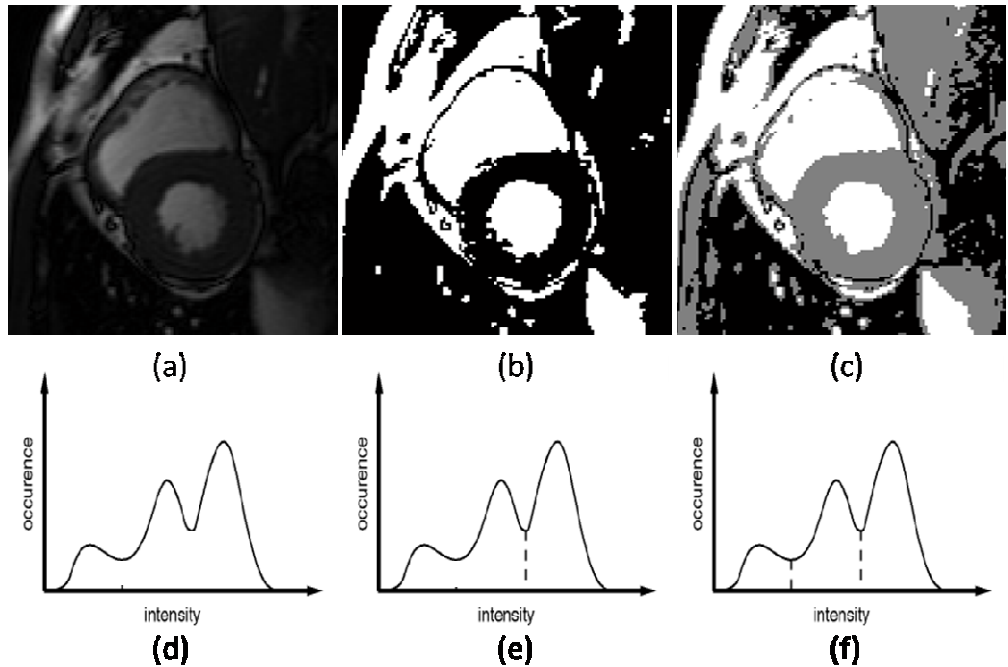


Figure 3.1 (a) Short-axis cardiac MRI image. (b) A binary image resulted from the thresholding process using single threshold value assigned by the dash line from the histogram on (e). (c) A resulted image of the thresholding by two thresholds at two gray levels assigned in the histogram at (f). (d-f) Histograms of the same gray-level image (a).

A thresholding procedure attempts to determine an intensity value, called the threshold, which separates the desired classes. The segmentation is then achieved by grouping all pixels with intensities greater than the threshold into one class and all other pixels into another class. Two potential thresholds are shown in Figure 1.f at the valleys of the histogram. Determination of more than one threshold value is a process called multi-thresholding [35].

Thresholding is a simple yet often effective means for obtaining a segmentation of images in which different structures have contrasting intensities or other quantifiable features. The partition is usually generated interactively, although automated methods do exist [35].

Thresholding is often performed interactively, based on the operator's visual assessment of the resulting segmentation. Thresholding is often used as an initial step in a sequence of image-processing operations [36, 37].

It has been applied in the myocardium segmentation in which a lot of classes of tissue are typically present. Its main limitations are that, in its simplest form, only two classes are generated, and it cannot be applied to multichannel images. In addition, thresholding typically does not take into account the spatial characteristics of an image. This causes it to be sensitive to noise and intensity in-homogeneities, which can occur in MR images.

Both of these artifacts essentially corrupt the histogram of the image, making separation more difficult. For these reasons, variations on classical thresholding have been proposed for medical-image segmentation that incorporate information based on local intensities [38] and connectivity [39]. A survey on thresholding techniques is provided elsewhere [35].

3.2. Region Growing

Region growing is a technique for extracting an image region that is connected based on some predefined criteria. These criteria can be based on intensity information and/or edges in the image [40]. In its simplest form, region growing requires a seed

point that is manually selected by an operator and extracts all pixels connected to the initial seed based on some predefined criteria. For example, one possible criterion might be to grow the region until an edge in the image is met. Another possible criterion might be to grow until the difference between the candidate pixels and the mean intensity of the current region is less than a threshold assigned manually or using the image statistical estimation.

Figure (3.2) shows the different stages of the simple region growing when applied on a short-axis CINE MRI image.

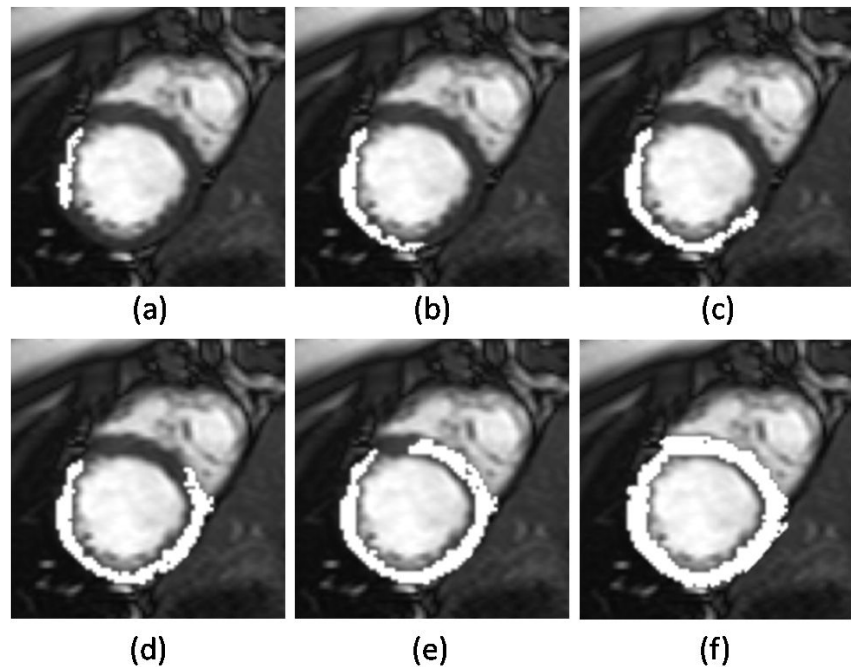


Figure 3.2 (a)-(f) stages of application of the region growing on a short-axis cardiac CINE MRI at different times.

It can be shown in figure (3) the effect of usage region growing on the short-axis MRI images with different threshold values.

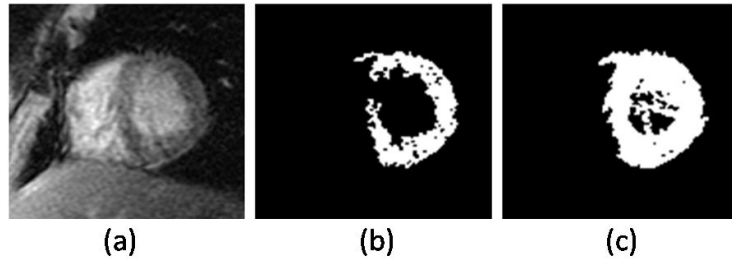


Figure 3.3 (a) A short-axis cardiac MRI image with clear in-homogeneities. (b) A binary image resulted from application of region growing at threshold = 0.11. (c) A binary image resulted from application of region growing at threshold = 0.23.

Like thresholding, region growing is seldom used alone but usually within a set of image-processing operations, particularly for the delineation of small, simple structures such as tumors and lesions [41, 42]. The primary disadvantage of region growing is that it requires manual interaction to obtain the seed point.

Thus, for each region that needs to be extracted, a seed must be planted. Split-and-merge is an algorithm related to region growing, but it does not require a seed point [43]. Region growing can also be sensitive to noise, causing extracted regions to have holes or even become disconnected and it does not preserve the spatial information so it can easily fail if there exists any in-homogeneity. Conversely, partial-volume effects can cause separate regions to become connected.

3.3. Classifiers

Classifier methods are pattern recognition techniques that seek to partition a feature space derived from the image by using data with known labels. A feature space is the range space of any function of the image, with the most common feature space being the image intensities themselves. A histogram, as shown in Figure (3.4.a), is an

example of a one-dimensional feature space. Figure (3.4.b) shows the result of the classification of an image according to the one dimensional feature space (histogram) in figure (3.4.a) and it seems like the thresholding using two thresholds because we has only one dimensional feature.

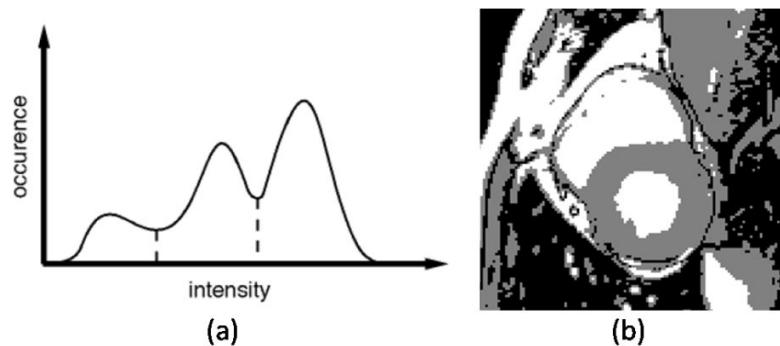


Figure 3.4 (a) Histogram showing three apparent classes. (b) The resulted image from the multi-thresholding technique using the threshold values specified by the classification applied on a short-axis cardiac MRI image.

Another example of the classification process is shown in figure (3.5.a). The image in figure (3.5.a) is a SENC MRI short-axis image and this image is a combination of two images which are low-tune and high-tune and these two images represents the two features which have been used for the classification process.

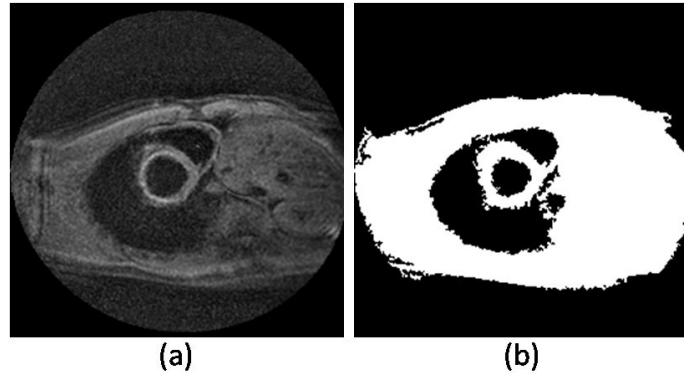


Figure 3.5 (a) A short-axis SENC MRI image with signal to noise ratio (b) A binary image representing the classified classes: background and tissue as black and white.

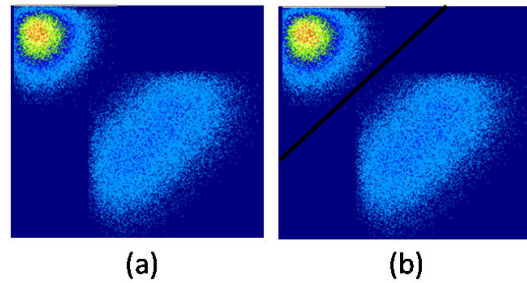


Figure 3.6 (a) A short-axis SENC MRI image with signal to noise ratio (b) A binary image representing the classified classes: background and tissue as black and white.

In figure (6) the two dimensional histogram of the simulation of the image in figure (3.5.a) can be shown. And the classification line can be shown in figure (3.6.b) which has been estimated using Bayesian classifier as an example.

Another feature space might have been generated from a dual-echo MR image, in which one axis represents the intensities of the proton density-weighted image and the other axis represents the intensities of the T2-weighted image. All pixels with their associated features on the left side of the partition would be grouped into one class.

Classifiers are known as supervised methods because they require training data that are manually segmented and then used as references for automatically segmenting new data. There are a number of ways in which training data can be applied in classifier methods. A simple classifier is the nearest-neighbor classifier, in which each pixel is classified in the same class as the training datum with the closest intensity. The k-nearest-neighbor classifier is a generalization of this approach, in which the pixel is classified into the same class as the majority of the k-closest training data. The k-nearest-neighbor classifier is considered a nonparametric classifier because it makes no underlying assumption about the statistical structure of the data.

A commonly used parametric classifier is the maximum-likelihood or Bayesian classifier. A result of applying of this method is shown before in figure (5-6). It assumes that the pixel intensities are independent samples from a mixture of probability distributions, usually Gaussian or have different probability distributions. This mixture, called a finite mixture model, is given by the probability density function,

$$f(y_j; \theta; \pi) = \sum_{k=1}^K \pi_k f_k(y_j; \theta_k),$$

where y_j is the intensity of pixel j ; f_k is a component probability density function parameterized by θ_k , and $\theta = [\theta_1, \dots, \theta_K]$. The variables π_k are mixing coefficients that weight the contribution of each density function and $\pi = [\pi_1, \dots, \pi_K]$.

Standard classifiers require that the structures to be segmented possess distinct quantifiable features. Because training data can be labeled, classifiers can transfer these labels to new data as long as the feature space sufficiently distinguishes each label as well. Being non iterative, classifiers are relatively computationally efficient, and, unlike thresholding methods, they can be applied to multichannel images. A disadvantage of classifiers is that they generally do not perform any spatial modeling. This weakness has been addressed in recent work extending classifier methods to segmenting images that are corrupted by intensity inhomogeneities [44] like what happens in cardiac MRI imaging. Another disadvantage is the requirement of manual interaction to obtain training data if we do not use a predefined model. Training sets can be acquired for each image that requires segmenting, but this can be time consuming and laborious.

On the other hand, use of the same training set for a large number of scans can lead to biased results that do not take into account anatomical and physiological variability between different subjects especially if we have healthy and unhealthy cases so the training datasets are huge and models cannot be evaluated easily.

3.4. Clustering

Clustering algorithms essentially perform the same function as classifier methods without the use of training data so that they are termed unsupervised methods. To compensate for the lack of training data, clustering methods iteratively alternate between segmenting the image and characterizing the properties of each class. In a sense, clustering methods train themselves, using the available data.

Three commonly used clustering algorithms are the K-means, the fuzzy c -means algorithm [45], and the expectation-maximization (EM) algorithm [46]. The K -means clustering algorithm clusters data by iteratively computing a mean intensity for each class and segmenting the image by classifying each pixel in the class with the closest mean [47]. Figure (3.7.b) shows the result of applying the K -means algorithm to a slice of short-axis CINE MRI image in Figure (3.7.a).

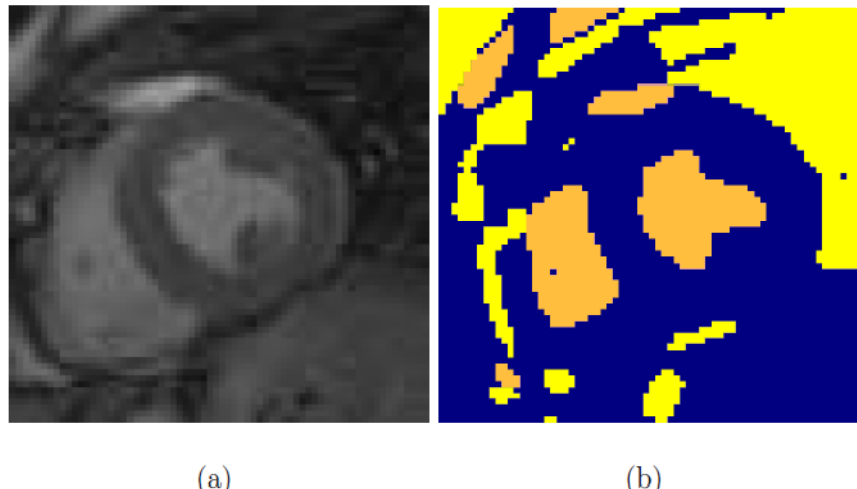


Figure 3.7 (a) A short-axis CINE MRI image. (b) A resulted image after clustering into two three classes. Courtesy of [48].

The number of classes was assumed to be three, representing (from dark gray to white in Figure (3.7.a) background, muscle, fat and blood. The fuzzy c -means algorithm generalizes the K -means algorithm, allowing for soft segmentations based on fuzzy set theory [49]. The EM algorithm applies the same clustering principles with the underlying assumption that the data follow a Gaussian mixture model. It iterates between computing the posterior probabilities and computing maximum likelihood estimates of the means, co-variances, and mixing coefficients of the mixture model.

Although clustering algorithms do not require training data, they do require an initial segmentation (or, equivalently, initial parameters). Like classifier methods, clustering algorithms do not directly incorporate spatial modeling and can therefore be sensitive to noise and intensity in-homogeneities. This lack of spatial modeling, however, can provide significant advantages for fast computation. Work on improving the robustness of clustering algorithms to intensity in-homogeneities in MR images has demonstrated excellent success.

3.5. Graph-based segmentation

Graph-based segmentation algorithms are based on selecting edges from a graph, where each pixel corresponds to a node in the graph, and certain neighboring pixels are connected by undirected edges. Weights on each edge measure the dissimilarity between pixels [50]–[52].

The graph (image) is then partitioned according to a criterion designed to model "good" clusters or finding a minimum cost path using graph-searching algorithms such as iterative programming. Each partition of the nodes (pixels) output from these algorithms are considered an object segment in the image. Some popular algorithms of this category are normalized cuts, random walker, minimum cut, isoperimetric partitioning and minimum spanning tree-based segmentation.

These methods are unable to accurately exclude complex cardiac structures such as PTMs from the segmentation of the left ventricle muscle, take long computation time and have difficulties in the basal and apical slices.

3.6. Active contour models ACMs

ACM is a framework for delineating an object outline from a possibly noisy 2D image. This framework attempts to minimize an energy associated to the current contour as a sum of an internal and external energy. The external energy is supposed to be minimal when the snake is at the object boundary position. The most straightforward approach consists in giving low values when the regularized gradient around the contour position reaches its peak value. The internal energy is supposed to be minimal when the snake has a shape which is supposed to be relevant considering the shape of the sought object. The most straightforward approach grants high energy to elongated contours (elastic force) and to bended/high curvature contours (rigid force), considering the shape should be as regular and smooth as possible [53]–[55].

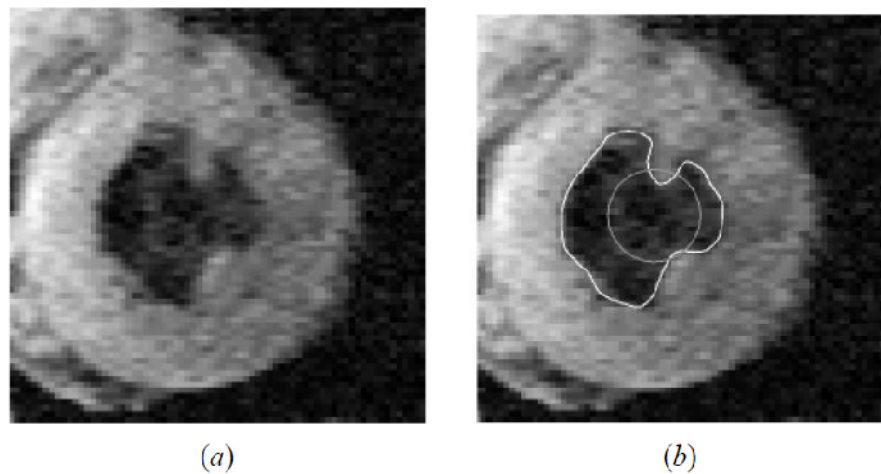


Figure 3.8 (a) A short-axis Black-Blood MRI image. (b) Initial active contour and the final converged result. Courtesy of [56].

The main advantages of active contour models ACMs are their ability to directly generate closed parametric curves or surfaces from images and their incorporation of

a smoothness constraint that provides robustness to noise and spurious edges. A disadvantage is that they require manual interaction to place an initial model and choose appropriate parameters. Reducing sensitivity to initialization has been a topic of research that has demonstrated excellent success. In addition, ACMs have difficulty with low contrast images. ACMs can also exhibit poor convergence to concave boundaries. This difficulty can be alleviated somewhat through the use of pressure forces and other modified external-force models. A general review on deformable models in medical image analysis can be found in reference [56].

3.7. Active shape models ASMs

ASMs, which are based on ACMs, segment objects using a shape model that is based on prior knowledge. The knowledge is represented by hand-annotated segmentation from a training dataset.

3.8. Active appearance models AAMs

AAMs are extensions of ASM that consider texture variation of objects with the shape of objects [57], [58]. Using a manual training dataset, the model is generated through principal component analysis, and the model is deformed according to the statistical variation of the dataset. ASM and AAM are limited in regard to the variation of the training dataset. Also, they impose high computational costs for iterative procedures. Moreover, ACM, ASM, and AAM have limitations in extracting the details of PTMs. And the disability of excluding them out of the left ventricle muscle.

3.9. Level-set segmentation

Level-set segmentation is a recent and well-established method to segment objects in noisy data [59]–[62]. However, it has difficulty in determining the stopping term, requires strong initialization of segmenting objects, and can get stuck in local minimum and high computational costs. Some algorithms use prior models to solve these problems, but the dependency on prior models results in loss of segmenting details and cardiac abnormalities.

In summary, much research has been performed in LV segmentation. Each algorithm has tradeoffs among time complexity, inter- or intra- operator variation, and accuracy in clinical practice. These algorithms have not excluded PTMs or segmented them in detail.

CINE IMAGES SEGMENTATION METHODS

4.1. Multi Seeded Region Growing with fixed Sectors sizes (Experiment 1)

The first experiment is the multi seeded region growing with fixed number and sizes of sectors and in this experiment, the number of sectors and the overlapping ratio will be evaluated by testing all the available datasets to give good results for all the images. And this work has been published in [63].

4.1.1. Standard region growing algorithm (RG)

Region growing is a simple region-based image segmentation method as stated in literature review chapter. It is also classified as a pixel-based image segmentation method since it involves the selection of initial seed points.

This approach to segmentation examines neighboring pixels of initial "seed points" and determines whether the pixel neighbors should be added to the region. The process is iterated on, in the same manner as general data clustering algorithms.

In standard region growing, an initial region composed of one seed point starts to grow iteratively by adding more neighboring pixels that satisfy some predefined criterion. This criterion can be based on intensity, texture, or edge information. One simple yet popular criterion is the intensity similarity among the region pixels. Let R_i be a set of pixels composing the growing region at the i^{th} iteration. Initially, the region is composed of a single seed point. That is,

$$R_0 \equiv \{(x^0, y^0)\} \quad (4.1)$$

Then at i th iteration, the region is given by this equation,

$$R_i = \begin{cases} R_{i-1} \cup \{(x, y)\} & \text{if } |\mu_{R_{i-1}} - I(x, y)| < T \\ R_{i-1} & \text{otherwise} \end{cases} \quad (4.2)$$

Where T is a predetermined threshold, $I(x, y)$ is the intensity of the candidate pixel (x, y) and μ_R is the mean intensity of the pixels inside region R defined as,

$$\mu_R = \frac{1}{n} \sum_{(x,y) \in R} I(x, y) \quad (4.3)$$

Where n is the cardinality of the set R

4.1.2. Limitations of region growing

Despite its simplicity and speed, a major limitation of the technique occurs at elevated noise levels and/or intensity non-uniformity of the region to be segmented [64]. In myocardial cine MR images, severe intensity variation are frequently encountered due to field in-homogeneity at the myocardium-lung and/or the flow and respiration artifacts. This was one of the reasons that region growing has not been used in left ventricle segmentation [65].

For example, figure (4.1.a) shows two images, the first is artifact free where the intensity variation inside the myocardium is very limited. On the other hand, figure (4.1.b) shows large intensity variation inside the myocardium due to respiratory motion. This significantly degrades the performance of RG as will be shown later.

Another limitation of using region growing in myocardial segmentation is the low-contrast interface between the LV and the liver which causes the growing region to extend beyond the actual borders of the myocardium [66].

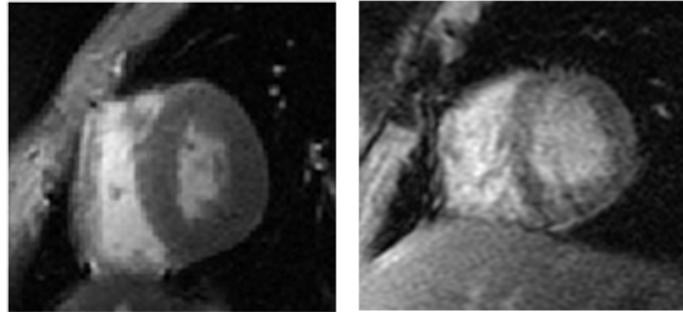


Figure 4.1 Short-axis image of the heart with a good quality (Left) another image with in-homogeneity artifacts (Right)

In this work, we propose to initialize the region growing with a number of seed points spread inside the myocardium at equiangular separations. This guarantees correct segmentation even if the myocardial pixel intensities are severely non uniform. In order to reduce the computation time, the growing region of each seed is constrained by an automatically determined surrounding sector of the myocardium.

The sectors of the different seed points are overlapping to guarantee the continuity of the extracted myocardium segment. In addition, using a priori knowledge of the intensity profile along radial lines of the myocardium, control points are set automatically to determine the epicardium near low-contrast interfaces (e.g. with liver).

4.1.3. Multi-Seeded Region Growing (MSRG)

In MSRG, m seed points are used to initialize m small regions whose union would form the segmented myocardium at the end of the growing operation.

For a given time frame, the seed points are selected automatically from an estimate of the interior myocardial contour. The latter can be estimated as the mean of the epi and endocardium contours of the previous time frame. We choose to select the seed points at equi-angles on the estimated interior contour as shown in figure (4.2).

In figure (4.2), the right image, we can see the four constraining areas represented with the four colors (red, gray, blue and green) and they are overlapped to guarantee the continuity of the region growing results and inside each region we have one white seed point distributed in the centers of each sector. And these constraining areas "sectors" have been used to limit the growing of the region in case of error (growing outside the right anatomical region) and also to limit the time of the technique from the programming perspective.

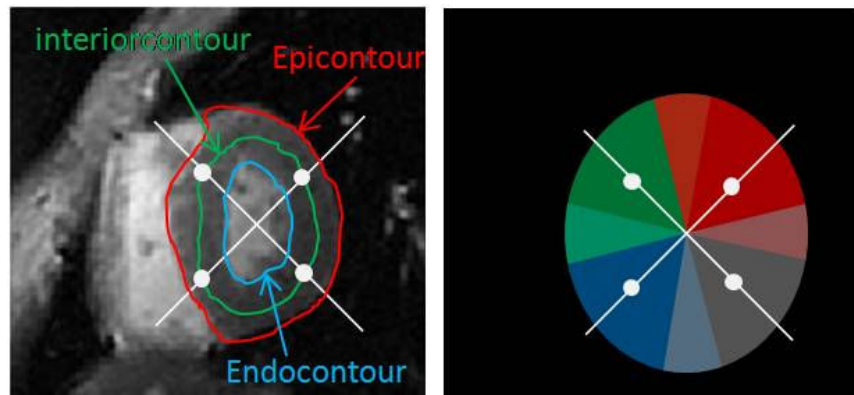


Figure 4.2 Short axis image with epi, interior and endocontour are drawn (Left) 4-constraining overlapped masks with their seed points (Right)



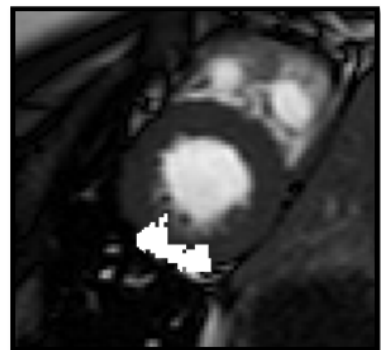
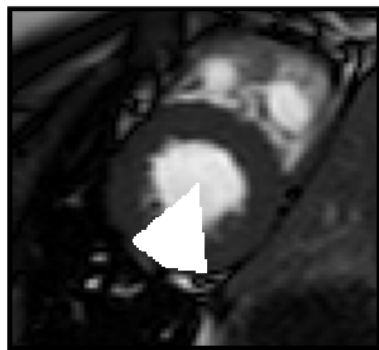
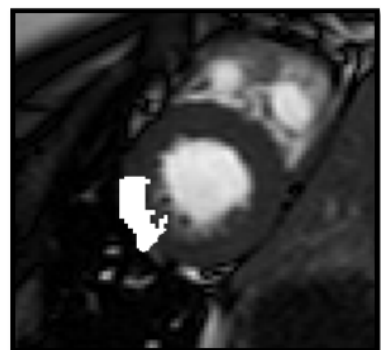
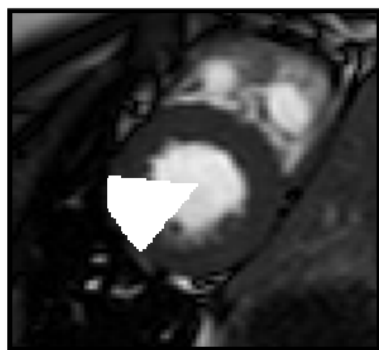
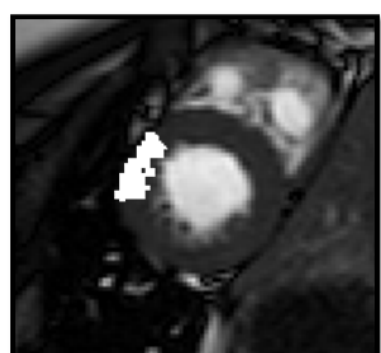
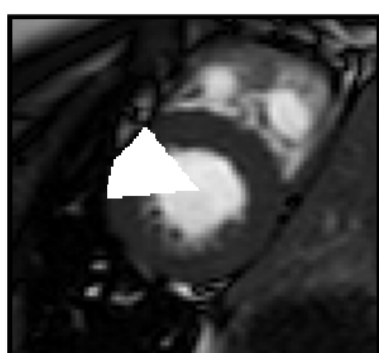
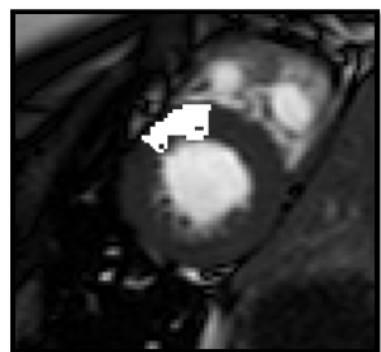
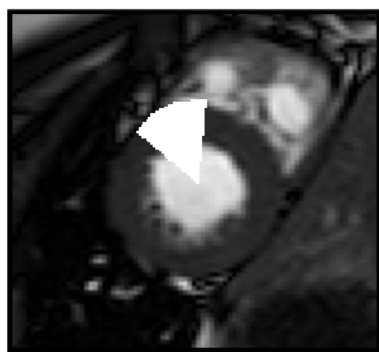
Figure 4.3 Short axis image with epi, interior and endocontour are drawn (Left) 4-constraining overlapping masks with their seed points (Right)

To avoid long computation time, constraining masks, CM^j , have been used to limit the circumferential and radial growing of the different regions, R^j . The masks are taken as overlapping sectors covering the entire area of the *LV* with one seed point lies inside each sector. Each region is thus allowed to grow according to the following equation,

$$R_0^j = \{(x_0^j, y_0^j)\} \quad (4.4)$$

$$R_i^j = \begin{cases} R_{i-1}^j \cup \{(x, y)\} & \text{if } |\mu_{R_{i-1}^j} - I(x, y)| < T \\ & \text{and } (x, y) \in CM^j \\ R_{i-1}^j & \text{otherwise} \end{cases} \quad (4.5)$$

Where (x_0^j, y_0^j) is the seed for region R^j and $j=1: m$. After the termination of the iterations, the segmented myocardium is taken as the union of the individual regions as shown in figure (4.4).



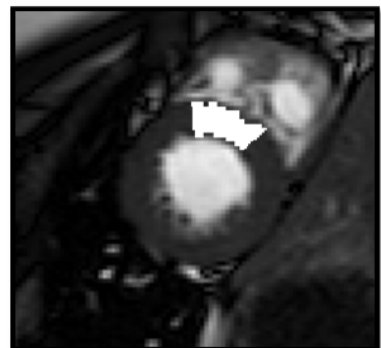
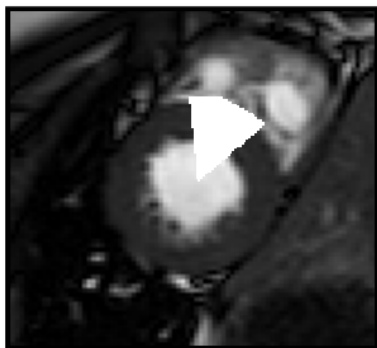
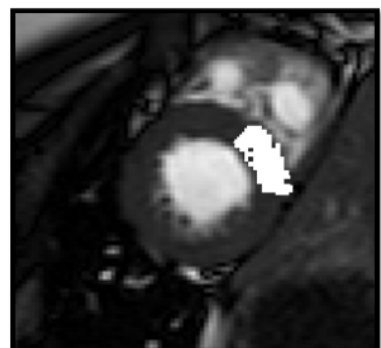
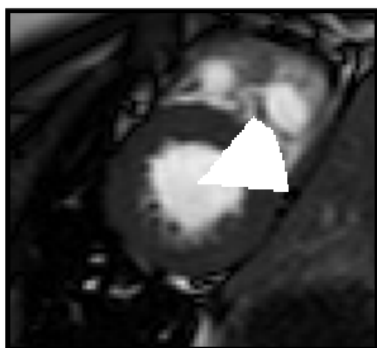
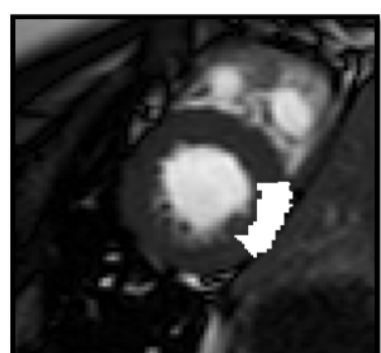
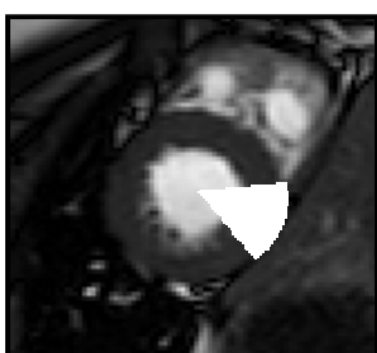
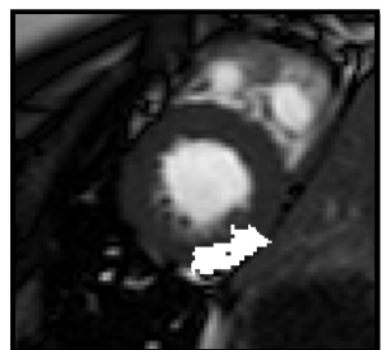
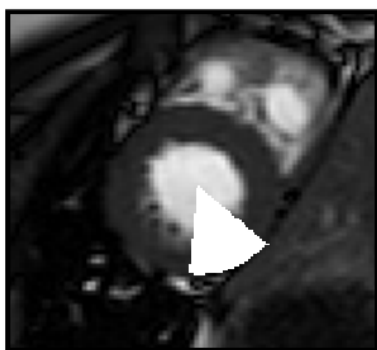


Figure 4.4 (Right images) Short axis image with sectors in white (Left images) result of region growing for each sector on the right image.

4.1.4. Morphological Operations

Morphological operations are affecting the form, structure or shape of an object [67].

Applied on binary images (black & white images – Images with only 2 colors: *black* and *white*). They are used in pre or post processing (filtering, thinning, and pruning) or for getting a representation or description of the shape of objects/regions (boundaries, skeletons convex hulls) [69].

The two principal morphological operations are dilation and erosion [68]. Dilation allows objects to expand, thus potentially filling in small holes and connecting disjoint objects. Erosion shrinks objects by etching away (eroding) their boundaries. These operations can be customized for an application by the proper selection of the structuring element, which determines exactly how the objects will be dilated or eroded.

The dilation process is performed by laying the structuring element B on the image A and sliding it across the image in a manner similar to convolution and it is represented by this notation,

$$A \oplus B \quad (4.6)$$

It is best described in a sequence of steps:

1. If the origin of the structuring element coincides with a 'white' pixel in the image, there is no change; move to the next pixel.
2. If the origin of the structuring element coincides with a 'black' in the image, make black all pixels from the image covered by the structuring element.

The structuring element can have any shape. An example is shown in figure (4.5) Note that with a dilation operation, all the 'black' pixels in the original image will be retained, any boundaries will be expanded, and small holes will be filled.

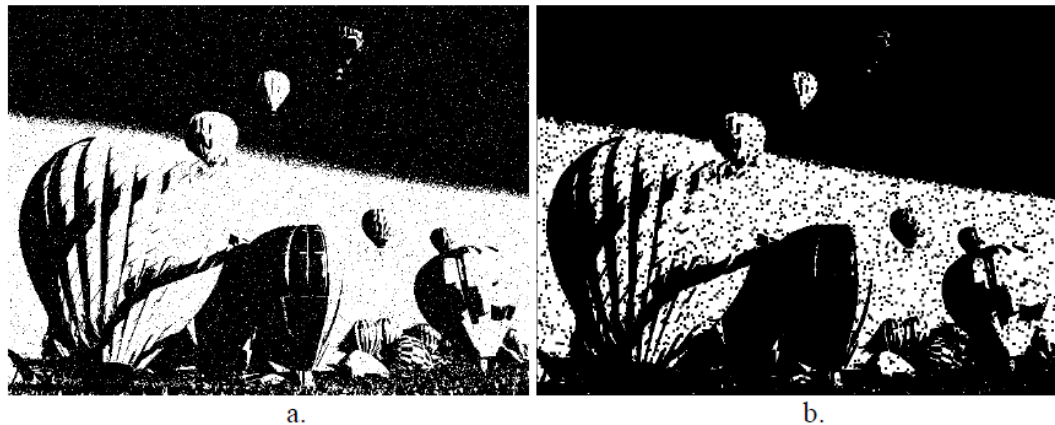


Figure 4.5 Example of the dilation (a) Original image (b) the result image.

The erosion process is similar to dilation, but we turn pixels to 'white', not 'black'. As before, slide the structuring element across the image and then follow these steps:

1. If the origin of the structuring element coincides with a 'white' pixel in the image, there is no change; move to the next pixel.

2. If the origin of the structuring element coincides with a 'black' pixel in the image, and at least one of the 'black' pixels in the structuring element falls over a white pixel in the image, then change the 'black' pixel in the image (corresponding to the position on which the center of the structuring element falls) from 'black' to a 'white'.

Its notation is as follows,

$$A \ominus B \quad (4.7)$$

In figure (4.6), the only remaining pixels are those that coincide to the origin of the structuring element where the entire structuring element was contained in the existing object. Because the structuring element is 3 pixels wide, the 2-pixel-wide right leg of the image object was eroded away, but the 3-pixel-wide left leg retained some of its center pixels.



Figure 4.6 Example of the erosion (a) Original image (b) The result image

Opening and closing These two basic operations, dilation and erosion, can be combined into more complex sequences. The most useful of these for morphological

filtering are called opening and closing [68]. *Opening* consists of an erosion followed by a dilation and can be used to eliminate all pixels in regions that are too small to contain the structuring element. In this case the structuring element is often called a probe, because it is probing the image looking for small objects to filter out of the image.

And the representative notation is:

$$A \ominus B = (A \ominus B) \oplus B \quad (4.8)$$

Closing consists of a dilation followed by erosion and can be used to fill in holes and small gaps. In figure (4.7) we see that the closing operation has the effect of filling in holes and closing gaps. Comparing the left and right images from figure (4.7), we see that the order of operation is important. Closing and opening will generate different results even though both consist of erosion and dilation.



Figure 4.7 Results of the opening (a) and closing (b) operations on the original image from figure (4.5) (a).

Through this manner we can use the binary images resulted from the modified region growing technique to close the holes and smooth the donut view representing the left ventricle tissue using the closing technique and smoothing using dilatation. In figure (4.8) we can see that we have got rid from the speckles and holes inside the myocardium tissue using the closing operation only.

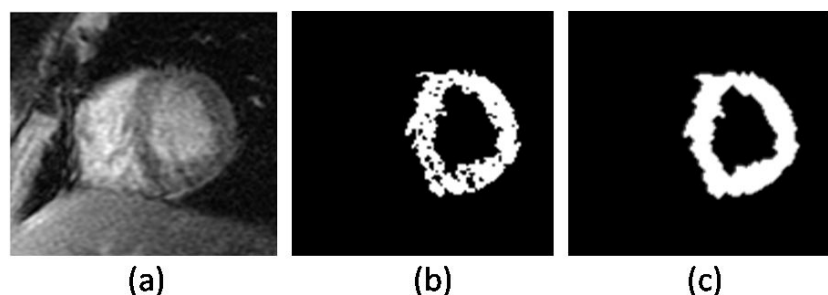


Figure 4.8 (a) Original Image (b) Segmentation result with black holes and speckles (c) result of closing operation

We have used also the dilation to smooth the inner and outer edges of the myocardium tissue with a disk structure element because the disc shape has the most curved edge so it will preserve the smoothness of the donut shape.

4.1.5. Epicardial Control Points

The resulting region from the MSRG technique may include non-myocardial tissues due to low contrast interfaces. This problem occurs mainly at the outer boundary. To avoid this problem, control points on the true interface boundaries are identified by means of feature matching and used to constrain the outer contour to the real epicardium. Thirty four datasets have been analyzed offline to learn the true location of the epicardial points at low contrast interfaces as follows.

First, the outer interface between the myocardium and all other tissues were delineated manually and the intensity profiles along radial lines at these interfaces were plotted. Then, these profiles have been classified into three main classes: myocardium-lung, myocardium-liver and myocardium-blood profiles. The mean profile of each class (shown in figure 3.c) is taken as a template for subsequent profile matching. The correct interface point along each interface was determined according to a certain criterion depending on the interface type. For the myocardium-liver interface, whose profile appears as inverted Gaussian, the minimum intensity index is set as the true interface point. For the myocardium-lung and myocardial-blood interfaces, the true interface points are determined as the first point on the profile satisfying intensity value smaller than 33% and 66% of the maximum profile

intensity, respectively. Those values (33% - 66%) have been concluded from studying the manual segmented contours and founding their positions on the profiles.

After determining interface profile templates and the rules for selecting the true interface points from these templates as shown in figure (4.9), the output of the MSRG technique is then processed as follows. The intensity profiles of all points on the outer contour are matched with the three interface templates. If matched with one of the templates, then the type of the interface and thus the location of the true interface points are estimated. This leaves the outer contour of the MSRG segmented region irregular and thus needs some smoothing.

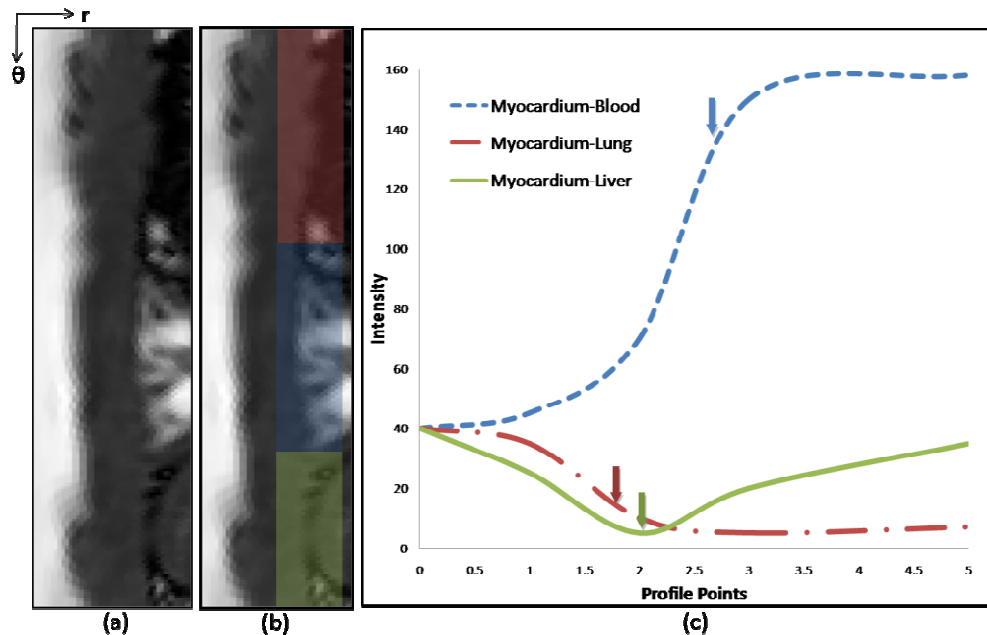


Figure 4.9 (a) A myocardium image shown in the polar representation showing different types of interfaces (b) Three regions are highlighted with the same color of their types in the next chart (c) Chart represents the three types of features.

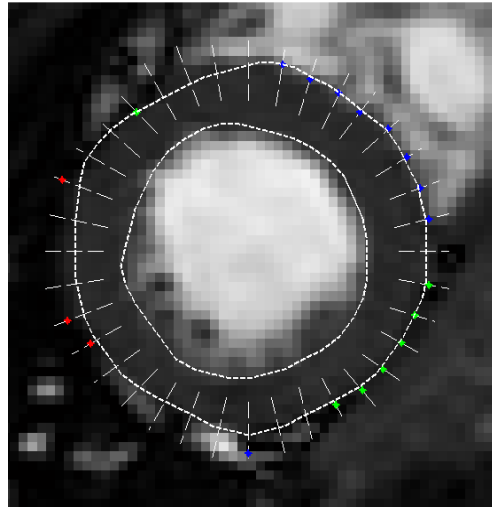


Figure 4.10 a short-axis CINE MRI image with the segmentation contours and the refined control points in the three colors

4.1.6. Refinement of the Contours using ACMs

After determining the control points, the outer and inner contours of the MSRG segmented region are then refined to smooth sharp bending segments by using a few iterations of standard active contour model [70] with the addition of some pressure forces like the balloon energy and next paragraph will make you more familiar with the active contour model (snakes).

Snake is a parametric curve defined within domain of an image. All snake properties and its behavior is specified through a function called energy functional by analogy with physical systems. A partial differential equation controlling the snake causes it to evolve so as to reduce its energy [71]. The physical analogy can be extended, and the motion of the snake can be viewed as being due to simulated forces acting upon it.

In order to gain an intuitive understanding of the snake model, it is therefore suitable to compare it with a real physical model.

The first snake model was proposed by Kass [70] in 1987. The energy functional which the snake was to minimize in order to achieve equilibrium was defined as following

$$E_{\text{snake}} = \int_0^1 \{E_{\text{int}}(v(s)) + E_{\text{image}}(v(s))\} ds$$

(4.9)

where the position of the snake on the image is represented parametrically by a planar curve $v(s) = (x(s); y(s))$, E_{int} represents the internal energy of the curve due to the bending and the E_{image} represents the image forces pushing the snake toward the desired object. The proposed internal energy model was defined as

$$E_{\text{int}} = (\alpha(s)|V_s(s)|^2 + \beta(s)|V_{ss}(s)|^2)/2, \quad s \in [0, 1] \quad (4.10)$$

where $v_s(s)$ is the first derivative and $v_{ss}(s)$ the second derivative of $v(s)$ with respect to s . Note that we assume continuous image and curve coordinates. In applications, we work with digital images and a discretization must be formulated. Since the object in interest should be recognized by the snake as a set of low values on the negative edge map, i.e. spatial gradient magnitude, the model for the image energy was defined as

$$E_{\text{ext}} = -|\nabla I(x, y)|^2 \quad (4.11)$$

If the object was homogeneous inside (both the boundary and the area inside the boundary have approximately the same grey level) or

$$E_{\text{ext}} = -I(x, y) \quad (4.12)$$

if the image is a line drawing (black on white). The term $I(x,y)$ represents the grey level values of the image. Let's now try to analyze it by viewing it in terms of our intuitive landscape model. The first derivative of $v(s)$ with respect to s gives us the rate of change of length of the curve, which means the longitudinal contraction of the curve. The coefficient $\alpha(s)$ allows the curve to have smaller or larger degree of contraction and therefore makes the snake act like an elastic string. Large values of $\alpha(s)$ mean large contraction of the snake in the direction of the force. Therefore $\alpha(s)$ denoted as the elasticity coefficient.

The second derivative gives us the rate of convexity or the curvature. The coefficient $\beta(s)$ regulates than the rate of the change of the curve in the direction normal to its boundary. This term makes the snake act like a rigid string. That means that the curve preserves the smoothness, the straight -line shape but does not contract.

If the value of $\beta(s)$ is high the curve is hard and resists bending, while small values of $\beta(s)$ is small allow the curve to develop a corner. By adjusting these two coefficients, the curve gets an appropriate elasticity and is able to embrace the object of interest.

The second energy term is easy to interpret. We can regard the image intensity function as a landscape and the snake is rolling down to a valley driven by gravity like force. If we think of the low values of the negative edge map as the valley, calculate the edge map over the image and make the snake go in the direction of the minima on the edge map, it will roll to the valley and stay there.

Having defined the various energy terms that derive the snake, the initial position must be interactively specified by the user or geometrically identified using predefined model.

Those are the principles behind the snake. It will be shown later that this model may be improved in many ways to be able to access our images with its different problems properties.

Actually active contour model has been used after the step of the control points' refinement to preserve the smoothness of the final curve. The resulted rough contour came from the low resolution of the image and there are tiny objects that are represented by just one or two pixels as shown in figure. So it will not preserve the smooth of the whole contour.

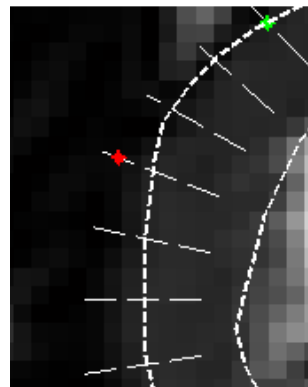


Figure 4.11 an image introduces the effect of the low resolution on the segmentation process

In our problem we are in need for the addition of pressure energy in the outward axial direction to keep our contour from shrinking because of the elasticity energy and this energy will be controlled by the cost function $\gamma(s)$ which control the effect of this energy and we will call it balloon energy and another important cause and it is that we

sometimes need to initialize the contour inside the myocardium and let it grow in the direction of the Epicardium.

Balloon energy will be computed by measuring the Euclidean distance between each point on the contour and the center of the contour itself and maximizing this Euclidean distance and this distance will contribute in the total balloon energy which is multiplied by the cost function $\gamma(s)$. To constrain the contour in the required place; in other words to keep the contour without shrinking because of the elasticity energy or to grow the contour as stated before, we will assign negative values to $\gamma(s)$ to minimize the total score.

4.1.7. Proposed Algorithm

The complete proposed algorithm is summarized in the flowchart in figure (4).

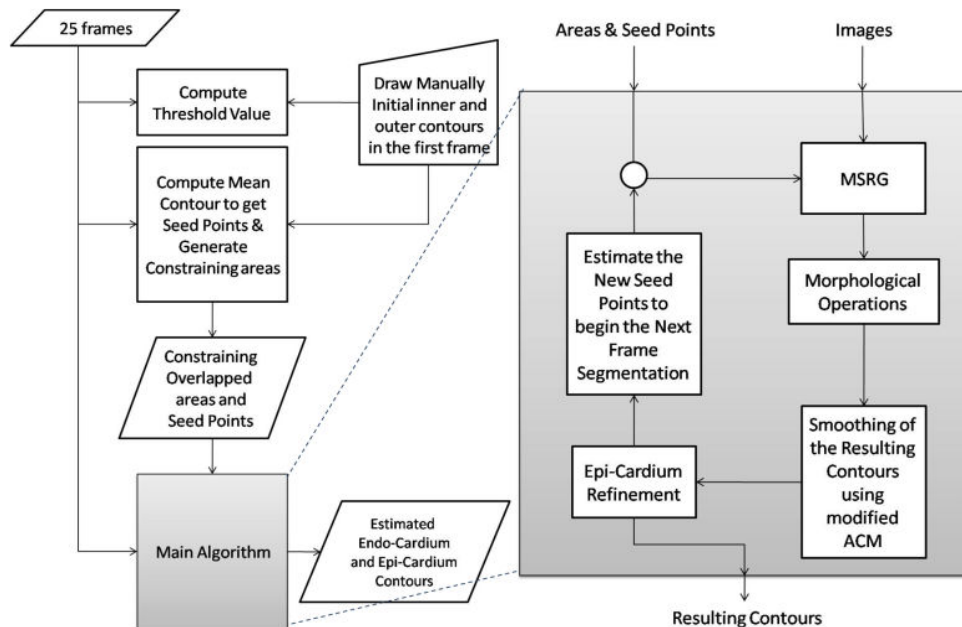


Figure 4.12 (Left) Flowchart of the whole proposed algorithm (Right) Detailed flowchart of the main algorithm block.

4.2. Adaptive Multi Seeded Region Growing using K-Means (Experiment 2)

4.2.1. Multi-Seeded Region Growing

The same method that have been clarified in section 4.1.3 will be used in this experiment but with small refinement concerning the computation of the sectors widths, number and threshold value for the region growing algorithm. Also the size of the sectors is not the same like the previous experiment, it has different arc lengths. The positions and widths of the sectors have been estimated by the classification of the mean profile using k-means which will be explained in section 4.2.3.

4.2.2. Seed Points and Constraining Areas Selection

It has been found that the best source of information to get the suitable places of seeds and constraining areas is the intensity profile of the middle contour. Because it reveals some information about the homogeneity distribution inside the myocardium in the circumferential direction but it does not give us more information in the radial direction and consumes more time in computation, so this direction's information has been ignored.

4.2.3. K-Means

To extract this information using just the image intensities under the middle contour, k-means has been used to cluster the intensity profile signal into a predefined number of clusters using only two features: the distance between the points of the profile and the intensities of these points. So any two points/clusters have closer values of

intensity and positions can be combined to the same cluster. Also the centers of these resulted clusters can be used as seed points for the region growing technique.

The main idea about k-means is that we want to minimize the following objective function,

$$J = \sum_{j=1}^k \sum_{i=1}^n \|x_i^{(j)} - C_j\|^2, \quad (4.13)$$

Where $\|x_i^{(j)} - C_j\|^2$ is a chosen distance measure between a data point $x_i^{(j)}$ and the cluster center C_j is an indicator of the distance of the n data points from their respective cluster centers.

So k-means algorithm is composed of the following steps as stated in [72]:

1. Place K points into the space represented by the objects that are being clustered.
These points represent initial group centroids.
2. Assign each object to the group that has the closest centroid.
3. When all objects have been assigned, recalculate the positions of the K centroids.
4. Repeat Steps 2 and 3 until the centroids no longer move. This produces a separation of the objects into groups from which the metric to be minimized can be calculated.

It can be shown in figure (4.13) that the middle contour profile has different trends and continues regions containing these trends. But there is a problem in the high variations of the curve because of the noise and to solve this problem and make this

profile more meaningful we have smoothed the curve with an acceptable degree without affecting the details of the profile.

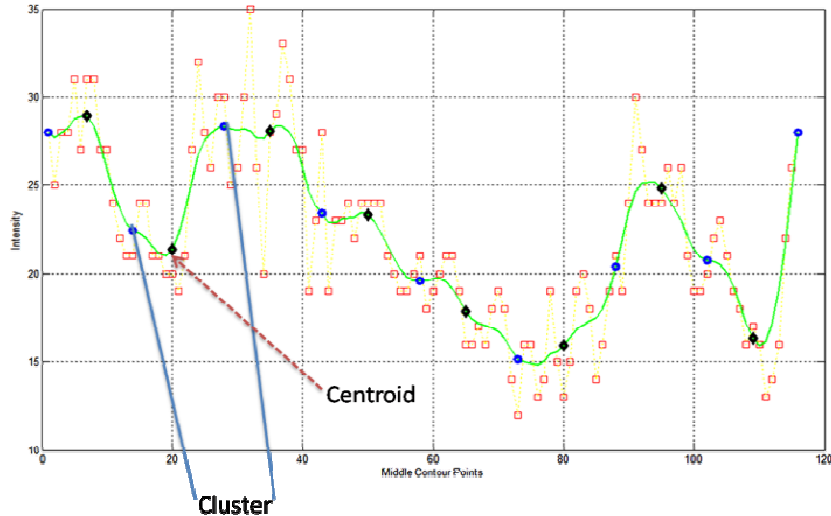


Figure 4.13 the curve in yellow represents the original profile and the profile of the mean contour after smoothing is in green with the classification results using k-means. Each classified sector is limited between each two successive blue points. And the black point is the centroid of each sector.

4.2.4. Proposed Algorithm

The complete proposed algorithm is summarized in the flowchart in figure (4).

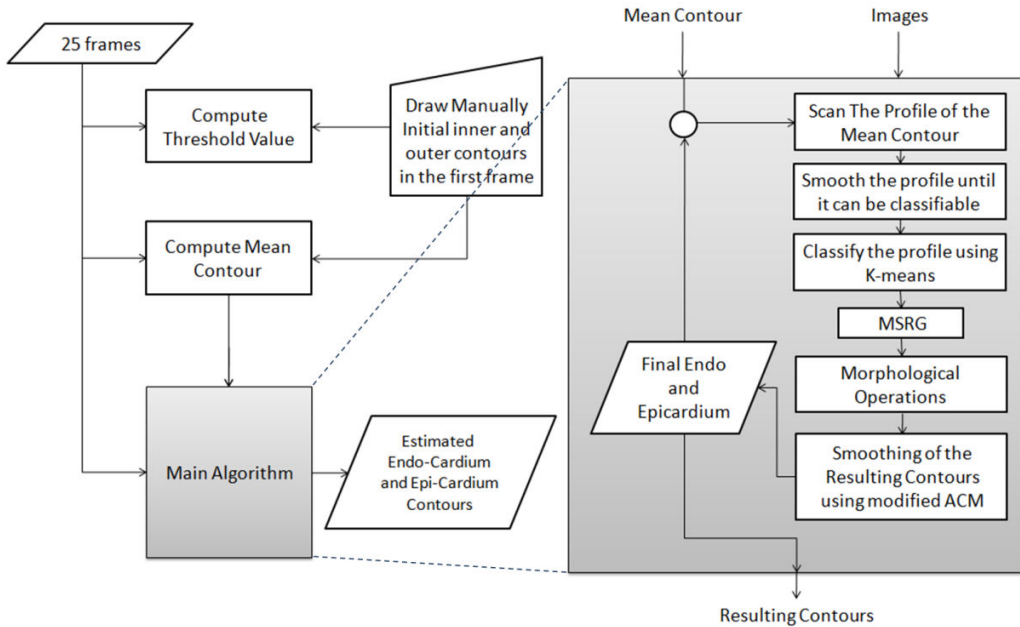


Figure 4.14 Flowchart of the whole proposed algorithm (Left) Detailed flowchart of the main algorithm block (Right)

4.3. Automatic Evaluation Methods

Automatic evaluation methods are numerous but in our case we can use only three types of performance evaluation techniques which are the average perpendicular distance, the dice metric, accuracy measurements and the visual (manual) evaluation. Each one of them has its advantages and drawbacks and they will be illustrated in the next sections.

4.3.1. Average perpendicular distance

The average perpendicular distance measures the distance from the automatically segmented contour to the corresponding manually drawn expert contour. Then we average all these distances over all contour points. A high value implies that the two

contours do not match closely and there is a big difference. Also maximum and minimum Euclidean distances can be computed to show how much the error is distributed all over the contour points.

But it suffers from some losses of information about the intra un-segmented parts of the segmented region. This problem will happen if the resulted binary image from the region growing has some black holes like what is shown in figure (4.8.b). Another type of losses will happen if my target is to segment the LV papillary muscles and trabeculations or include them into my consideration.

Figure (4.15) represents the average perpendicular distance technique so we have three colors of lines red, green and blue and they are representing the automatically segmented epicardium contour, the manually segmented epicardium contour and the perpendicular distances respectively.

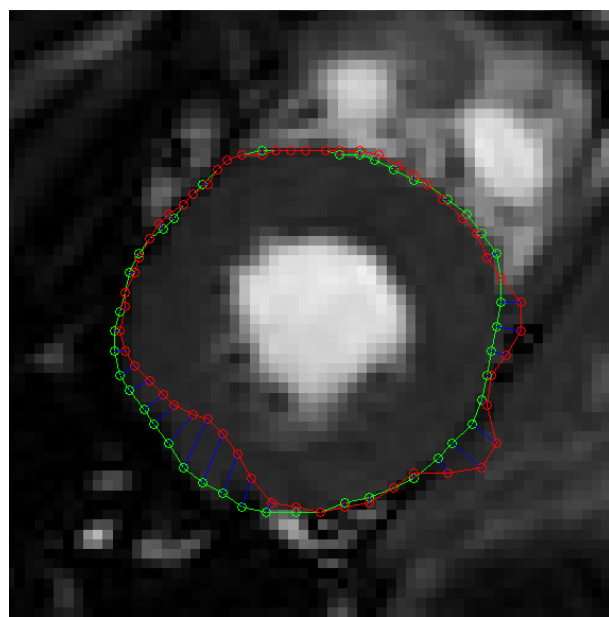


Figure 4.15 The average perpendicular distance between two contours

The perpendicular distances have been computed by getting the absolute Euclidean distance because we are going to compute the global or accumulated error. As an example we can see in the right part of the contour that the red contour or the estimated contour is going far from the true contour so we can say that there is a positive error and the negative error has happened in the down left part of the contour.

The global error will be computed by the following equation,

$$APD = \frac{\sum_{i=1}^n \|P_{Manual_i} - P_{Automatic_i}\|_2}{n} \quad (4.14)$$

Where n is the number of points forming the contour and P_{Manual_i} represents the i^{th} point on the manual segmented contour and $P_{Automatic_i}$ represents the i^{th} point on the automatically segmented contour.

4.3.2. Dice metric

The Dice metric is a measure of contour overlap utilizing the contour areas automatically segmented A_a , manually segmented A_m , and their intersection A_{am} [73]. DM is always between 0 and 1, with higher DM indicating better match between automatic and manual segmentations.

$$DM = \frac{2A_{am}}{(A_a + A_m)} \quad (4.15)$$

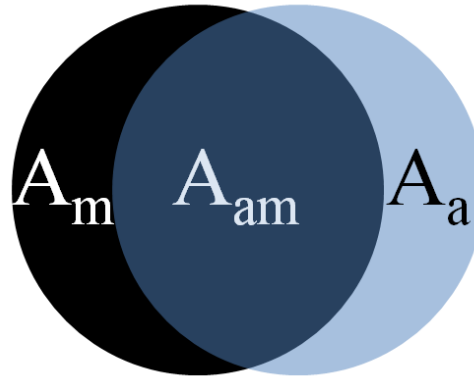


Figure 4.16 The parameters used by the Dice metric

4.3.3. Accuracy Measurements

In this type of evaluation, the performance can be measured also in another way using the computation of the sensitivity, specificity and precision. These measurements can be computed if we know the TP true positive, TN true negative, FP false positive and FN false negative values.

And they can be computed by the following relationships

$$TP = A_{am}, \quad (4.16)$$

$$TN = I_{area} - A_a - A_m + A_{am}, \quad (4.17)$$

where I_{area} is the area of the whole image.

$$FP = A_a - A_{am} \quad (4.18)$$

$$\text{and } FN = A_m - A_{am} \quad (4.19)$$

4.3.4. Visual (Manual) Evaluation Method

Visual Assessment: An experienced cardiologist will rate the segmentation results from testing datasets on a visually-based 4-point scale, for each of the following:

1. Accuracy of the contours delineating the LV papillary muscles and trabeculations, suitable for LV Mass calculation; and
2. Accuracy of the LV myocardial contours, suitable for EF calculation.

4.3.5. Another Parameters that's taken into account

Manual steps: Number of manual steps (e.g. key presses or mouse clicks) required to initialize the automatic segmentation stage, if any.

Computation time: The average computation time to complete the ES and ED segmentations on all slices for the automatic stage of the procedure.

BLACK BLOOD IMAGES CLASSIFICATION

In this Black-blood cardiac Magnetic Resonance Imaging (MRI) technique the blood signal is nulled to increase the contrast-to-noise ratio (CNR) of myocardium-background and to avoid the flow artifacts because of the blood. Aletras et al [74] proposed an acquisition technique for acquiring cardiac images with black-blood contrast. Nevertheless, the technique could null the blood signal only at one specific time instance during the cardiac cycle and thus cannot produce cine sequence. This limitation prohibits using the technique in the assessment of the heart motion. Another technique that can be used to produce cine sequence with black-blood contrast was proposed by Frahm et al and known as STEAM [75]; unfortunately, the use of STEAM was hindered by severe deformation-dependent artifact that has been reported by many researchers [75,76]—such as fading of the signal.

To overcome these limitations, Fahmy et al proposed a modified STEAM-based technique that successfully 1) corrects the STEAM artifacts, and 2) produces cardiac cine sequences with black-blood contrast [77]. However, as good as modified STEAM is, it suffers from low CNR, and there is a great need to enhance this poor CNR by reducing the level of background noise signal. Methods for denoising exist, but they are not optimal for the case of modified STEAM suggested by Fahmy et al. In this chapter we propose a technique to reduce the background noise in the modified STEAM images and SENC images [78]. Also we explore the use of other methods of denoising and their results. Numerical simulation and quantitative studies were done

to compare the performance of the used methods. Finally, validation on real MRI modified STEAM images was performed [79, 80].

5.1. Modified STEAM for Black Blood Imaging

The basic idea behind the modified STEAM technique is to acquire two black-blood STEAM image sequences with complementary image intensity. That is, one sequence captures static and low deforming tissues while the other captures highly tissues. The two image sequences are then combined to remove this deformation dependency. In the noise-free case, given a time frame t , the signal intensities at a pixel (x, y) in the acquired images was shown by [77] to be

$$S_1(x, y, t) = \frac{1}{2}p(x, y)\text{Sinc}(\delta\omega(x, y, t)), \quad (5.1)$$

$$S_2(x, y, t) = \frac{1}{2}p(x, y)\text{Sinc}(1 - \delta\omega(x, y, t)), \quad (5.2)$$

where $p(x, y)$ is the signal component representing the water proton density inside the tissues at the pixel (x, y) ; and $\delta\omega(x, y, t)$ is a deformation-dependent term related to the tissue strain, $\varepsilon(x, y, t)$, through the equation:

$$\delta\omega(x, y, t) \propto \frac{\varepsilon(x, y, t)}{1 - \varepsilon(x, y, t)}. \quad (5.3)$$

The deformation-dependent effect is removed by the summation of the two images and using special correction weights to extract the true signal, $p(x, y)$,

$$p(x, y) \approx \frac{S_1(x, y, t) + S_2(x, y, t)}{W(\partial\hat{\omega}|_{(x, y, t)})}, \quad (5.4)$$

where $W(\cdot)$ is a weighting function that depends on $\delta\omega$, which can be estimated, as described in detail in [75,78] by,

$$\partial\hat{\omega}(x, y, t) = \frac{S_2(x, y, t)}{S_1(x, y, t) + S_2(x, y, t)}. \quad (5.5)$$

It is worth noting that, in actual images, although the blood signal is nulled in the acquired STEAM sequences, the background areas in the reconstructed sequence, $\hat{\mathbf{p}}(x, y)$, obviously are not identical to zero due to the noise effect. The following section proposes a more realistic signal model that takes into account the stochastic nature of the acquired signal.

5.2. Stochastic Model

In order to account for the noise effect, a probabilistic model was used for the signal intensity of the STEAM images based on the well-known MRI signal model of the Rician and Rayleigh probability density functions [81] for the tissue and the background signals respectively. That is,

$$f_S(S|tissue) = \frac{S}{\sigma^2} \cdot e^{-\frac{\mu^2+S^2}{2\sigma^2}} \cdot I_0\left(\frac{\mu S}{\sigma^2}\right), \quad (5.6)$$

$$f_S(S|bkgrnd) = \frac{S}{\sigma^2} \cdot e^{-\frac{S^2}{2\sigma^2}}, \quad (5.7)$$

where I_0 is the zeroth order modified Bessel function of the first kind; S denotes the pixel signal of the magnitude image; σ is the standard deviation of the contaminating

noise, which can be estimated with high accuracy from the image background areas; and μ is the true mean of the signal S , which can be given by equation (5.1) and (5.2). Using the fact that the two images S_1 and S_2 are acquired independently, we can easily show that the joint density function of their signal intensities (at the same pixel location) can be written as,

$$\begin{aligned} f_{S_1 S_2}(S_1 S_2 | tissue) &= f_{S_1}(S_1 | tissue) \cdot f_{S_2}(S_2 | tissue) \\ &= \frac{S_1 S_2}{\sigma^4} \cdot e^{-\frac{p^2 \cdot sinc(\partial\omega)^2 + p^2 \cdot sinc(1-\partial\omega)^2}{2\sigma^2}} \cdot e^{-\frac{S_1^2 + S_2^2}{2\sigma^2}} \cdot I_o\left(\frac{p \cdot sinc(\partial\omega) \cdot S_1}{\sigma^2}\right) \cdot I_o\left(\frac{p \cdot sinc(1 - \partial\omega) \cdot S_2}{\sigma^2}\right) \end{aligned} \quad (5.8)$$

and,

$$f_{S_1 S_2}(S_1 S_2 | bkgrnd) = f_{S_1}(S_1 | bkgrnd) \cdot f_{S_2}(S_2 | bkgrnd) = \frac{S_1 S_2}{\sigma^4} \cdot e^{-\frac{S_1^2 + S_2^2}{2\sigma^2}}. \quad (5.9)$$

5.3. Classification Techniques

5.3.1. Bayesian Classifier

As mentioned above, we will develop algorithms to identify the background regions in the reconstructed sequence, $\hat{p}(x, y, t)$, and suppress their signal. In this work, a feature vector $\bar{v} = [S_1(x, y), S_2(x, y)]$ is used to represent the information available for each pixel (x, y) in the sequence $\hat{p}(x, y)$. Based on the Bayes classifier technique [82],

all feature vectors are then classified into two classes, background and tissues, as follows. First, a Bayes discriminant function is built using the joint probability function in equations (5.8) and (5.9),

$$d(\bar{v}) = \log(f_{S_1 S_2}(S_1, S_2 | tissue)) - \log(f_{S_1 S_2}(S_1, S_2 | bckgrnd)). \quad (5.10)$$

Based on the above equation, the decision rule for the classification is,

$$pixel(x, y) = \begin{cases} \epsilon bckgrnd, & d(\bar{v}) < 0 \\ \epsilon tissue, & d(\bar{v}) > 0 \end{cases}. \quad (5.11)$$

Besides this Bayesian classifier, three other types of classifiers are used based on simple thresholding which we will refer to them as the Linear Classifier, the Quadratic Classifier, and the Rectangular Classifier, respectively.

5.3.2. Linear Classifier L₁-Norm

In the next three types of classification a simple threshold was used to classify the background and tissue signal. For a thresholding technique, it is important to obtain the threshold value. We are using two methods to obtain the threshold value. The first is the estimation of the standard deviation of the background signals by taking a region in the background and computing $\hat{\sigma}$ using

$$\hat{\sigma}^2 = \frac{1}{2N} \sum_{(x,y) \in R} \hat{p}(x, y)^2, \quad (5.12)$$

where R is a background region of size N pixels (shown as a white rectangle in figure (5.1)). The threshold can be written as

$$\text{Threshold} = 1.3 \times \hat{\sigma}. \quad (5.13)$$

The other method for finding the threshold value is by computing the mean intensity in two regions, one in the background and one in the tissue, using the

$$\text{Threshold} = \frac{(\mu_{\text{tissue}} + \mu_{\text{bckgrnd}})}{2}, \quad (5.14)$$

where μ_{tissue} is the mean value of the tissue signals and μ_{bckgrnd} is the mean value of the background signals. In the Linear type of classification we use the L¹ Norm defined as

$$\|x\|_1 = |x_1| + |x_2| \quad (5.15)$$

Therefore, if the intensities of two points satisfy the following inequality,

$$\text{Threshold} > |S_1| + |S_2|, \quad (5.16)$$

this pixel then represents a background.

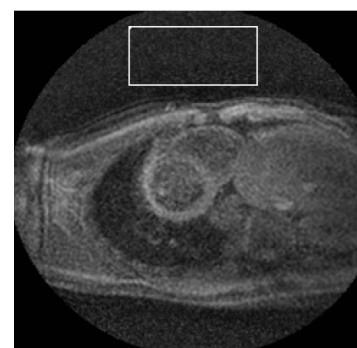


Figure 5.1 the region from the background that was taken to calculate the standard deviation

5.3.3. Quadratic Classifier L₂-Norm

In this type we use the L² norm as described in this equation,

$$\|x\|_2 = (x_1^2 + x_2^2)^{1/2} \quad (5.17)$$

The threshold value is required also so the threshold will be estimated using the equations in (5.12, 5.13) because it is a value of threshold that is independent on the tissue signals and purely dependent on the back ground signals. After that classification takes place using this relation,

$$Threshold > \sqrt{(S_1^2 + S_2^2)} \quad (5.18)$$

Using this relation we classify each pixel of the images and null each pixel identified as background.

5.3.4. Rectangular Classifier L_{inf}-Norm

In this type of classification it is important to compute the threshold value using the equations in (5.12, 5.13) and the decision function will be as follows,

$$Threshold > S1 \text{ & } Threshold > S2. \quad (5.19)$$

5.4. Numerical Simulation

A numerical simulation was done to illustrate the feasibility of using the proposed method for differentiating the background from the tissue regions. Two simulations were done to study the following two cases separately.

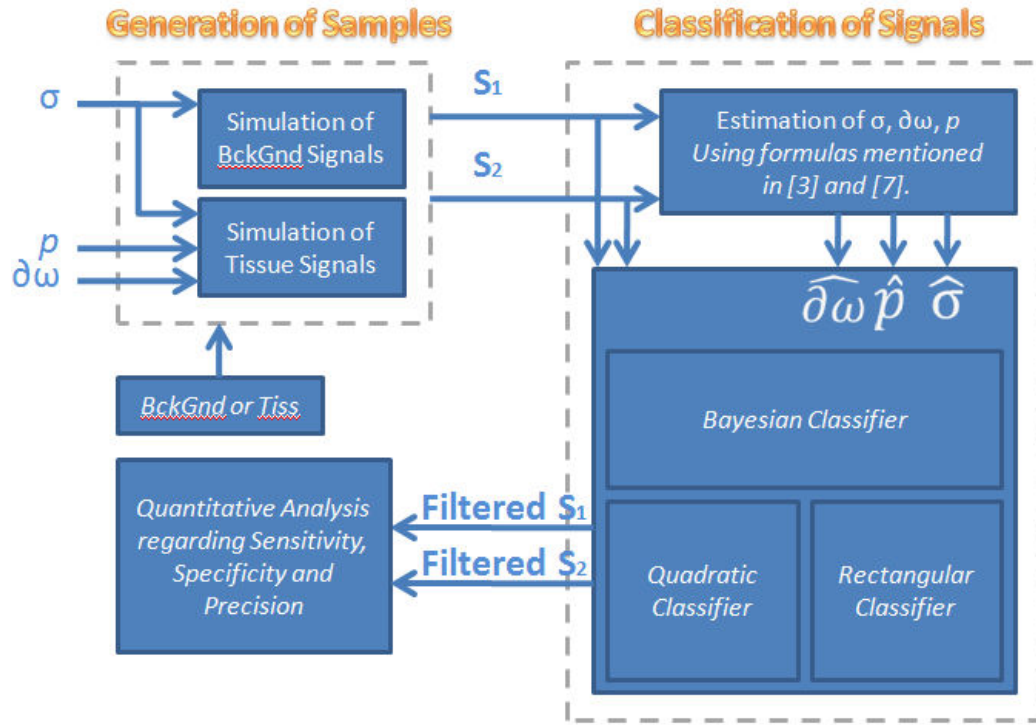


Figure 5.2 Simple block diagram illustrates the steps of our experiment beginning with the signal simulation finishing with the decision making.

5.4.1. Case1: Background Signal

The background signal in images S1 and S2 was generated using a Rayleigh number generator. A range of standard deviation $\sigma = 40:90$ was used to generate 100,000 pair of signal intensity samples and the vector $\bar{v} = [S_1 \ S_2]$ was created for each sample. This set of vectors was created for each value of σ . Figure (5.3) shows a plot of the

joint probability density function of S_1, S_2 for the generated samples at each value of σ . This large number of samples was generated to remove any source of dependency and to increase the degree of randomness. Sets of vectors were generated with different values of σ to simulate multiple signals to noise ratio values so that the judgment of the proposed method became fairer.

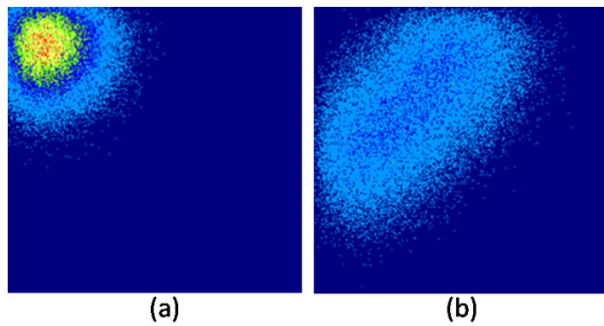


Figure 5.3 The Joint PDF of signal intensities S_1 and S_2 for: (a) the background and (b) tissue samples

5.4.2. Case2: Tissue Signal

In order to simulate the signal intensities of the tissues, Rician random variables were generated on the form:

$$S_1 = \sqrt{(n)^2 + (n' + p \cdot \text{sinc}(\delta\omega))^2}, \quad (5.20)$$

$$S_2 = \sqrt{(m)^2 + (m' + p \cdot \text{sinc}(1 - \delta\omega))^2}, \quad (5.21)$$

where p was set to 255 and the variables m, n, m', n' are independent Gaussian random variables with zero mean and a range of standard deviation $\sigma = 40:90$. This

simulation corresponds to different signal to noise ratios of $20 \log(255/\sigma)$ (which is the SNR value of the MRI data set, as will be shown later). The variable $\delta\omega$ was varied from 0 to 1 to simulate different levels of tissue deformation. As in the above case, 100,000 pair of signal intensity samples and the vector $\bar{v} = [S_1, S_2]$ was created for each sample. Figure (5.3) shows a plot of the joint probability density function of S_1 versus S_2 for the generated samples, and then all classification techniques are applied and tested using the three terms of accuracy that will be mentioned later.

5.5. Real Images Test

To validate the proposed method, it was tested using real MRI data. A human volunteer was imaged using the modified STEAM technique to capture 12 time frames for a short-axis cross-section of his heart. At each time frame, equations (5.1) and (5.2) were used to reconstruct a black sequence, $p(x, y)$. Only 1 time frame out of acquired twelve time frames are shown in figure (5.1) filter the background noise, first, the standard deviation of the background noise was calculated using the maximum likelihood described in equation (5.12), In order to identify the background regions, the proposed Bayesian decision rule was applied to the image in figure (5.1) shows the block diagram of the Bayesian classifier technique.

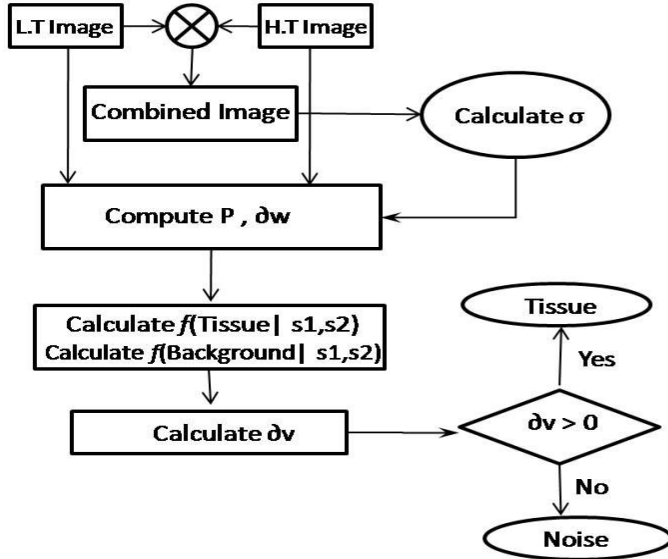


Figure 5.4 Block Diagram of the Bayesian classifier system using real images

Beside this technique two other techniques were also used which are the l-norm and the global threshold techniques. In the l-norm we used L^1 Norm, L^2 Norm and L^∞ Norm which are calculated from the equations (5.16), (5.18), (5.19) respectively, where S_l is the signal acquired from the L.T image while S_2 is the signal acquired from H.T image. So when applying the technique, first check whether the L Norm at every pixel is less than certain threshold or not, as if it exceeds this value it will be an indication that this pixel is tissue and if it is less than this value it will be considered as a background. Different threshold values were tested and it was noticed that the value that is equal to $\mu + \sigma$, where μ and σ are the mean and standard deviation of the background region in the $p(x, y)$, gave the best results and optimal values of

sensitivity and specificity for the $p(x, y)$. Also for the L^2 Norm when the threshold value multiplied by 0.75 the results were enhanced, and the same for the L^∞ Norm when it was multiplied by 0.65 results were enhanced at high extent. Figure shows the joint probability density function for the background region in the L.T and H.T images, and the behavior for L^1 Norm, L^2 Norm and L^∞ Norm are shown in solid, dashed and dotted line respectively.

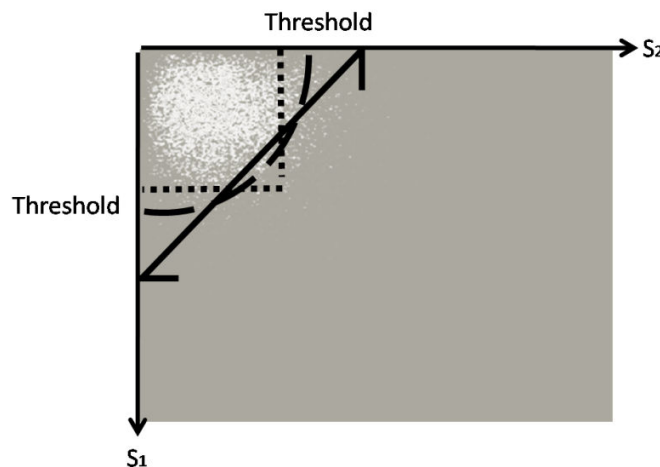


Figure 5.5 Simple block diagram illustrates what are the steps of the simulation of the Bayesian technique & the other two techniques.

The reason for not increasing the threshold value is to avoid considering the tissue pixels as background pixels and consequently decrease the specificity.

5.6. Further Processing

The results of the Bayesian method can be enhanced more by applying morphological operators like small regions removing and holes filling which have been discussed in chapter 4 in the morphological operation section. This step is a very important step to introduce some spatial information and grouping tasks into the resulted segmentation binary image. Figure (5.6) shows the processing flow from the low tune and high tune images to the final tissue segmented image.

In this flow we begin with the combination process for the two low and high tune images which are shown in figures (5.6.a)-(5.6.b) then classify the resulted (combined) image in figure (5.6.c) into tissue and background classes using the Bayesian classifier.

The resulted binary image in figure (5.6.d) which represents the decision for each pixel using Bayesian classifier can be used as an input image for the morphological operations block which consists of some closing operations (dilation then erosion) to fill the black holes and smooth the edges of the segmented tissue part.

The morphed binary image in figure (5.6.f) can be multiplied by the combined image to generate the final classified image which is shown in figure (5.6.g) using the AND operation.

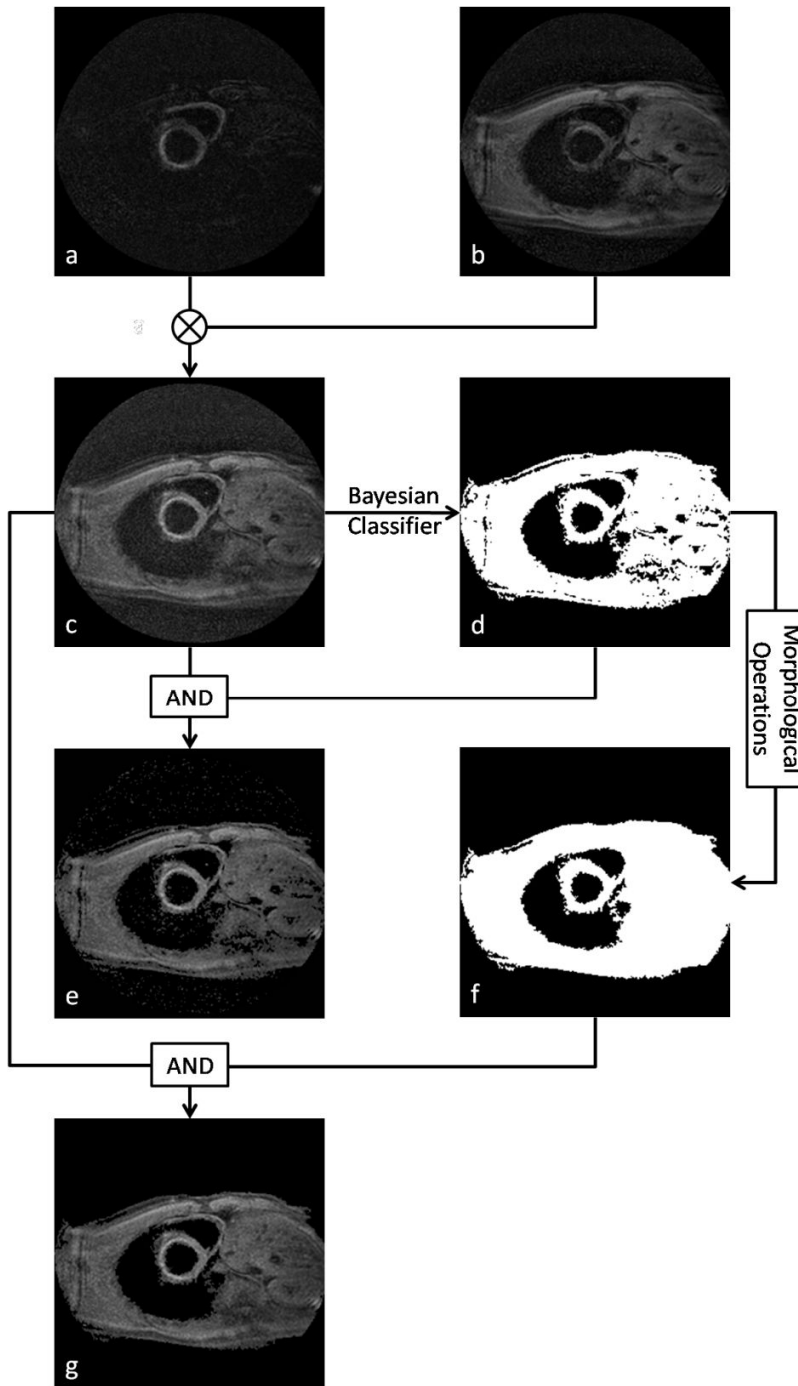


Figure 5.6 Simple block diagram illustrates what are the steps of the simulation of the Bayesian technique & the other two techniques.

5.7. Performance Evaluation Methods

Sensitivity, Specificity and Precision are statistical measures of the performance of this binary classification test. So these three parameters have been calculated for each method with different SNR values. Sensitivity in our case is the ability of the classifier to identify the background signals and it has the formula,

$$\text{Sensitivity} = \frac{TP}{(TP + FN)}, \quad (5.22)$$

where TP (true positive) is the number of vectors that have been identified as background vectors by the classifier and they are really background vectors, it can be called true background, FN (false negative) is the number of the vectors that have been identified as tissue vectors by the classifier and they are really background vectors. Specificity is the ability of the classifier to identify the tissue signals and it has the formula,

$$\text{Specificity} = \frac{TN}{(TN + FP)}, \quad (5.23)$$

Where TN (true negative) is the number of vectors that have been identified as tissue vectors by the classifier and they are really tissue vectors, it can be called true tissue, FP (false positive) is the number of the vectors that have been identified as background vectors by the classifier and they are really tissue vectors. Precision has the formula,

$$\text{Precision} = \frac{TP}{(TP + FP)} = \frac{\text{Sens}}{(1 - Spec + Sens)}. \quad (5.24)$$

CINE SEGMENTATION RESULTS & DISCUSSION

In this chapter, results of the two experiments will be shown and each experiment has its internal steps that have their own results as a pipeline of processes.

The first experiment is the multi seeded region growing with fixed number and sizes of sectors and in this experiment, the number of sectors and the overlapping ratio will be evaluated by testing all the available datasets to give good results for all the images.

The second experiment is the multi seeded region growing with varied number and sizes of the sectors which constraints the growing as stated in the methods chapter. In this experiment, the number of the sectors and their sizes will be evaluated automatically using the k-means as shown in the CINE segmentation chapter. And all the results related to the steps of this experiment will be shown in the next sections.

In this chapter we demonstrate some of the results obtained by running our algorithm on short-axis CINE MRI data sets. Each complete data set contains from 8 to 14 slices of short-axis MR images, each slice captured at 16-25 phases or frames. Unless otherwise specified, the presented results are generated using the fifth slice of the sample data sets. The original size of each 2D scan is 256*256 pixels.

Processing each frame takes approximately 936ms on Core2Duo, 2.26GHz, running Windows Vista. All Processing are in Matlab. Finally, quantitative measures, comparing our method with the hand-segmented data are presented in the last section.

6.1. Multi Seeded Region Growing with fixed Sectors sizes (Experiment 1)

Results

In the first experiment, results of application of simple region growing will be introduced in the next section; the results of the multi-seeded region growing also will be shown and discussed in the next sections and the impact of control point refinement and active contour model will be shown also.

The picking of the best threshold value, number of sectors and overlapping ratio will be illustrated in this section also beside that we will talk about the drawbacks of this algorithm.

6.1.1. Simple Region Growing

Figure (6.1) shows the result of applying simple region growing on a mid-slice short-axis image using threshold value equal to 25. It is obvious that the original image has a good quality and high homogeneity, so that the result is good in the right image but there are some small holes inside the myocardium.

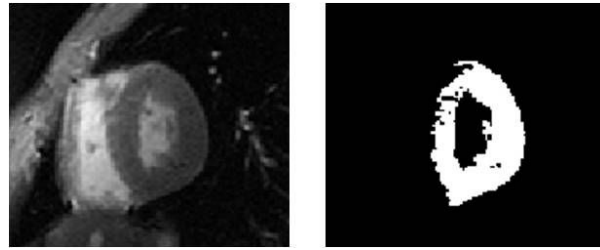


Figure 6.1 Short-axis image (Left) Result of applying the simple RG (Right)

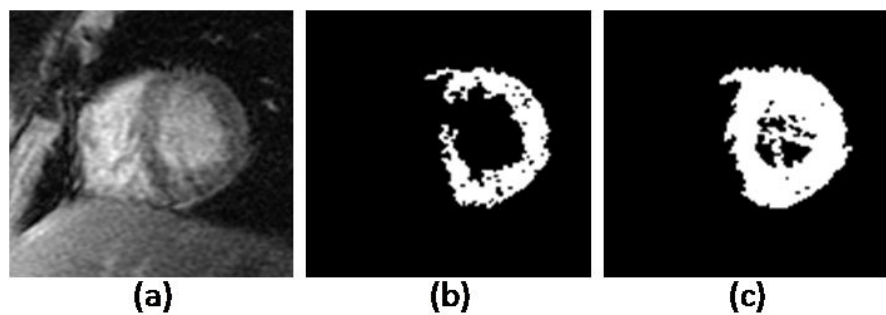


Figure 6.2 (a) Original image (b) Result of applying region growing with threshold = 27 (c) Another result using threshold = 52

Another image with bad quality is shown in figure (6.2.a), the MSRG technique gave bad results as shown in (6.2.b) and the region discontinuity also is shown. To recover this error the only way to route is to increase the threshold value and the resulted region from this raise is shown in (6.2.c), there is over estimation for the myocardium tissue and the technique begin to identify the blood in the cavity as tissue. Then the raising in the threshold value will not solve the in-homogeneity problem.

6.1.2. Multi Seeded Region Growing constrained by Overlapped Sectors

The final result of MSRG is the union of the multiple sectors m resulting as stated before. Then internal and external contours can be segmented using boundary tracing.

The result of applying MSRG is shown in figure (6.3) using no of sectors = 10, overlapping ratio = 0.1 and two different threshold values 21, 29.

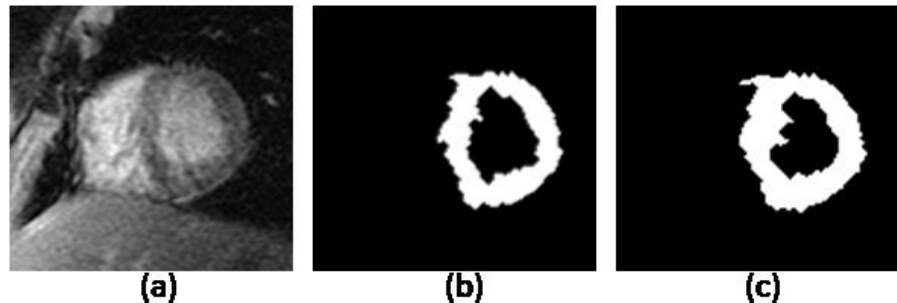


Figure 6.3 (a) Original image (b) Result of MSRG with threshold = 21, no. of sectors = 10 and Overlapping Ratio = 0.1 (c) result using threshold = 29

The problem of discontinuity which was caused by image in-homogeneity has been solved but there were some black holes that have been removed using some morphological operation.

6.1.3. Evaluation of the MSRG Coefficients

There are some parameters that affect the performance of MSRG and they are the threshold value, number of constraining sectors and overlapping ratio between sectors. To study the effect of these parameters on MSRG performance, the MSRG technique was tested with all different and possible values of no. of sectors and overlapping ratio using one hundred selected image [7] representing different qualities, SNRs and homogeneities. True positives and false positives have been computed for each result of RG and MSRG to compare between them.

The manually segmented inner and outer contours which attached with datasets are available at York University website [7]. It has been found that the mean performance of the MSRG is better than the RG in terms of TP and FP in a specific range of threshold values, as shown in figure (6.4) and it enables us to pick the best threshold values to perform well. Also the best values deduced from the figure for the overlapping percentage is 10% because it gives partially higher TP and low FP. Another study has been made on the effect of the number of sectors and the overlapping ratio on the MSRG performance.

It has been found that increasing the number of sectors improves the performance and it reaches the steady state at no. of sectors ≥ 10 as shown in figure (6.5). FP will increase if we increase the overlapping percentage and we found that the optimal overlapping ratio from figure (6.4) and (6.5) is nearly 10% and more than this percentage it begins to perform worse.

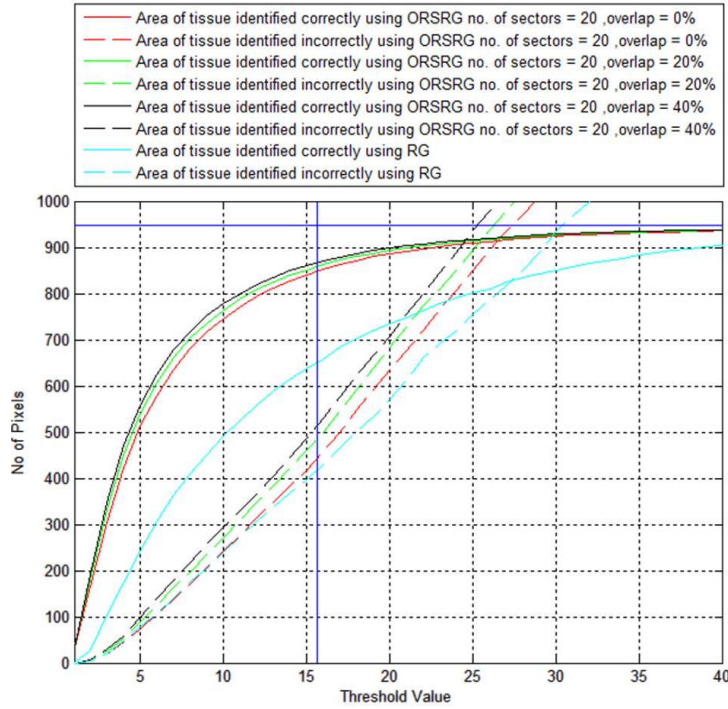


Figure 6.4 Performance curves of the RG and MSRG

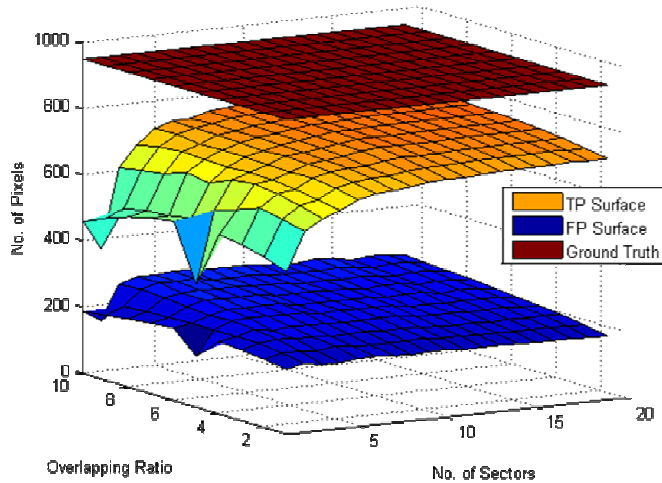


Figure 6.5 Three surfaces are representing the ground truth, TP and FP from upper to lower.

6.1.4. Resulted Contour Refinement using ACM and CPR

In this section we are going to show the results of application of some refinement methods which have been introduced in the CINE methods chapter. These methods are Active Contour Model ACM and Control Point Refinement CPR and each one of them has been used to smooth the contour and to re-position the control points into to the right place respectively. In figure (6.6.c), the effect of application of ACM and CPR is shown and it can be shown that the ACM and CPR has smoothed and re-positioned the contour into the right place.

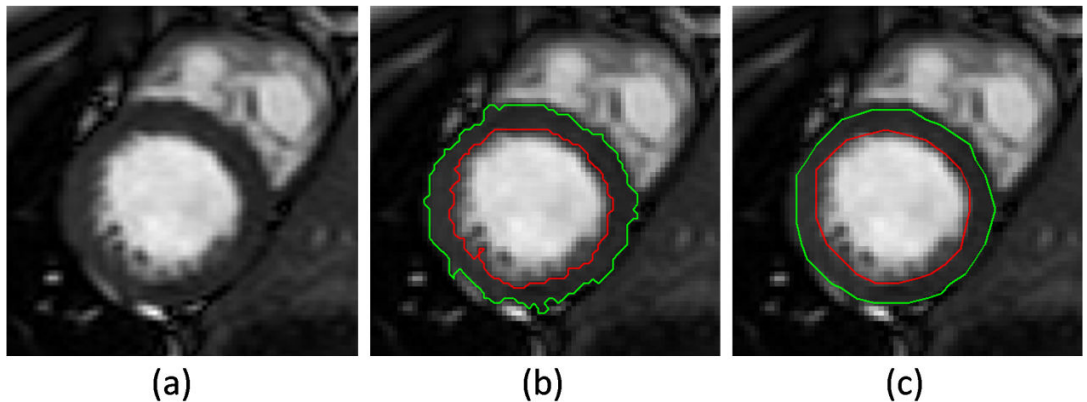


Figure 6.6 (a) Original CINE image (b) Resulted two contours are drawn in red and green representing the endocardium and epicardium (c) Refined and smoothed contours using ACM and CPR

6.1.5. Final Results

This section introduces the final results of the whole algorithm on different images with different qualities and SNRs. Figure (6.7-6.11) shows the final result of applying the proposed algorithm and these results are for 4 series representing four different qualities.

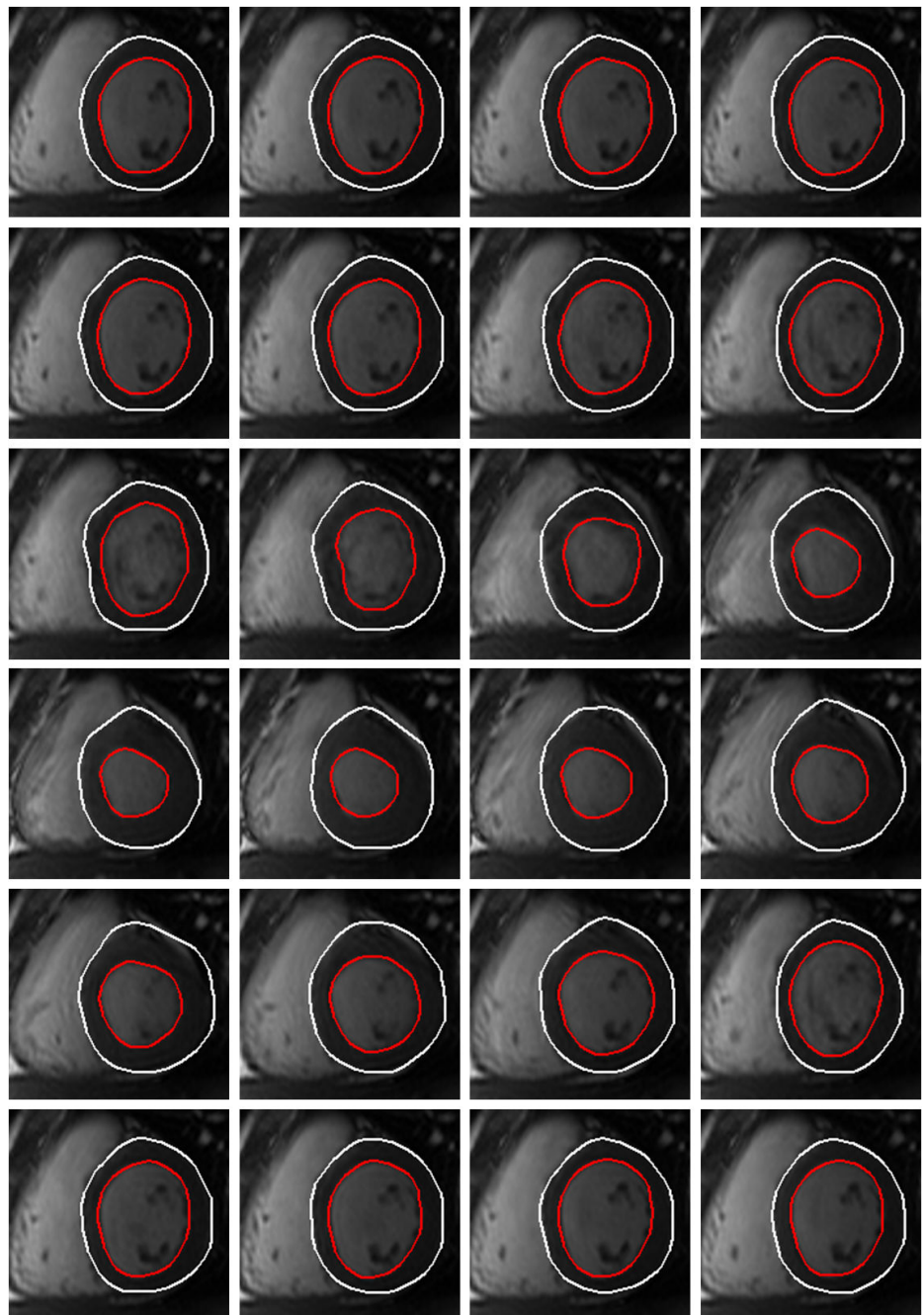


Figure 6.7 Segmentation results on 24 time frames are shown between the red and white contours which representing the endocardium and epi cardium.

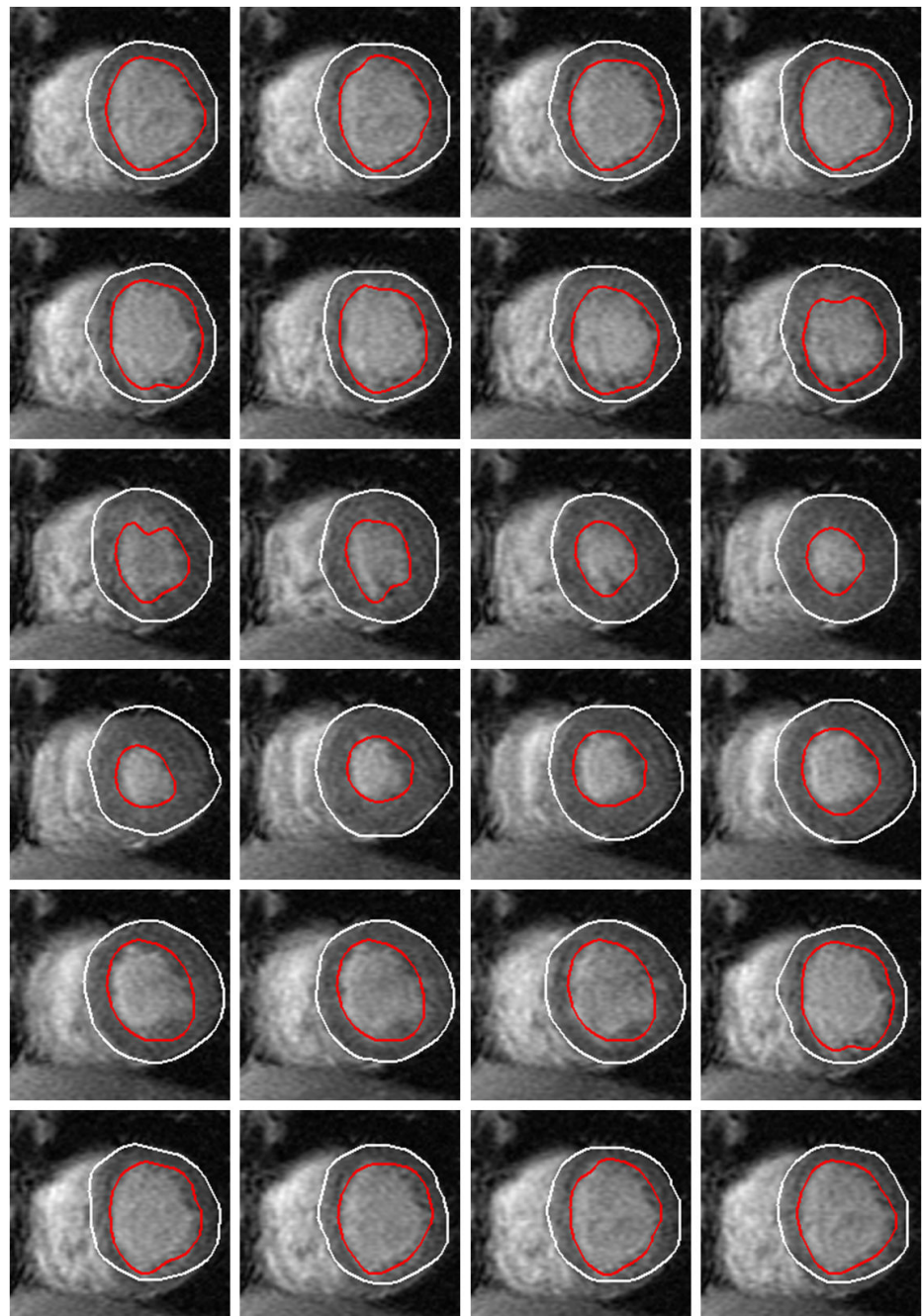


Figure 6.8 Segmentation results of low quality dataset with high in-homogeneity in these images.

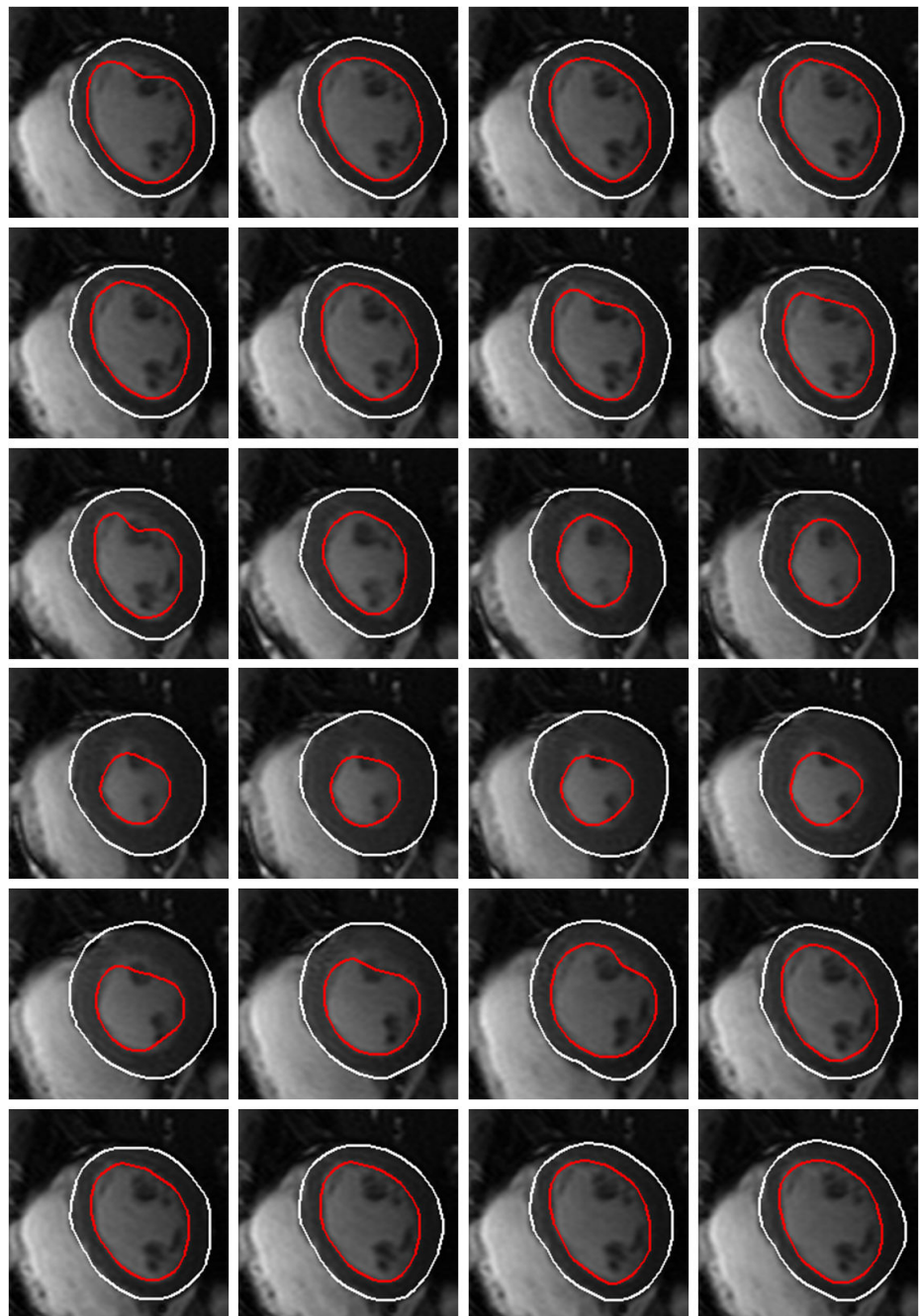


Figure 6.9 Segmentation results on 24 time frames are shown.

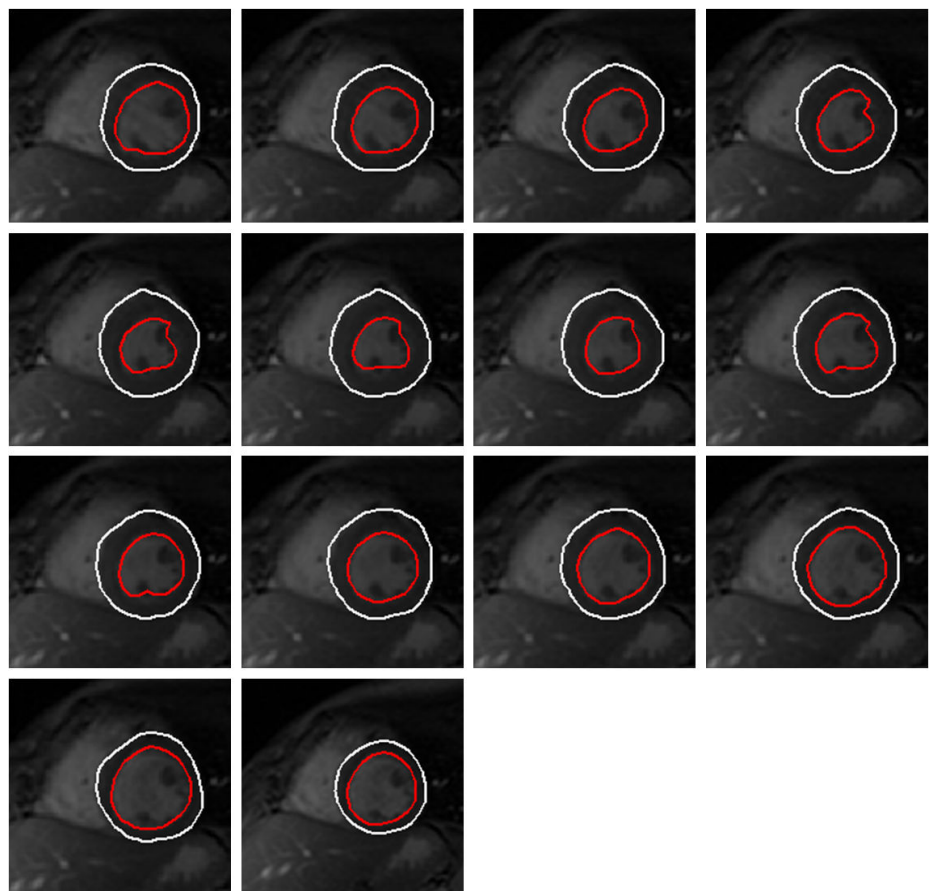


Figure 6.9 Segmentation results on 16 time frames are shown.

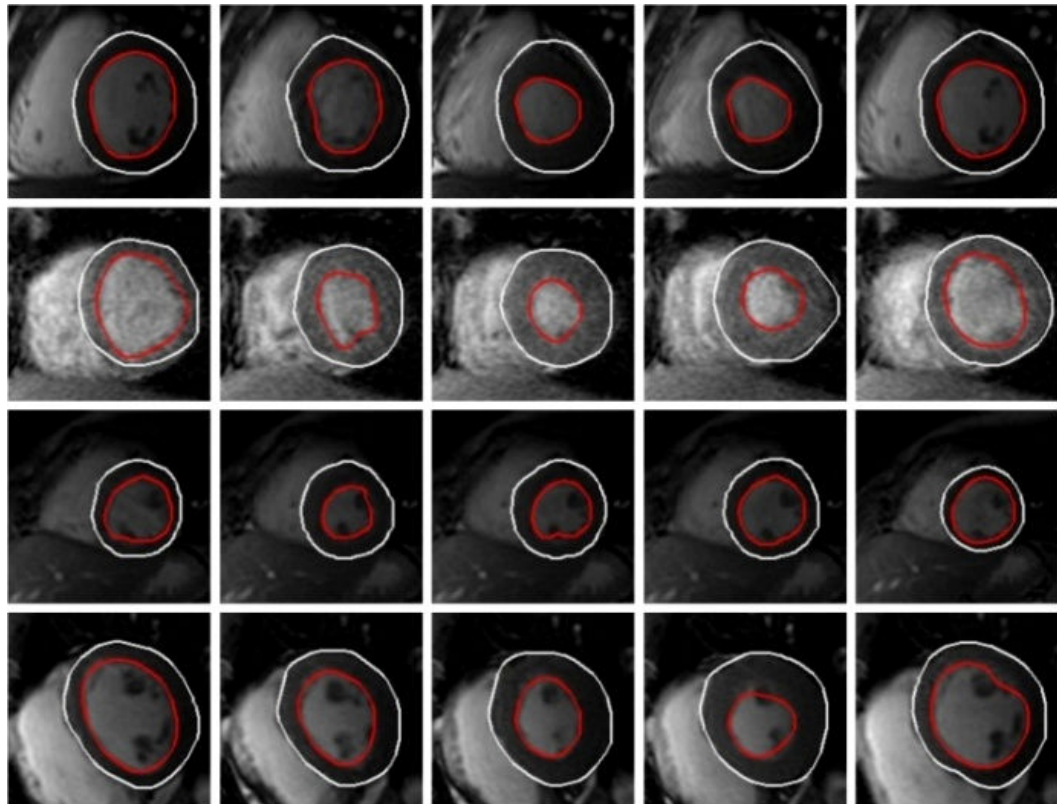


Figure 6.11 Final results of the whole algorithm are shown where the white and red contours are representing epicardium and endocardium contour.

6.2. Adaptive Multi Seeded Region Growing using K-Means (Experiment 2)

Results

In the Second experiment, results of the multi-seeded region growing will be shown and discussed in the next section. We will Show also the process of selecting the regions and their positions using k-means.

6.2.1. Selecting the sectors sizes and positions using k-means

The selection of the sectors' sizes and their positions has been done using k-means as we stated before on the methods chapter. In figure (6.12), the mid-wall contour is shown in (a) which will be used as its profile to estimate the sectors sizes and positions. And the curves after classification are shown in (b).

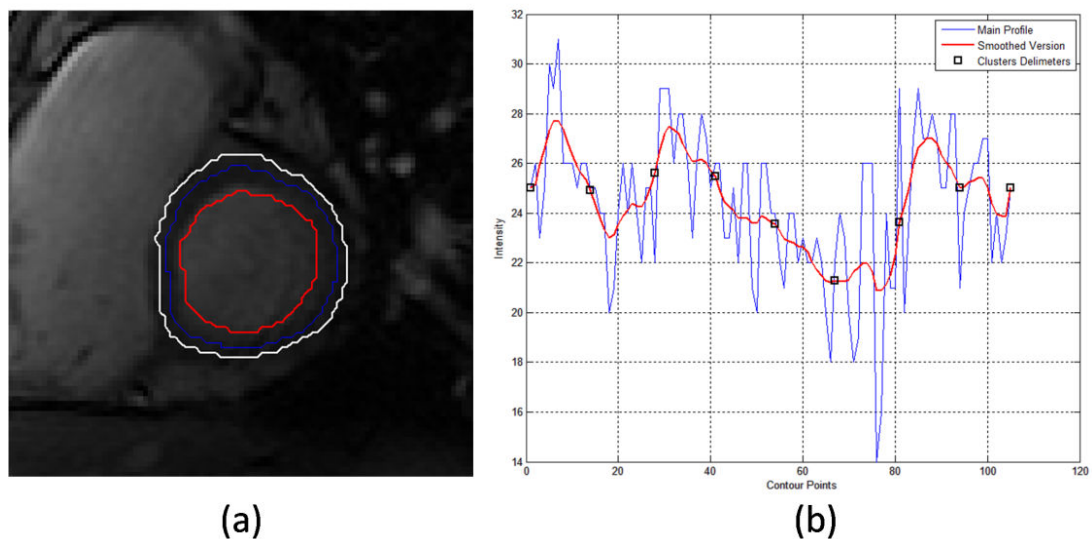


Figure 6.12 (a) short axis CINE MRI image with endocardium, mid-wall and epicardium contours drawn in red, blue and white respectively (b) graph showing the profile of the mid wall contour in blue, the smoothed version of the original profile in red and the black squares are the resulted limits of the clusters using k-means which will be transformed into the polar space to form the limiting sector.

6.2.2. Quantitative Analysis

To analyze the performance of the proposed technique, sensitivity and precision have been computed for the simple region growing, the multi seeded region growing with constant constraining areas and seed points and the MSRG with automatic selection

of constraining areas and seed points according to the intensity profile. The ground truth has been assigned using manual segmentation and this segmentation has been done by expertise which was attached with testing dataset from York University [7].

Sensitivity and precision have been computed in term of areas of tissue and background identified by the two contours (Epicontour and Endocontour).

In table 1, sensitivity and precision have been computed for the three pre-mentioned methods and we have found that the adaptive MSRG has the best performance than MSRG and RG interms of sensitivity and precision together.

Table. 1 Sensitivity and precision of each method (simple region Growing, Multi-Seeded Region Growing and Adaptive Multi-Seeded Region Growing)

	RG	MSRG	Adaptive MSRG
Sensitivity	57.11%	89.47%	89.19%
Precision	53.10%	72.34%	84.91%

6.2.3. Final Results:

The adaptive MSRG introduced good results as shown in figures (13-15) and it can be shown the ability of the technique to identify the epicardium and endocardium successfully without taking the papillary muscles in consideration and also identification of true edges between myocardium, liver and other surrounding organs.

The following figures (13-15) are the results of application of Adaptive MSRG algorithm shown in the methods section. In figure (16) some examples of the failed

cases is shown to illustrate the effect of the very weak edges and high in-homogeneity and non estimating the number of sectors exactly.

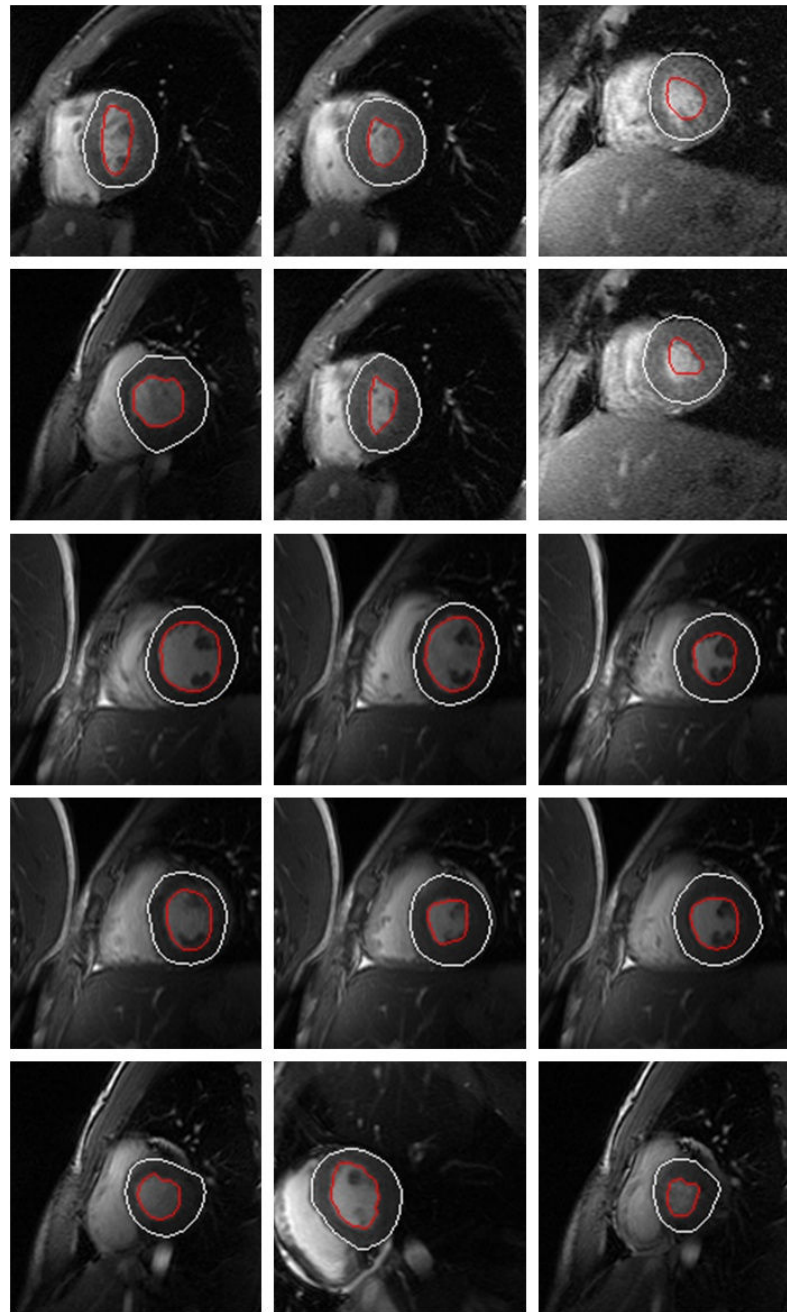


Figure 6.13 Final results of the Adaptive MSRG (Red Contours represents the endocardium and White Contours represents the epicardium).

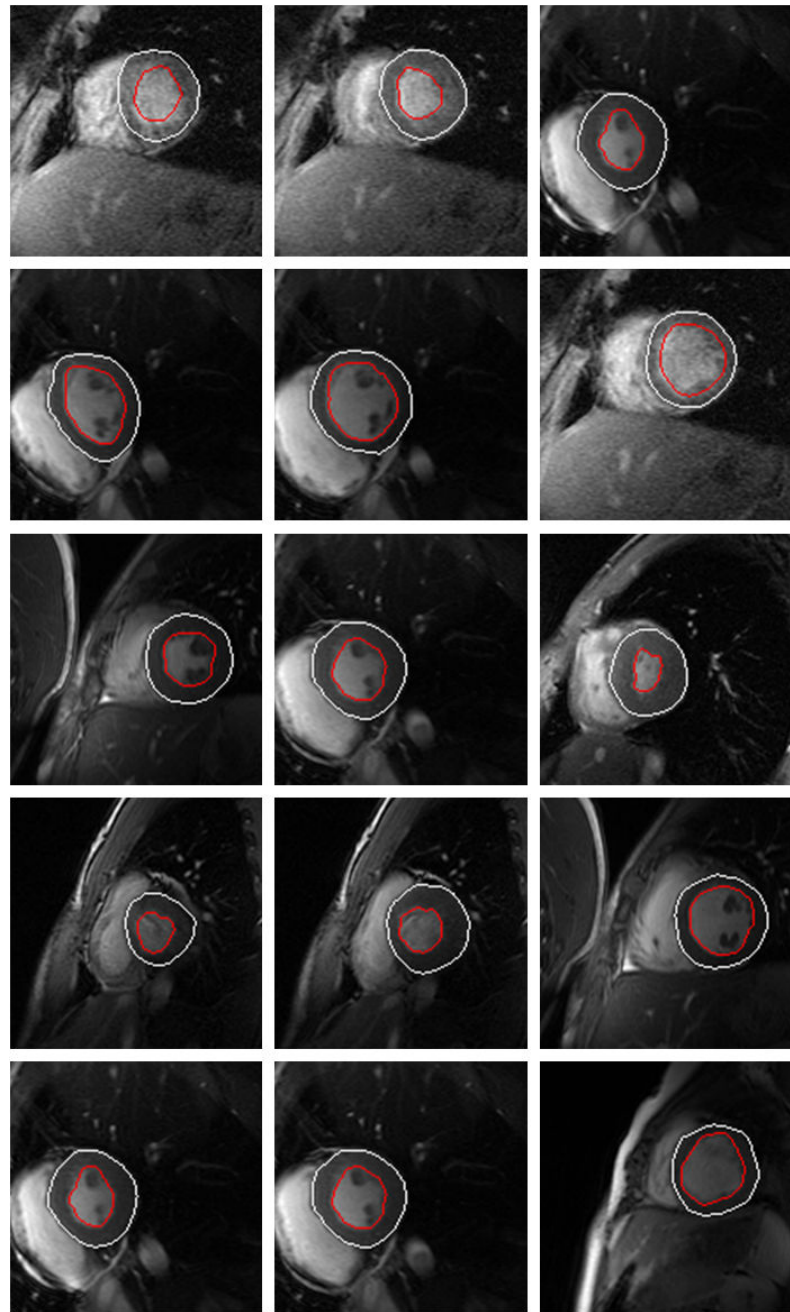


Figure 6.14 Final results of the Adaptive MSRG (Red Contours represents the endocardium and White Contours represents the epicardium).

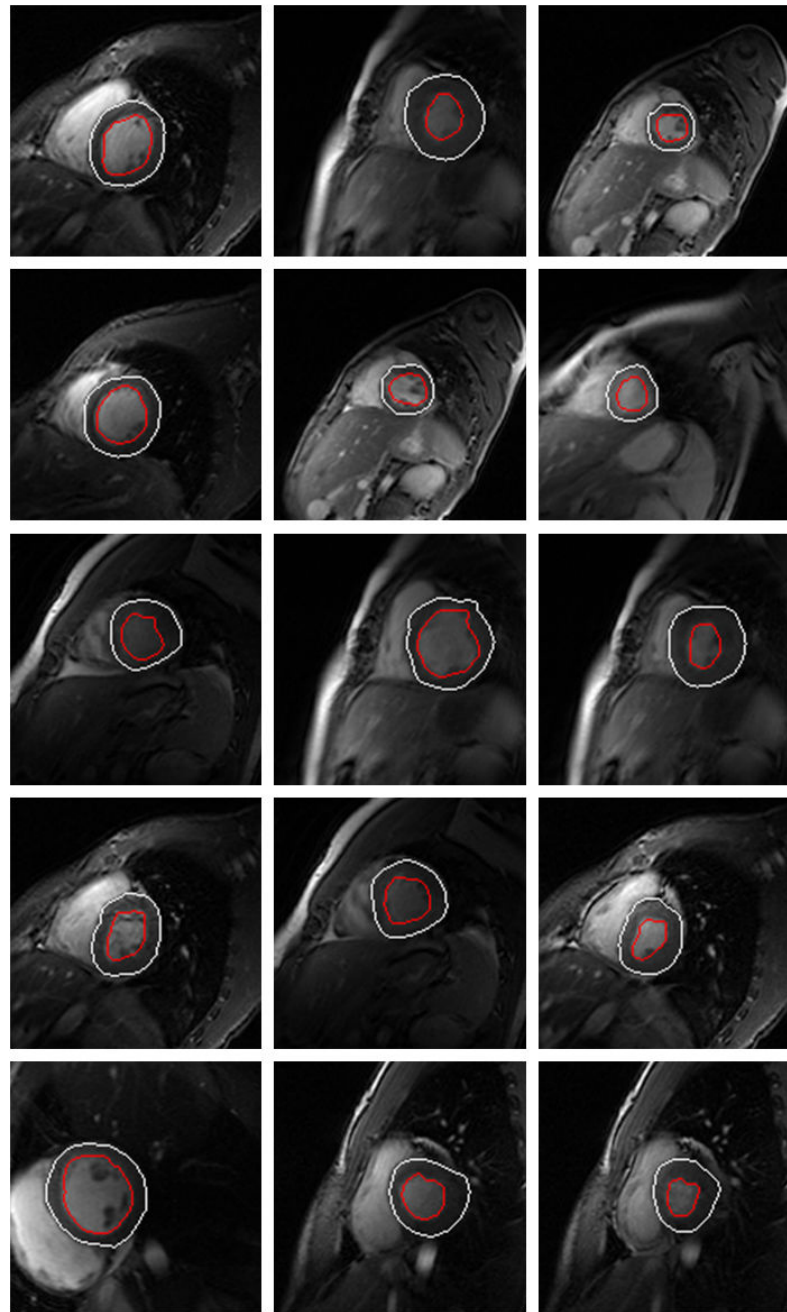


Figure 6.15 Final results of the Adaptive MSRG (Red Contours represents the endocardium and White Contours represents the epicardium).

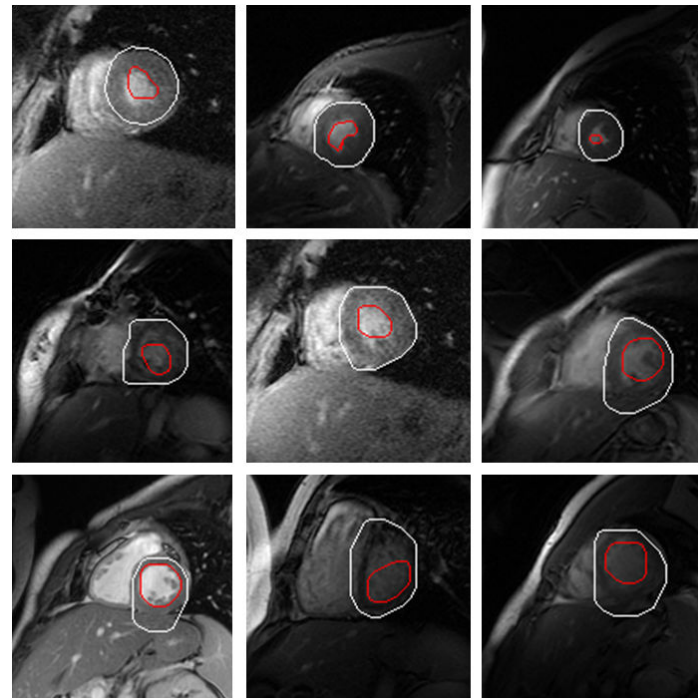


Figure 6.16 Some of the failed segmented frames.

BB CLASSIFICATION RESULTS & DISCUSSION

7.1. Simulated Data Results

For each two vectors of background & tissue which generated with using different values of σ and $\delta\omega$ over the predefined range was tested by application of the proposed method to classify each generated vector \bar{v} either as background or tissue based on equations (5.10) and (5.11). The vectors are classified also using Linear, Quadratic and Rectangular techniques based on formulas in equations (5.16), (5.18) and (5.19). All the samples that were identified as background were excluded and the joint probability density function of S_1 versus S_2 for the remaining samples was recalculated. Figure (7.1.c), (7.1.d) shows the resulting joint probability density functions using Bayesian classifier. Figure (7.1.e), (7.1.f) shows the resulting joint probability density functions using Quadratic classifier. Figure (7.1.g), (7.1.h) shows the resulting joint probability density functions using Rectangular classifier. Figure (7.1.i), (7.1.j) shows the resulting joint probability density functions using linear classifier. Evidently from the figure, it can be shown that the methods ware successful in suppressing most of the background signal. Also it shows that some background samples still exist while some tissue signal intensities were mistakenly suppressed. Nevertheless, this type of errors is natural in any classification process (usually referred to as type-I and type-II errors). It is shown that by increasing σ value during generation of the two vectors that type-II error increase and type-I error still fixed. The Bayesian classification keeps these errors at their minimal value. It is worth noting that the edges of the suppressed areas in figures (7.1.c) and (7.1.d) represents

the Bayesian decision boundary given by setting Eq. (5.10) to zero and solving for S_1 and S_2 .

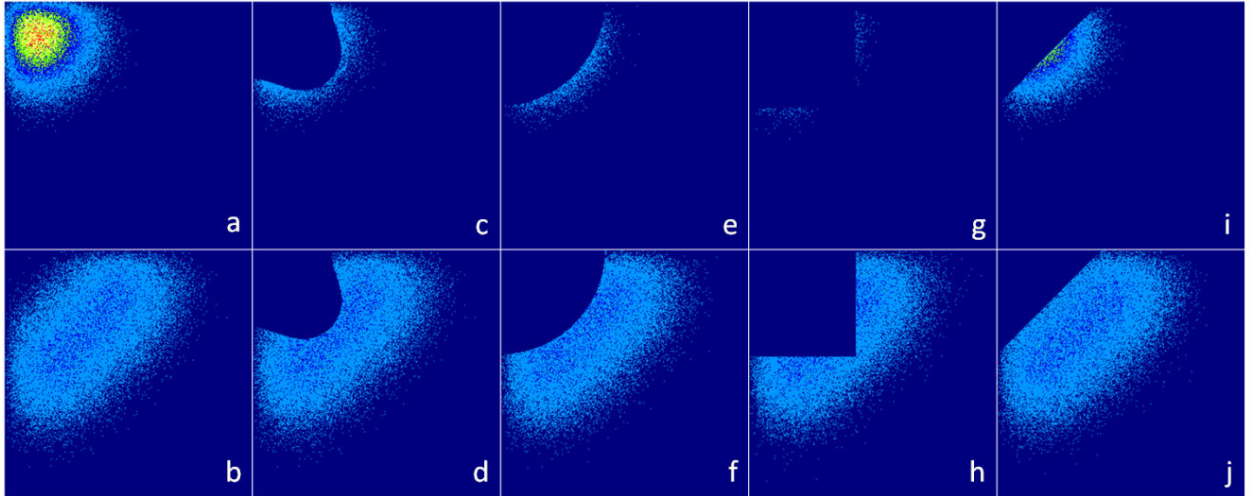


Figure 7.1 The Joint PDF of signal intensities S_1 and S_2 for: (a) the background and (b) tissue samples. (c) and (d) are the Joint PDF of signal intensities S_1 and S_2 after removing the samples that are identified as background using *Bayes Classifier* for background and tissue signals. (e) and (f) are like (c, d) but identified using *Quadratic Classifier*, (g) and (h) are like (c, d) but identified using *Rectangular Classifier*. Also (i) and (j) are like (c, d) and for *Linear classifier*. All signals are generated with $\sigma = 70$.

For each two sets of vectors \bar{v} generated from different values of σ , $\partial\omega$; sensitivity, specificity and precision were computed. For each of Bayesian, Linear, Quadratic and Rectangular Classifiers' results Sensitivity, Specificity and Precision were computed to show the difference between all the used classifiers. Figure (7.2) shows the Sensitivity value for each classifier where the vertical axis represents sensitivity and

the horizontal axis represents the noise standard deviation. Figure (7.3) shows the Specificity value for each classifier where the vertical axis represents specificity and the horizontal axis represents the noise standard deviation. Figure (7.4) shows the Precision value for each classifier where the vertical axis represents precision and the horizontal axis represents the noise standard deviation. The computation time required for each method has been calculated and displayed in Table (7.1).

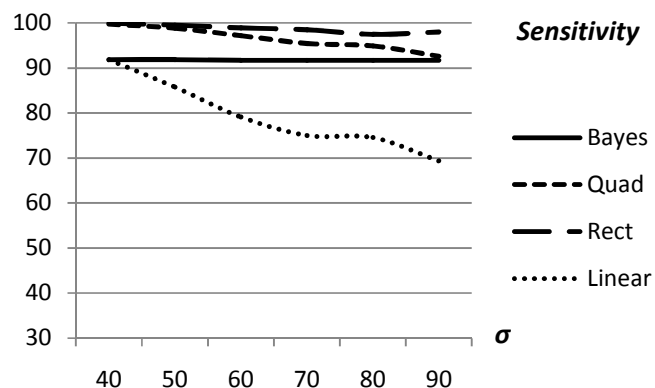


Figure 7.2 The Sensitivity (Ability of detecting Background) signals using the four methods for generated signals with different σ .

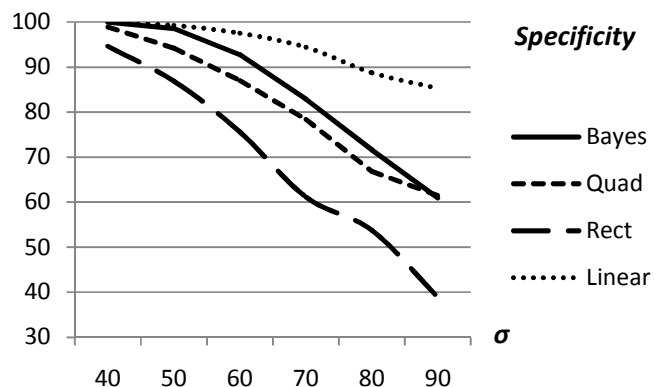


Figure 7.3 The Specificity (Ability of detecting Tissue) signals using the four methods for generated signals with different σ .

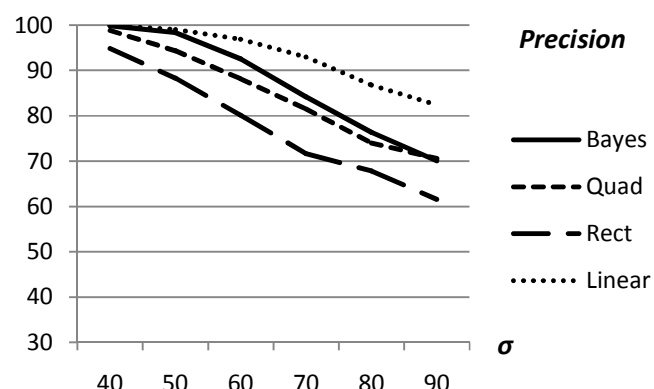


Figure 7.4 Precision using the four methods for generated signals with different σ .

Table 7.1 Relative Computation Time for each technique.

Classifier Type	Relative Computation Time
Bayesian Classifier	2.387
Quadratic Classifier	1.085
Rectangular Classifier	1.000
Linear Classifier	1.034

7.2. Real Images Results

Figure (7.6.a) shows the results after truncating the background noise using Bayes Classifier on two different images which are shown in figure (7.5). Figures (7.6.b), (7.6.c), (7.6.d) and (7.6.e) show the result of applying L^1 Norm, L^2 Norm and L^∞ Norm and Global threshold techniques on the images of figure (7.5). It is worth noting that all images in figure (7.5) are displayed with the same contrast and intensity settings. That is, the differences between the images are due to the effect of the noise removal process.

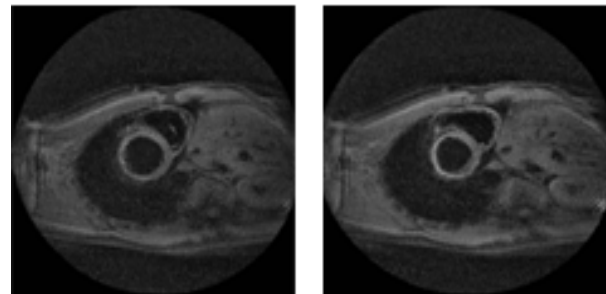


Figure 7.5 Two combined Images that were chosen to apply the different techniques on them.

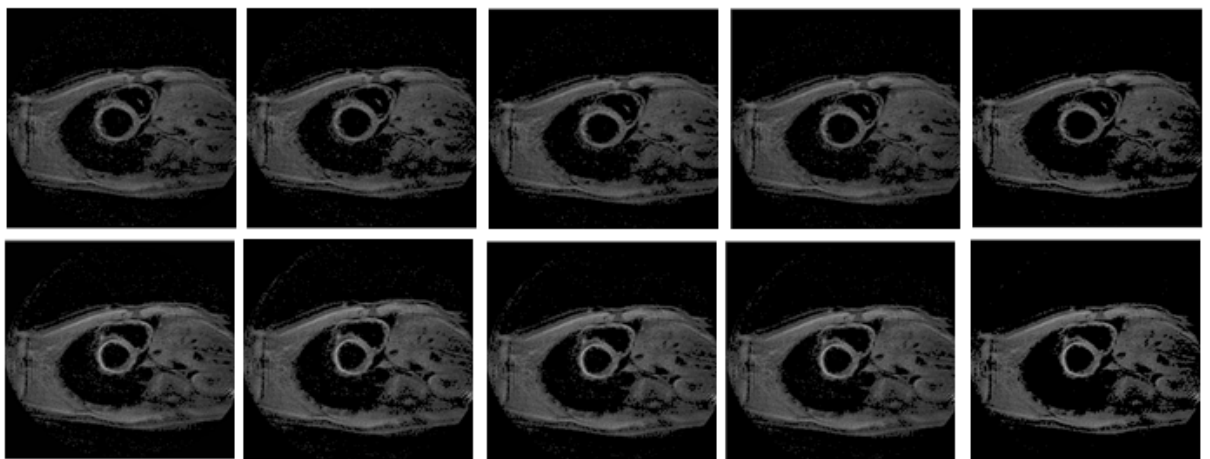


Figure 7.6 (a) shows the result of applying Bayesian technique, (b) shows the result of applying L_1 technique (c) shows the result of applying L_2 technique (d) shows the result of applying L_∞ technique (e) shows the result of applying Global Threshold technique.

Numerical Analysis was done to represent how each technique behaves in different ROI (background, static tissue and myocardium) for the different time frames, and therefore we can decide the sensitivity and specificity for each technique. As shown in figure (7.7) three regions were chosen and they are represented by dotted, dashed and solid line regions. And for each region the number of pixels considered to be background in each technique is calculated. Figure (7.8), (7.9) and (7.10) shows the number of pixels considered as a background in each technique for all the time frames, also Sensitivity and specificity for all the techniques are calculated, where they are mentioned before. Figure (7.11), (7.12) shows the sensitivity and Specificity behavior with the time for the all techniques.

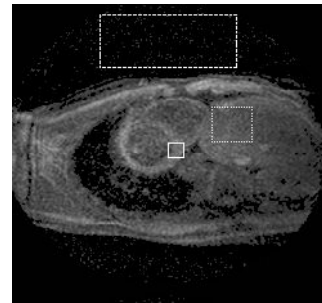


Figure 7.7 The different ROIs, background region (Dotted) static tissue (Dashed), and myocardium region (Solid).

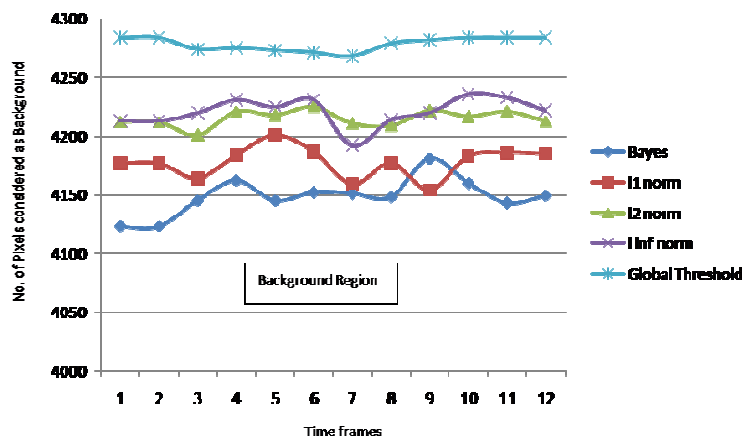


Figure 7.8 Shows the number of pixels considered as noise in the background region.

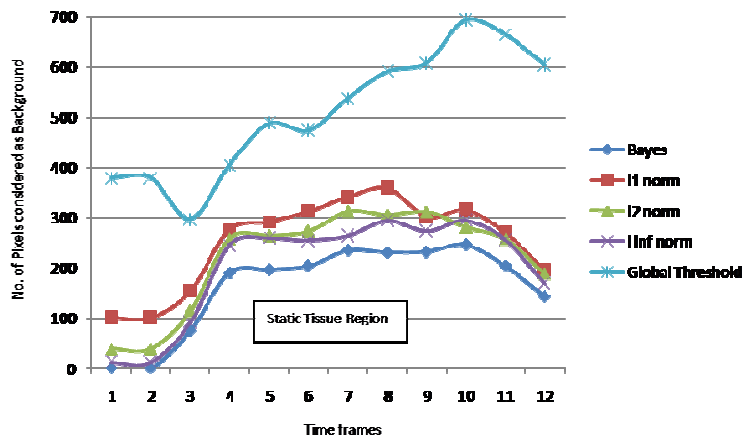


Figure 7.9 Shows the number of pixels considered as noise in the background region.

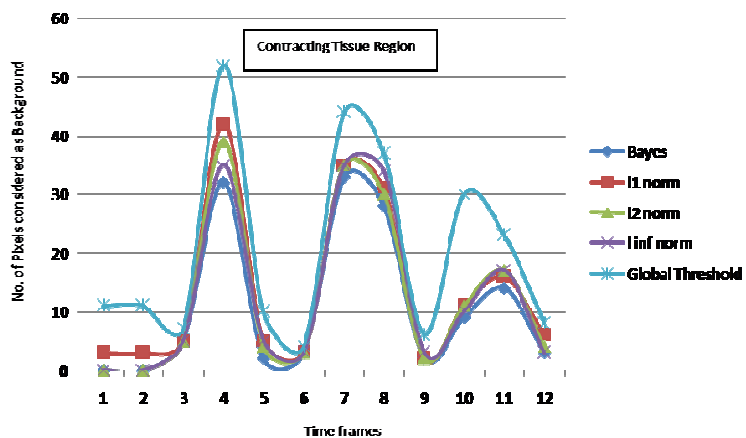


Figure 7.10 Shows the number of pixels considered as noise in the background region.

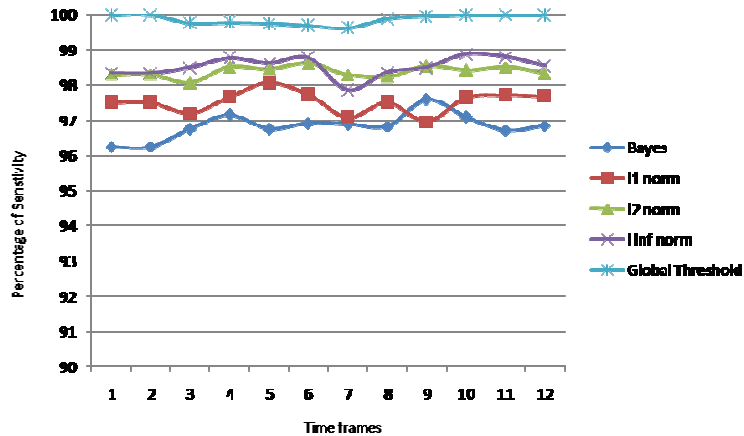


Figure 7.11 Shows the sensitivity behavior for each technique within the time frames.

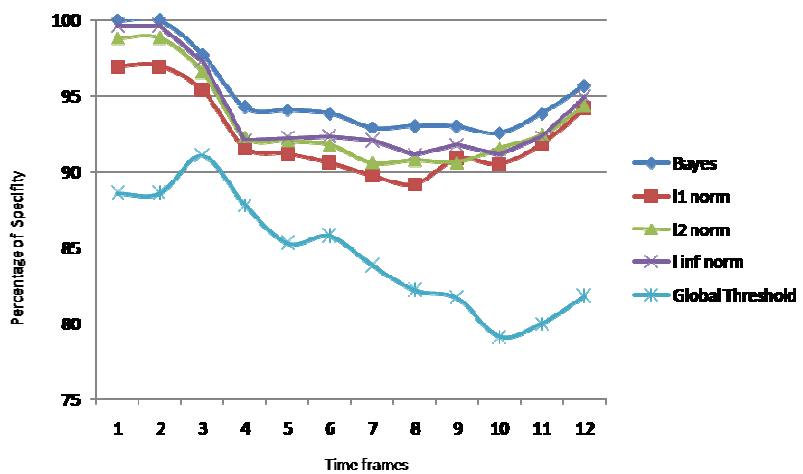


Figure 7.12 Shows the sensitivity behavior for each technique within the time frames.

However quantitative analysis is done, but there is a need to measure also the efficiency based on computational time, through applying the 5 different methods stated in this paper, each method differ from the other in the time needed to perform the algorithm to a set of images. The computer specification that was used was 2.66GHz Ccore2Duo processor with 2 GB RAM, the technique that need the most computational time was Bayesian technique while that need the least time is Global

threshold technique. Numerically each technique was applied on 12 pictures, for the Bayesian method it took 8.287 seconds to apply the method for all the time frames, while for L^2 Norm method it took 2.228 seconds, for the L^1 Norm method it took 2.317 seconds, for the L^∞ Norm method it took 2.121 seconds, finally the Global threshold method it took 1.64 seconds. Computational time could be reduced when advanced programming techniques are used.

Table 7.2 Relative Computation

Method	Computation Time(sec)	Relative Time
Global Threshold	0.1366	1
l_∞ norm	0.1761	1.28
l_1 norm	0.1780	1.303
l_2 norm	0.1856	1.35
Bayesian	0.6702	4.90

The results of the Bayesian method have been enhanced by the application of some morphological operators as we stated in the further processing section in the methods chapter. In figure (7.13) it can be shown that the result became more enhanced and more realistic after the further enhancement.

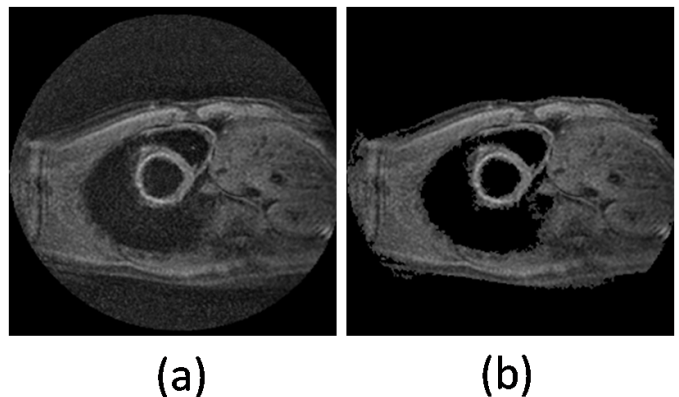


Figure 7.13 (a) Original Black Blood MRI Image. (b) Final Result after application of the further processing and enhancement methods.

CONCLUSION

Cardiac MRI generally has better resolution and contrast than other imaging modalities such as ultrasound. Besides that, they have the ability to provide valuable clinical information such as cardiac structure and regional function measurements better than CT Imaging. However, they suffer from the low resolution and long exam time taken to the test. There are also some limitations in widespread use of MRI in clinical applications, the most important of all being the fact that during each cardiac MRI acquisition, more than 100 static 2D scans are generated.

In order to evaluate the cardiac function, we are in need to measure some parameters such as ejection fraction. To do that LV has to be segmented in each of the slices and time frames. Manual segmentation of the LV is very labor intensive and it is considered to be the bottleneck of the MRI process. So that, any application that facilitates semi- or fully automatic segmentation of CMR images will be beneficial to the medical imaging community.

There is another problem concerning the black blood images which suffer from low signal to noise SNR ratio. So there was a simple solution to increase this ratio and this is done by nulling of the background noise. In order to null the background we are in need to identify or classify the background from the tissue.

In this work, we have proposed an algorithm to segment and track the left ventricle in a set of cine MRI, consisting of multiple slices of heart from the apex to the base, each in 18-25 phases. Also we have proposed the usage of the Bayesian classifier to identify the tissue and background in the black blood Cardiac MRI.

The focus of our work is to track the LV in a 2D+T data set, consisting of consecutive time frames of a single slice. Some of the challenges of working with MR images include:

- low-contrast in some areas of epicardium adjacent to the lungs and fatty tissue
- Quality degradation by artifacts due to blood flow or respiratory motion
- Papillary muscles which are located close to the LV and have similar intensity as the myocardium

Due to these challenges, it is hard to derive estimates based on gradient information alone. We have taken a new approach to this problem, use the resulted region from the multi seeded region growing technique as an input for the ACM and CPR to add the spatial information to our solution and guarantee the speed of the algorithm. We have two experiments the first one includes all the previous steps and this experiment has some problems like the unknown technique coefficients. So we have proposed another approach and in this approach we have used the k-means to estimate the sectors sizes and positions which included in the second experiment. Beside that ACM has been used as a smoothing technique to add some spatial information to our resulted contour.

In this thesis we have also proposed the usage of the Bayesian classifier to classify the tissue and background and have evaluated its performance in comparison with the basic classifiers which have been stated before in the methods chapter.

Performance of the MSRG and adaptive MSRG algorithms depends on a lot of factors, including the number of sectors used, more importantly the number of

iterations and the coefficients of the cost functions of ACM and the degree of the smoothness of the profile for the adaptive MSRG.

MSRG has been experimented with different set of parameters and presented the effects of varying such parameters in the results chapter. Generally, most of these parameters were found intuitively or experimentally. We also tested different methods or enhancements at various stages of our two problems. And we have got good results visually and quantitatively for the both problems.

8.1. Future Work

We discussed some of the advantages and disadvantages of our solution in the previous section. There are a lot of ideas that can be added to our current framework based on its importance and complexity. In the future, we are going to try estimating the suitable number of sectors to fully automate this process and also try to estimate the initial endocardium and epicardium for the first frame automatically. This thesis can be extended to analyze the 4D data in the same time, including the previous and past slices available for the refinement step as well. To make all contour results affect each other.

REFERENCES

- [1] American Heart Association. *Heart disease and stroke statistics - 2006 update*. online, September 2006.
<http://circ.ahajournals.org/cgi/content/short/113/6/e85>.
- [2] Annual Statistical Report. Minsitry of Health, Egypt. <http://www.mohp.gov.eg/>
- [3] J. Earls, V. Ho, T. Foo, E. Castillo, and S. Flamm. *Cardiac MRI: Recent progress and continued challenges*. *Journal of Magnetic Resonance Imaging*, 16:111{127, 2002.
- [4] A.F. Frangi, D. Rueckert, and J.S. Duncan. *Three-dimensional cardiovascular image analysis*. *IEEE Transactions on Medical Imaging*, 21(9):1005{1010, 2002
- [5] H. Azhari, S. Sideman, J. L. Weiss, E. P. Shapiro, M. L. Weisfeldt, W. L. Graves, W. J. Rogers, R. Beyar, "Three dimensional mapping of acute ischemic regions using MRI: wall thickening versus motion analysis" *AJP - Heart and Circulatory Physiology* 1990.
- [6] Ahmed S. Fahmy, Li Pan, Nael F. Osman , *Artifact-free black-blood cine cardiac imaging in a single breath-hold*, *Magn Resonance Imaging Journal Volume 24, Issue 10, Pages 1303-1310, 2006*
- [7] Aletras AH, Wen H. *Mixed echo train acquisition displacement encoding with stimulated echoes: an optimized DENSE method for in vivo functional imaging of the human heart*. *Magn Reson Med* 2001; 46:523–534.
- [8] Frahm J, Hanicke W, Bruhn H, Gygell ML, Merboldt KD. *High-speed STEAM of the human heart*. *Magn Reson Med* 1991; 22: 133-142.
- [9] Fischer SE, Stuber M, Scheidegger MB, Boesiger P. *Limitations of Stimulated Echo Acquisition Mode (STEAM) Techniques in Cardiac applications*. *Magn Reson Med* 1995; 34: 80-91.
- [10] Fahmy AS, Stuber M, Osman NF. *Correction of throughplane deformation artifacts in Stimulated Echo Acquisition Mode (STEAM) cardiac imaging*. *Magn Reson Med* 2006; 55 (2): 404-412.
- [11] J. Rogers. *Cardiovascular physiology*. Online, 1999.
http://www.nda.ox.ac.uk/wfsa/html/u10/u1002_01.htm.
- [12] W.J. Germann and C.L. Staneld. *Principles of Human Physiology*. Benjamin/Cummings, 2004.
- [13] J. Earls, V. Ho, T. Foo, E. Castillo, and S. Flamm. *Cardiac MRI: Recent progress and continued challenges*. *Journal of Magnetic Resonance Imaging*, 16:111{127, 2002.
- [14] A.F. Frangi, D. Rueckert, and J.S. Duncan. *Three-dimensional cardiovascular image analysis*. *IEEE Transactions on Medical Imaging*, 21(9):1005{1010, 2002}.
- [15] K.M. Das. *Cardiac MR: One-stop shop*. *HEART VIEWS*, 5(1):17{23, 2004}.

- [16] Lauterbur PC (1973). "Image Formation by Induced Local Interactions: Examples of Employing Nuclear Magnetic Resonance". *Nature* 242: 190–191. doi:10.1038/242190a0.
- [17] The Economist. Medical imaging - MRI's inside story. *The Economist Technology Quarterly*, 369(8353):24{26, Dec. 4th 2003.
- [18] a b c Filler AG (2009). "The history, development, and impact of computed imaging in neurological diagnosis and neurosurgery: CT, MRI, DTI". *Nature Precedings*.doi:10.1038/npre.2009.3267.5.
- [19] Lauterbur PC (1974). "Magnetic resonance zeugmatography". *Pure and Applied Chemistry* 40: 149–157. doi:10.1351/pac197440010149.
- [20] Damadian R, Goldsmith M, Minkoff L (1977). "NMR in cancer: XVI. Fonar image of the live human body". *Physiological Chemistry and Physics* 9: 97–100.
- [21] Hinshaw DS, Bottomley PA, Holland GN (1977). "Radiographic thin-section image of the human wrist by nuclear magnetic resonance". *Nature* 270: 722–723. doi:10.1038/270722a0.
- [22] William R. Hendee, E. Russell Ritenour "Medical Imaging Physics (Fourth Edition)" Published Online: 20 Mar 2003.
- [23] D. A. Skoog, F. J. Holler, and T. A. Nieman, editors. *Principles of Instrumental Analysis*. Harcourt Brace College Publishers, 1998, fifth edidtion.
- [24] K.M. Das. Cardiac MR: One-stop shop. *HEART VIEWS*, 5(1):17-23, 2004.
- [25] A.F. Frangi, D. Rueckert, and J.S. Duncan. Three-dimensional cardiovascular image analysis. *IEEE Transactions on Medical Imaging*, 21(9):1005-1010, 2002.
- [26] N. F. Osman , S. Sampath , E. Atalar , J. L. Prince "Imaging longitudinal cardiac strain on short-axis images using strain-encoded MRI". *Magnetic Resonance in Medicine* 46 (2002).
- [27] L. P. Clarke, R. P. Velthuizen, M. A. Camacho, J. J. Heine, M. Vaidyanathan, L. O. Hall, R. W. Thatcher, and M. L. Silbiger, "MRI segmentation: Methods and applications," *Magn. Reson. Imag.*, vol. 13, no. 3, pp. 343–368, 1995.
- [28] J.S. Suri, "Computer vision pattern recognition and image processing in left ventricle segmentation: The last 50 years," *Pattern Anal. Appl.*, vol. 3, pp. 209–242, 2000.
- [29] A. E. O. Boudraa, M. Arzi, J. Sau, J. Champier, S. Hadj-Moussa, J.-E. Besson, D. Sappey-Marinier, R. Itti, and J.-J. Mallet, "Automated detection of the left ventricular region in gated nuclear cardiac imaging," *IEEE Trans. Biomed. Eng.*, vol. 43, no. 4, pp. 430–437, Apr. 1996.
- [30] A. E. O. Boudraa, "Automated detection of the left ventricular region in magnetic resonance images by Fuzzy C-Means model," *Int. J. Card. Imag.*, vol. 13, no. 4, pp. 347–355, 1997.
- [31] G. D.Waiter, F. I.McKiddie, T.W. Redpath, S. I. Semple, and R. J. Trent, "Determination of normal regional left ventricular function from cine-MR images using a semi-automated edge detection method," *Magn. Reson. Imag.*, vol. 17, pp. 99–107, 1999.
- [32] A. S. Pednekar, R. Muthupillai, V. V. Lenge, I. A. Kakadiaris, and S. D. Flamm, "Automatic identification of the left ventricle in cardiac cine-MR images:

- Dual-contrast cluster analysis and scout-geometry approaches,"* *J. Magn. Reson. Imag.*, vol. 23, no. 5, pp. 641–651, 2006.
- [33] M. Lynch, O. Ghita, and P. F. Whelan, “Left-ventricle myocardium segmentation using a coupled level-set with a priori knowledge,” *Comput. Med. Imag. Graph.*, vol. 30, pp. 255–262, 2006.
- [34] Z. Zhou, J. You, P. A. Heng, and D. Xia, “CardiacMRimage segmentation and left ventricle surface reconstruction based on level set method,” *Stud. Health Technol. Sci.*, vol. 111, pp. 629–632, 2005.
- [35] Sahoo PK, Soltani S, Wong AKC. 1988. *A survey of thresholding techniques*. *Comput. Vis. Graph. Image Proc.* 41:233–60
- [36] Singleton HR, Pohost GM. 1997. Automatic cardiac MR image segmentation using edge detection by tissue classification in pixel neighborhoods. *Magn. Reson. Med.* 37:418–24
- [37] Gordon CL, Webber CE, Adachi JD, Christoforou N. 1996. In vivo assessment of trabecular bone structure at the distal radius from high-resolution computed tomography images. *Phys. Med. Biol.* 41: 495–508
- [38] Li HD, Kallergi M, Clarke LP, Jain VK, Clark RA. 1995. Markov random field for tumor detection in digital mammography. *IEEE Trans. Med. Imaging* 14:565–76
- [39] Lee C, Hun S, Ketter TA, Unser M. 1998. Unsupervised connectivity-based thresholding segmentation of midsagittal brain MR images. *Comput. Biol. Med.* 28:309–38
- [40] Haralick RM, Shapiro LG. 1985. Image segmentation techniques. *Comput. Vis. Graph. Image Proc.* 29:100–32
- [41] Gibbs P, Buckley DL, Blackband SJ, Horsman A. 1996. Tumour volume detection from MR images by morphological segmentation. *Phys. Med. Biol.* 41:2437–46
- [42] Pohlman S, Powell KA, Obuchowski NA, Chilcote WA, Broniatowski SG. 1996. Quantitative classification of breast tumors in digitized mammograms. *Med. Phys.* 23:1337–45
- [43] Manouskas IN, Undrill PE, Cameron GG, Redpath TW. 1998. Split-and-merge segmentation of magnetic resonance medical images: performance evaluation and extension to three dimensions. *Comput. Biomed. Res.* 31:393–412
- [44] Wells WM, Grimson WEL, Kikins R, Jolesz FA. 1996. Adaptive segmentation of MRI data. *IEEE Trans. Med. Imaging* 15:429–42
- [45] Bezdek JC, Hall LO, Clarke LP. 1993. Review of MR image segmentation techniques using pattern recognition. *Med. Phys.* 20:1033–48
- [46] Lei T, Sewchand W. 1992. Statistical approach to X-ray CT imaging and its applications in image analysis. II. A new stochastic model-based image segmentation technique for X-ray CT image. *IEEE Trans. Med. Imaging* 11(1):62–69
- [47] Jain AK, Dubes RC. 1988. *Algorithms for Clustering Data*. Englewood Cliffs, NJ: Prentice Hall. 696 pp.

- [48] M. Lynch, O. Ghita P. F. Whelan, *Automatic Segmentation of the Left Ventricle Cavity and Myocardium in MRI Data.*
- [49] Zadeh LA. 1965. *Fuzzy sets. Inf. Control* 8:338–53
- [50] R. J. Van Der Geest, V. G. M. Buller, E. Jansen, H. J. Lamb, L. H. B. Baur, E. E. Van Der Wall, A. de Roos, and J. H. C. Reider, “Comparison between manual and semiautomated analysis of left ventricle volume parameters from short-axis MR images,” *J. Comput. Assisted Tomogr.*, vol. 21, no. 5, pp. 756–765, 1997.
- [51] R. J. vanGeuns, T. Baks, E. H. Gronenschield, J. P. Aben, P. A. Wielopolski, F. Cademartiri, and P. J. de Feyter, “Automatic quantitative left ventricular analysis of cine MR images by using three-dimensional information for contour detection,” *Radiology*, vol. 240, no. 1, pp. 215–221, 2006.
- [52] A. Pednekar, U. Kurkure, R. Muthupillari, S. Flamm, and I. A. Kakadiaris, “Automated left ventricle segmentation in Cardiac MRI,” *IEEE Trans. Biomed. Eng.*, vol. 53, no. 7, pp. 1425–1428, Jul. 2006.
- [53] M. F. Santarelli, V. Positano, C. Michelassi, M. Lombardi, and L. Landini, “Automated cardiac MR image segmentation: Theory and measurement evaluation,” *Med. Eng. Phys.*, vol. 25, no. 2, pp. 149–159, 2003.
- [54] M. R. Kaus, J. von Berg, J. Weese, W. Niessen, and V. Pekar, “Automated segmentation of the left ventricle in cardiac MRI,” *Med. Image Anal.*, vol. 8, no. 3, pp. 245–254, 2004.
- [55] M.-P. Jolly, “Automatic segmentation of the left ventricle in cardiac MR and CT Images,” *Int. J. Comput. Vis.*, vol. 70, no. 2, pp. 151–163, 2006.
- [56] D. L. Pham, C. Xu, J. L. Prince, *A Survey of Current Methods in Medical Image Segmentation*, in *Annual Review of Biomedical Engineering*, Vol. 2 (2000), pp. 315–338.
- [57] R. J. Van Der Geest, B. P. Lelieveldt, E. Angelie, M. Danilouchkine, C. Swingen, M. Sonka, and J. H. Reiber, “Evaluation of a new method for automated detection of left ventricular boundaries in time series of magnetic resonance images using an active appearance motion model,” *J. Cardiovasc. Magn. Reson.*, vol. 6, no. 3, pp. 609–617, 2004.
- [58] Q. Chen, Z.M. Zhou, M. Tang, P. A. Heng, and D. S. Xia, “Shape statistics variational approach for the outer contour segmentation of left ventricle MR Images,” *IEEE Trans. Inf. Technol. Biomed.*, vol. 10, no. 3, pp. 588–597, Jul. 2006.
- [59] W. J. Niessen, B. M. T. H. Romeny, and M. A. Viergever, “Geodesic deformable models for medical image analysis,” *IEEE Trans. Med. Imag.*, vol. 17, no. 4, pp. 634–641, Aug. 1998.
- [60] N. Paragios, “A level set approach for shape-driven segmentation and tracking of the left ventricle,” *IEEE Trans. Med. Imag.*, vol. 22, no. 6, pp. 773–776, Jun. 2003.
- [61] C. Corsi, C. Lamberti, R. Battani, A. Maggioni, G. Discenza, P. MacEneaney, V. Mor-Avi, R. M. Lang, and E. G. Caiani, “Computerized quantification of left ventricular volumes on cardiac magnetic resonance images by level set method,” *Comput. Assisted Radiol. Surg.*, vol. 1268, pp. 1114–1119, 2004.

- [62] M. Lynch, O. Ghita, and P. F. Whelan, "Automatic segmentation of the left ventricle cavity and myocardium in MRI data," *Comput. Biol. Med.*, vol. 36, no. 4, pp. 389–407, 2006.
- [63] M. A. Alattar, N. F. Osman, A. S. Fahmy: "Myocardial Segmentation Using Constrained Multi-Seeded Region Growing", *Image Analysis and Recognition, 7th International Conference, ICIAR, Póvoa de Varzim, Portugal 89-98(2010)*
- [64] D. L. Pham, C. Xu, J. L. Prince, "A Survey of Current Methods in Medical Image Segmentation", *Tech. rep., The John Hopkins University, The John Hopkins University, Baltimore, (Jan 1998).*
- [65] A. Garcia, C. Vachier, A. Rosset, JP. Vallée "Multi-criteria seeded region growing for multi-contrast MRI"
- [66] M. D. Cerqueira, N. J. Weissman, V. Dilsizian, A. K. Jacobs, S. Kaul, W. K. Laskey, D. J. Pennell, J. A. Rumberger, T. Ryan, M. S. Verani, "Standardized Myocardial Segmentation and Nomenclature for Tomographic Imaging of the Heart, American Heart Association Writing Group on Myocardial Segmentation and Registration for Cardiac Imaging".
- [67] Umbaugh Scot E, *Computer Vision and Image Processing*, Prentice Hall, NJ, 1998, ISBN 0-13-264599-8
- [68] R.C.Gonzales, R.E.Woods, *Digital Image Processing*. 2-nd Edition, Prentice Hall, 2002.
- [69] J. Serra (1982): *Image Analysis and Mathematical Morphology*, Academic Press, London.
- [70] M. Kass, A. Witkin, and D. Terzopoulos, "Snakes - Active Contour Models" *International Journal of Computer Vision*, 1(4): 321-331, 1987.
- [71] C. Xu and J. L. Prince, "Snakes, Shapes, and Gradient Vector Flow," *IEEE Transactions on Image Processing*, 7(3), pp. 359-369, March 1998 (JHU-ECE TR96-15).
- [72] http://home.dei.polimi.it/matteucc/Clustering/tutorial_html/kmeans.html.
- [73] Lynch M., Ghita O., Whelan P.F.: Segmentation of the left ventricle of the heart in 3-D+t MRI data using an optimized nonrigid temporal model. *IEEE Trans. Med. Imaging*. 27(2),195-203(2008).
- [74] Aletras AH, Wen H. "Mixed echo train acquisition displacement encoding with stimulated echoes: an optimized DENSE method for *in vivo* functional imaging of the human heart" *Magn Reson Med* 2001; 46:523–534.
- [75] Frahm J, Hanicke W, Bruhn H, Gygell ML, Merboldt KD. "High-speed STEAM of the human heart" *Magn Reson Med* 1991; 22: 133-142.
- [76] Fischer SE, Stuber M, Scheidegger MB, Boesiger P. "Limitations of Stimulated Echo Acquisition Mode (STEAM) Techniques in Cardiac applications" *Magn Reson Med* 1995;34: 80-91.
- [77] Fahmy AS, Stuber M, Osman NF. "Correction of through plane deformation artifacts in Stimulated Echo Acquisition Mode (STEAM) cardiac imaging" *Magn Reson Med* 2006; 55 (2): 404-412.

- [78] Osman NF, Sampath S, Atalar E, Prince JL. "Imaging longitudinal cardiac strain on short-axis images using strain encoded (SENC) MRI". *Magn Reson Med* 2001; 46: 324-334.
- [79] M. A. AlAttar, A. G. Motaal, N. F. Osman and A. S. Fahmy "Performance Evaluation Of Cardiac MRI Image Denoising Techniques" - CIBEC'08, Cairo, Egypt
- [80] A. G. Motaal, M. A. AlAttar, N. F. Osman and A. S. Fahmy "Cardiac MRI STEAM Images Denoising Using Bayes Classifier" - CIBEC'08, Cairo, Egypt
- [81] Sijbers J, Den Dekker A. J., Van Dyck D., Raman E. Estimation of signal and noise from Rician distributed data. *Proc.Int. Conf. Signal Proc. and Comm.*, pp. 140- 142, Spain 1998.
- [82] Duda RO, Hart PE. *Pattern classification and scene analysis*. New York,: Wiley; 1973.